Microrobotic Platform for Observing Stimulus Response of Single Motile Microorganism

著者	Belal Ahmed
その他のタイトル	単一運動性微生物の刺激応答計測のためのマイクロロボティックプラットホーム
学位授与年度	令和元年度
学位授与番号	17104甲生工第355号
URL	http://hdl.handle.net/10228/00007876

Microrobotic Platform for Observing Stimulus Response of Single Motile Microorganism

AHMAD BELAL

Department of Life Science and Systems Engineering
Graduate School of Life Science and Systems Engineering
Kyushu Institute of Technology

Contents

List of Figures

Nomenclature

Chapter 2

p	Pixel pitch
d	Focal distance
l	Light intensity
Θ	Magnification dial rotational degree
s_i	Target size
w_{FOV}	FOV width
v	Target relative velocity
X_g, Y_g	Center of gravity coordinates (COG)
I	Pixel intensity
ϕ	Orientation of target
D_x	Distance from COG to center of FOV in x axis
D_y	Distance from COG to center of FOV in y axis
W	Width of high-speed online vision frame
H	Height of high-speed online vision frame
u_x	Control input for tracking stage in x axis
u_y	Control input for tracking stage in y axis
K_x	Adaptive gain in x axis
K_y	Adaptive gain in y axis
e_x	Error signal in x axis
e_y	Error signal in y axis
r	Radius of ROI

a	Semimajor axis of ellipse ROI
b	Semiminor axis of ellipse ROI
S_x	Position reference for x axis
S_y	Position reference for y axis
A	Maximum amplitude
α,β	Constants
μ_k	Grayscale mean value of frame k
I_{max}	Maximum grayscale pixel intensity
N_d	Noise density

Chapter 3

u_r	Position command for microtool
e_r	Error signal in microtool position controller
K_p	Proportional gain
K_i	Integral gain
F_h	Hydrodynamic force
C	Drag coefficient
A_{mt}	Cross section of microtool
v_{mt}	Actuation velocity of microtool
y_{mt}	Deflection of microtool
l_{mt}	Length of microtool
E	Module of elasticity of microtool
I_{mt}	Moment of inertia of microtool
g	Gravitational acceleration
F_m	Magnetic force
F_{my}	Horizontal component of magnetic force
F_{mz}	Vertical component of magnetic force

F_f	Friction force
μ_s	Friction coefficient
l_c	Length of microchip chamber
w_c	Width of microchip chamber
h_c	Height of microchip chamber
n_m	Number of magnets
F_{yp}	Peak value of the horizontal component of the magnetic force

Chapter 4

D_{2x}, D_{2y}	Distance commands for stage 2 on x and y axis
D_{3x}, D_{3y}	Distance commands for stage 3 on x and y axis
v_t	Velocity of the stimulation tool
d_p	Backward movement distance of the *Paramecium* in the avoiding reaction
R_{tp}	Pearson correlation coefficient between v_t and d_p
μ_t	Mean value of the stimulation tool velocity
σ_t	Standard deviation of the stimulation tool velocity
μ_p	Mean value of the backward movement distance
σ_p	Standard deviation of the backward movement distance
Θ_p	Angle of the *Paramecium* in the avoiding reaction

Chapter 1

Introduction

1.1 Investigation of Single Motile Microorganism

Single-celled organisms are the simplest form of life on our planet. Specifically, motile microorganisms possess interesting biological functions that come in handy in various fields. In order to utilize these functions, motile microorganisms have been widely studied both on large population-level and on the single-cell level. The study of large populations can provide us with statistical knowledge pertaining to the behavior of these organisms as a group without clarifying the specific behavior of each cell [1]–[5]. On the other hand, it is very critical to understand and anticipate the behavior of each cell, where the investigation on the single cell-level is essential [6]–[12]. The investigation of single motile microorganisms is known to have high potential in the fields of food production [13], bio-fuel [14], and related research seeks to understand the specific function of mechanoreceptors and growth factor of microorganisms. In addition, the motility of microorganisms has been actively utilized for delivering drugs to targeted organs in state-of-the-art nanomedicine applications [15]. Figure 1.1 shows the wide range of application of investigating the stimulus-response of motile microorganisms.

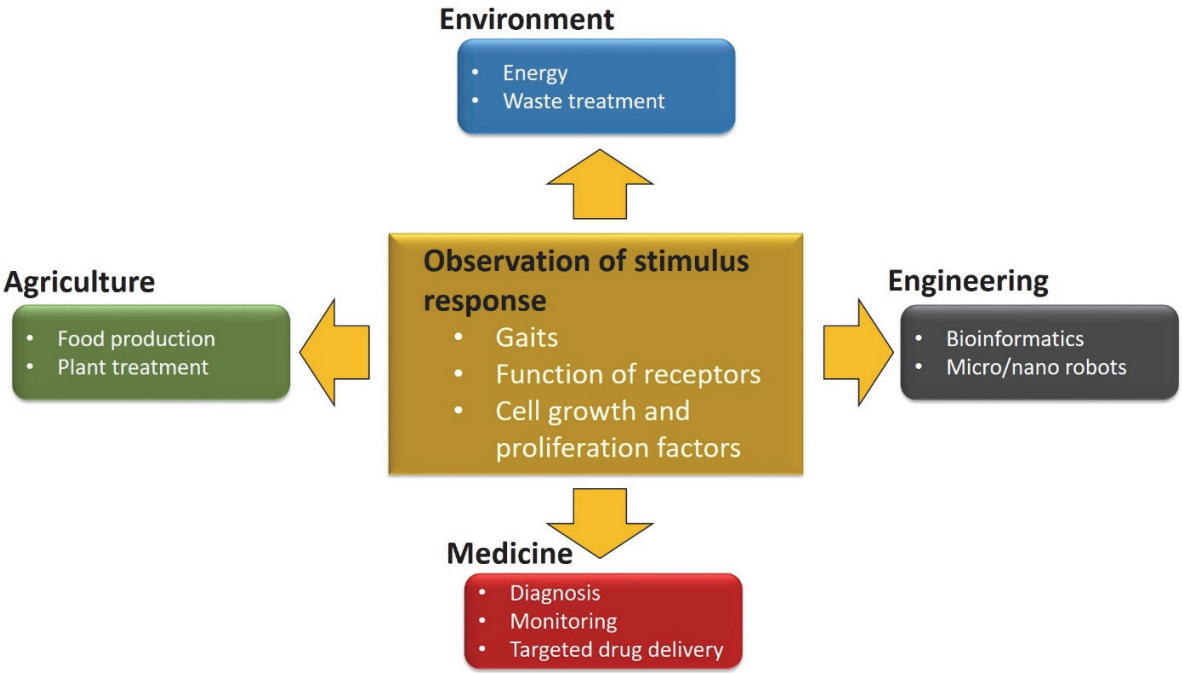

Figure 1.1: Applications of stimulus response observation of motile microorganisms in different fields.

To clarify the characteristics and functions of motile microorganisms, the stimulus-response is examined by applying external stimulations. In this case, the cell is exposed to an external stimulus, whether it be a chemical, electrical, photic or mechanical stimulation, and the response of the cell is then measured and analyzed [16]–[18]. The reaction of the cell to each type of external stimulation can give us unique information about cell characteristics.

1.2 Classification of Cells

The characteristics of the cell can play an essential role in determining the most appropriate investigation method. When looking from an investigation point of view, the movement of the cell is the main factor that affects the difficulties of the investigation process. In fact, we can

divide the cells into three main categories based on their movement in the fluidic environment as shown in Figure 1.2. These three categories are adhesive cells, floating cells, and motile cells.

As the name suggests, adhesive cells are cells that adhere to the culturing substrate such as tissue cells [19][20]. Consequently, the observation of this type of cells becomes relatively easier because they move with a very slow speed, although long-time observations are technically challenging [21][22]. However, if the target is to observe the stimulus-response of the cell, such as mechanical stimulation, compensation methods need to be considered in order to observe the real-time response of the cell for a long time. Ursekar et al. [23] have developed an equibiaxial stretching system using a stepper motor and a specially modified PDMS membrane that confines the cell in one area using cylindrical PDMS walls. The walls guarantee the homogeneity of the strain applied to the cells. Using their system, they succeeded in observing the effect of equibiaxial strain on cells even for very low magnitudes of strain. However, the cells could only be observed before and after applying the strain because of the movement of the membrane in the vertical direction when applying strain.

Floating cells are cells that do not adhere to the substrate and are constantly floating inside the fluidic environment such as oocytes. Although these cells do not have motility, they are more difficult to observe and investigate in liquids because of their high susceptibility to fluidic disturbance, which is easily generated in microfluidics. Furthermore, the fluidic disturbances could affect the position and the posture of the target cell and would make mechanical procedures such as manipulation and injection tasks more challenging. A large number of studies have proposed different ways to deal with the observation and manipulation of floating cells. For instance, Xie et al. [24] developed a robot-assisted cell manipulation system for injection tasks in *Zebrafish* embryos. In their system, a visual tracking system and autofocusing

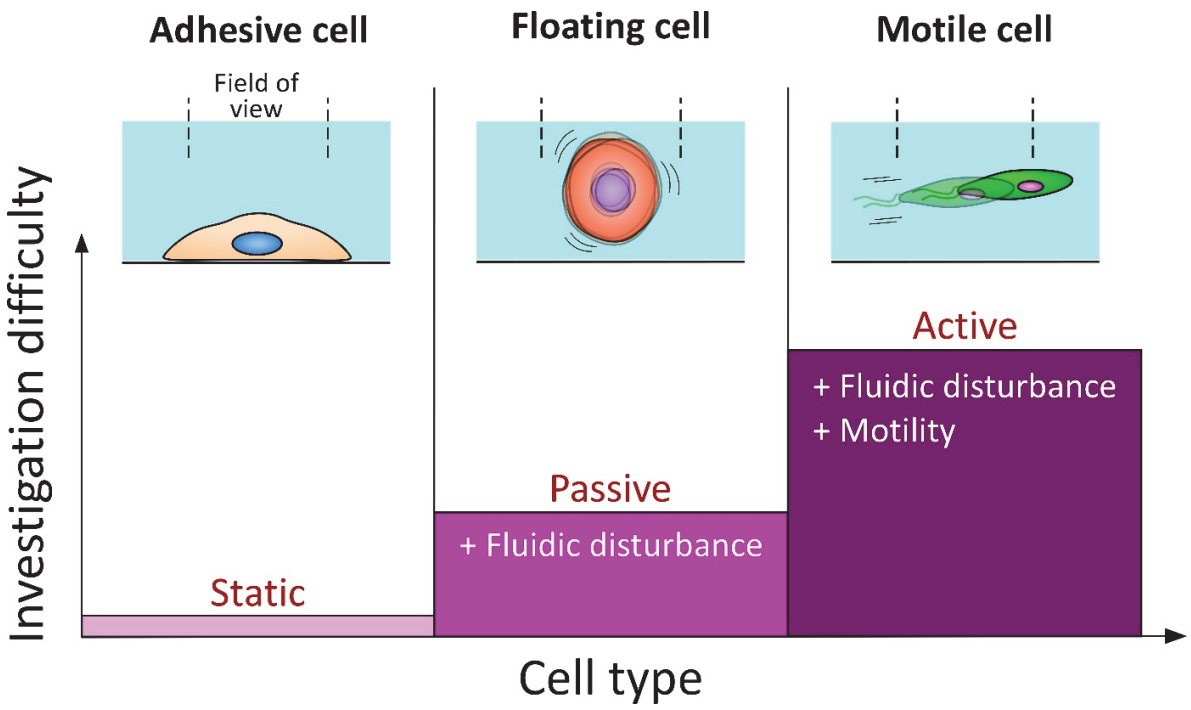

Figure 1.2: Cell classification based on movement pattern.

were used to achieve precise injection of embryos. Hagiwara et al. [25] have developed an on-chip microrobot for cell manipulation. Using the developed microrobot, they have succeeded in oocyte manipulation and cutting in a closed microfluidic environment. However, the floating cells' susceptibility to fluidic disturbance is a remaining obstacle.

Motile cells are cells that possess active motility, which allows them to swim freely in fluidic environments. In fact, the observation and investigation of motile cells are the most difficult compared to the previous cell types owing to the high agility, high moving speed, and the small size of such cells, where the cell easily escapes outside the field of view (FOV) of the microscope. Moreover, similar to floating cells, motile cells are highly susceptible to fluidic disturbances that would drastically increase the difficulty of investigation of this type of cells.

1.3 Conventional Investigation Approach of Motile Microorganisms

Because many aquatic microorganisms have motility and agility, it is quite difficult to investigate their dynamic behavior and stimulus-response under a microscopic environment. Therefore, to conduct observations in a highly magnified environment, the motile microorganisms are conventionally immobilized before the investigation to reduce their activity, as shown in Figure 1.3.

Different immobilization techniques for motile microorganisms have been proposed in the literature. For example, adding chemicals to reduce the speed or completely stop the movement of the cell's actuators have been widely used [26]–[28]. However, the main drawback of chemical immobilization is the toxicity and the effect on the viability of the cells. On the other hand, mechanical immobilization is another widely used method for microorganism investigation. Jana et al. [29] have investigated the different swimming modes of *Paramecium* in geometrically confined spaces to show the microorganism's flexibility in active navigation inside confined spaces. In their work, *Paramecium* was immobilized mechanically using a

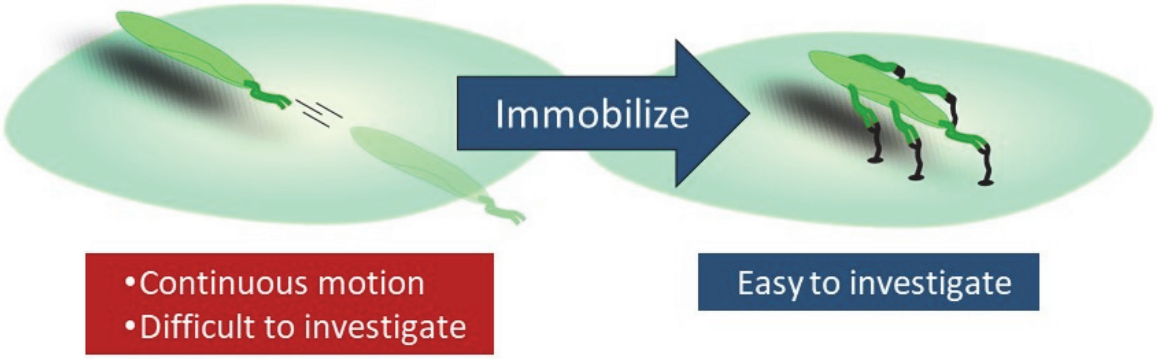

Figure 1.3: Conventional approach to investigate motile microorganisms by immobilization.

suction pipette. Mechanical immobilization can also be achieved through a mechanical microcompressor, which flattens and restricts the movement of cells. Yan et al. [30] have developed a microcompressor equipped with microfluidics for the immobilization of microorganisms. Using their device, they have conducted numerous observations of cellular events in several protozoan species.

Nonetheless, this immobilization acts as an external force that affects the functionality and response of the microorganism. In order to get the most natural responses to the stimulation applied to a motile microorganism, there should be no forces exerted on the microorganism other than the stimulation force. This means that the microorganism should not be immobilized and it should be allowed to swim freely inside the fluidic environment, but this raises a new problem. Since the microscope's FOV is fixed in place and its dimensions are relatively small, the target microorganism can easily swim outside the FOV where we can no longer apply stimulation nor observe its response. In order to acquire the most natural stimulus-response of swimming microorganism, two main procedures should be taken into consideration:

1) Continuous observation of the target microorganism.

2) Applying stimulation to the microorganism without disrupting the continuous observation to clearly see its specific reaction.

In particular, applying mechanical stimulation to a freely swimming microorganism while observing it is a very challenging task because of the small size and high agility of such organisms.

1.4 Continuous Observation

The main task of continuous observation is to keep the target in the FOV of the position sensing device. For large targets, continuous observation is generally achieved through active vision systems [31]–[34]. In a controlled active vision, the vision sensor is moved using actuators to keep the FOV of the camera focused on the target object. On the contrary, thanks to the small size of the microorganism, it is possible to keep the vision sensor in a stationary state, while controlling the position of the container of the cell to keep it in the FOV of the microscope. On the other hand, in case of continuous observation for investigation purposes, the ability to integrate a stimulation mechanism should be considered in the design of the observation system.

A very important question when designing observation systems is how much details do we need to observe? The answer to this question would greatly affect the difficulty of observation, as shown in Figure 1.4. For instance, if our purpose is to measure the speed of an organism, spatially large FOVs of the sensing device would be preferable, whereas spatially small FOVs would be more appropriate if our purpose is to observe the detailed dynamic behavior of the organism. In the case of single-cell investigation, highly detailed observations are required to elucidate the specific behavior of the cell when responding to stimulations. Therefore, it is preferable that the target cell would almost entirely fill the FOV of the observation area. In fact, there is a strong correlation between the relative speed of the object and the size of the observation area. In case our purpose is to have detailed observations of the target, high relative speed should be expected.

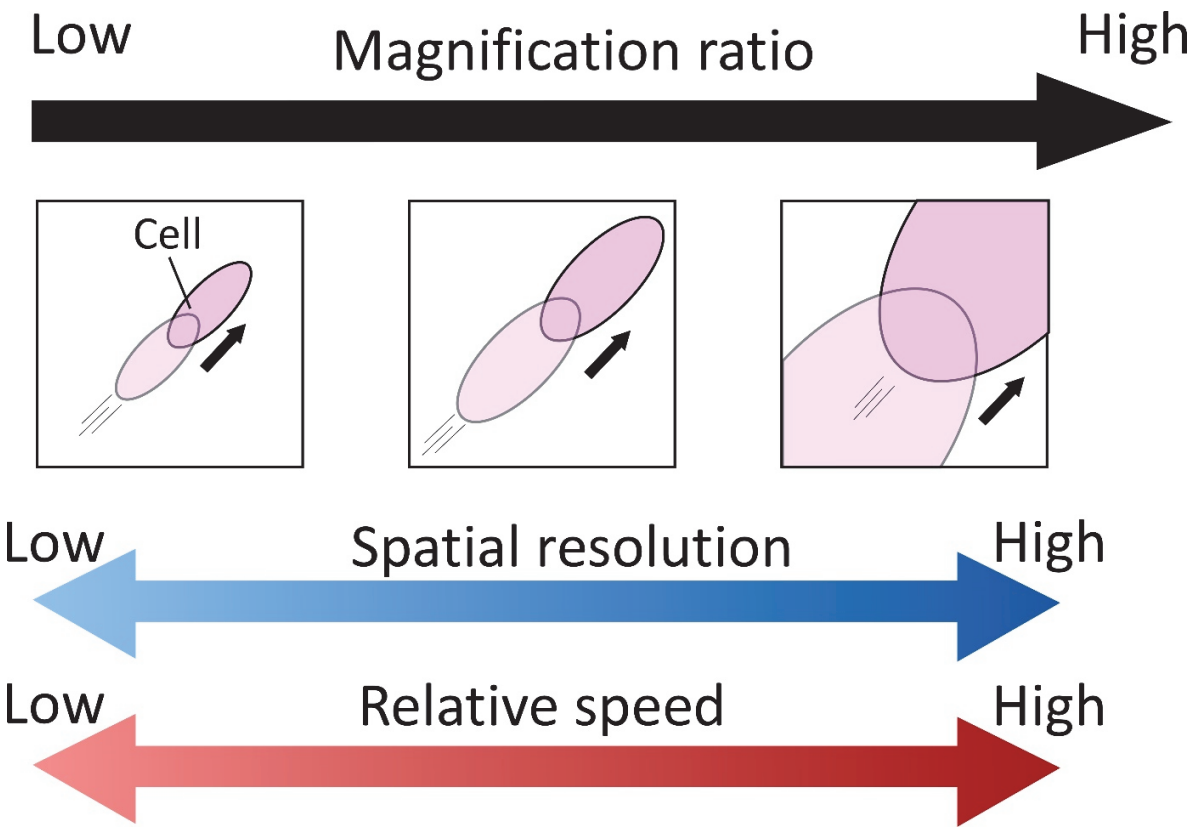

Figure 1.4: The effect of magnification ratio on the level of details and relative speed of the observed object.

Motile microorganisms are regarded as fast-moving objects when taking their size (few micrometers ~ hundreds of micrometers) and the required level of observation details into consideration. Although these organisms might seem to move slowly when using conventional speed metrics (e.g. mm/s), they actually move very quickly relative to their size. One of the speed metrics that can be used in this case is the "body length per second" metric. Using this metric, which is crucial in designing observation systems for detailed observation purposes, the speed of a motile microorganism (200 µm body length and 2 mm/s moving speed) is almost equivalent to the speed of a car moving at 144 km/h (4 m body length, 40 m/s moving speed).

1.4.1 Trapping

One way to keep the target in the FOV is to trap the motile microorganism in one restricted area. Confined microchambers and droplets can passively trap motile cells to aid in the observation of their mobility. Yuya et al. [35] have proposed a method for producing monodisperse semi-permeable microcapsules for observing encapsulated cells using alginate-poly-L-lysine (PLL) membrane. These microcapsules were fabricated using a monolithic three-dimensional (3D) microfluidic axisymmetric flow-focusing device. To produce a soft condition for the encapsulated cells, an internal gelation method was implemented. The produced microcapsules were robust and had a uniform size. The microcapsules were used in a bead-based microfluidic system to observe trapped cells. The main advantage of this work is the semi-permeable nature of the microcapsules, where trapped cells cannot travel through its membrane but nutrient and waste can. Although this type of trapping allows for continuous observation of motile microorganisms, detailed observations cannot be obtained because the size of the FOV should be equal to the size of the confining area, and reducing the size of the confining area would immobilize the microorganism. Moreover, applying mechanical stimulation would be difficult due to the closed nature of the environment.

On the other hand, trapping of motile microorganisms can be achieved using active force. A large number of studies have been conducted to trap a motile microorganism using different kinds of applied force. In fact, to trap a motile microorganism, the force generated by the trapping mechanism should be larger than the force generated by the motility of the cell. Optical trapping is one of the most studied areas in microobjects manipulation, known as “Optical tweezers”. The main concept behind optical trapping is to implement a tightly focused laser

beam using a microscope objective with a high numerical aperture, which would trap the target in 3D. Thalhammer et al. [36] have developed macro-optical tweezers that can trap comparatively large motile microorganisms by applying counter-propagation beams instead of tightly focused beams. Nonetheless, the main drawback of optical tweezers is the bio-effects on the target cell viability even when reducing the strength of the laser beam. Moreover, comparatively large and fast microorganisms are difficult to trap because of the low trapping force generated by the optical tweezers.

Because motile microorganisms live in aquatic environments, an apparent way to trap the cell is through hydrodynamic force by controlling the fluid flow around the cell. This can be achieved through generating push and pull laminar flows or through fluidic eddies. Barry et al. [37] have succeeded in trapping a single motile cell by generating fluidic eddies. Their device mainly consisted of a fixed cylinder inside a microchannel. Low-frequency oscillations were applied using a piezoelectric diaphragm to generate eddies and trap single cells in four different positions. This allows for long-time observations of the target cells without affecting the viability of the cell as much as possible, compared to other trapping techniques. However, the trapped microorganism would be constantly under the effect of the fluidic force, which would affect the credibility of the stimulus-response of the cell when stimulation is applied later.

1.4.2 Tracking

Visual tracking systems implement visual servoing to keep the target inside of the FOV. Visual servoing approach mainly uses a vision sensor to recognize and track the movement of the target, and an actuator to move the sensor, or the target so that the target is kept inside the FOV of the vision sensor [38][39]. One of the main parameters that play an essential role in the

performance of a visual tracking system is the sampling rate of the vision sensor, which is measured in frames per second (FPS). In fact, to choose the appropriate speed of the vision sensor, velocity and size of the target and the required level of observation details should be taken into consideration. As discussed earlier, the relative speed of motile microorganisms increases drastically when viewed in high magnifications. For high-speed targets, vision sensors with the conventional camera frame rate (30 FPS) cannot keep up with their speed. Therefore, high-frame rate image feedback is highly required.

Recently, the use of high-speed vision sensors has become more common in tracking and control for robotic systems [40]–[43]. Especially by utilizing high-speed "online" vision sensors (cameras) that can operate at speeds of hundreds or thousands of frames per second, real-time feedback control can be achieved with high stability. Specifically, high-speed visual servoing has the advantage of tracking the target as it is moving in slow motion, which allows for detailed observation of the target. In fact, one of the main advantages that these online vision sensors offer is the ability to continuously track a high-speed target even when the trajectory changes abruptly, which is the case when tracking highly agile organisms such as motile microorganisms.

A number of works have been conducted to track fast organisms using high-speed online visions. For example, Sakakibara et al. [44] have developed a tracking system for flying insects. Their system implemented a high-speed online camera and galvano mirrors, which reduce the inertial moment and increase the response time compared to conventional cameras driven by servomotors, to keep the target insect in inside the FOV of the video recording camera and the system was successful in continuously tracking a freely flying fly. Ogawa et al. developed a high-speed tracking system composed of a high-speed online vision sensor and motorized stages

[45]. By using high-speed visual servoing technique, they succeeded in the continuous tracking of single *Paramecium* under the microscope, even in 3D space.

The main bottleneck in high-speed vision systems is the processing time of the image processing algorithm. In fact, most of the high-speed vision-based tracking systems have implemented parallel processors to keep up with high-speed image feedback. Although parallel processing shows an excellent performance in image processing, its application is quite complex and costly especially when the resolution of the imaging device is comparatively large.
Additionally, the previously mentioned works in high-speed tracking have not included a stimulation mechanism, specifically mechanical stimulation, in their designs, which is a difficult task because of the disturbance it adds to the environment. Moreover, the maximum tracking time was at the level of tens of seconds, although it is highly desirable to observe the target organism for a longer time.

On the other hand, to enhance the performance of the tracking systems, predictive algorithms and filters have been implemented to anticipate the next position of the target. In fact, Kalman filters are one of the widely used predictive filters in robotic visual tracking [46][47]. By using a state model of the system and measurements with statistical noise, Kalman filters can increase the accuracy of the measurements and predict the next state of the system when needed. Shen et al. [48] have developed an autonomous quadrotor with limited onboard processing and sensing capabilities, which can travel in complicated environments autonomously at speeds up to 4 m/s and roll and pitch angles exceeding 20° using only a camera and an inexpensive inertial measurement unit (IMU) as sensors. In their system, a camera with 20 Hz was used for image feedback. However, the 20 Hz pose estimate from the vision system alone is not sufficient to control the robot. Therefore, an Unscented Kalman filter (UKF) was

employed to increase the pose and velocity estimation frequency of the drone to 100 Hz. However, in the case of motile microorganism the trajectory is mostly unpredictable and nonlinear, where the cell interacts with the environment and changes direction suddenly. This necessitates the use of nonlinear filters, which is computationally expensive and would increase the complexity of the system.

The use of high-speed online vision sensor is effective in tracking fast objects as if we are seeing the target in super-slow motion. However, there are instances when we cannot even see the object, no matter how fast the vision sensor is. Let us assume an ideal situation where we have an infinitely fast vision sensor and an infinitely fast actuator to track a target. In this case, the trackability of the target would be irrelevant to its relative speed and size, hence infinitely fast and small objects could be tracked assuming that a suitable microscope is available. However, this is not always true. In fact, a very common and challenging problem in the field of target tracking is the occlusion problem. Occlusion happens when the tracked object is partially or completely obscured from the view of the camera by another object. A substantial amount of research has been done to attempt to solve the occlusion problem in target tracking [49], and a number of solutions have been proposed that are based on deep learning [50][51], and predictive filters [52][53] to name a few. Nonetheless, most of the currently used algorithms face a huge difficulty to recover tracking after a full occlusion occurs, especially when the target is moving [49]. For example, even when using predictive algorithms such as Kalman filters, it would still be difficult to predict the target trajectory in the case of occlusion. Figure 1.5 shows an occlusion example where two close-to-identical objects are occluded by an obstacle. The first scenario shows a case where it is possible to predict the trajectory of each target. On the other hand, the second scenario shows a more difficult case where the targets change their

trajectory abruptly, which substantially increases the prediction difficulty. Moreover, as mentioned above, the occlusion problem is not related to the frame rate of the vision sensors, and thus using high-speed imaging would not solve the problem. One promising solution for the occlusion problem is to use a hardware approach to design the tracking environment in a way that decreases or eliminates the occlusion between objects in the observation field.

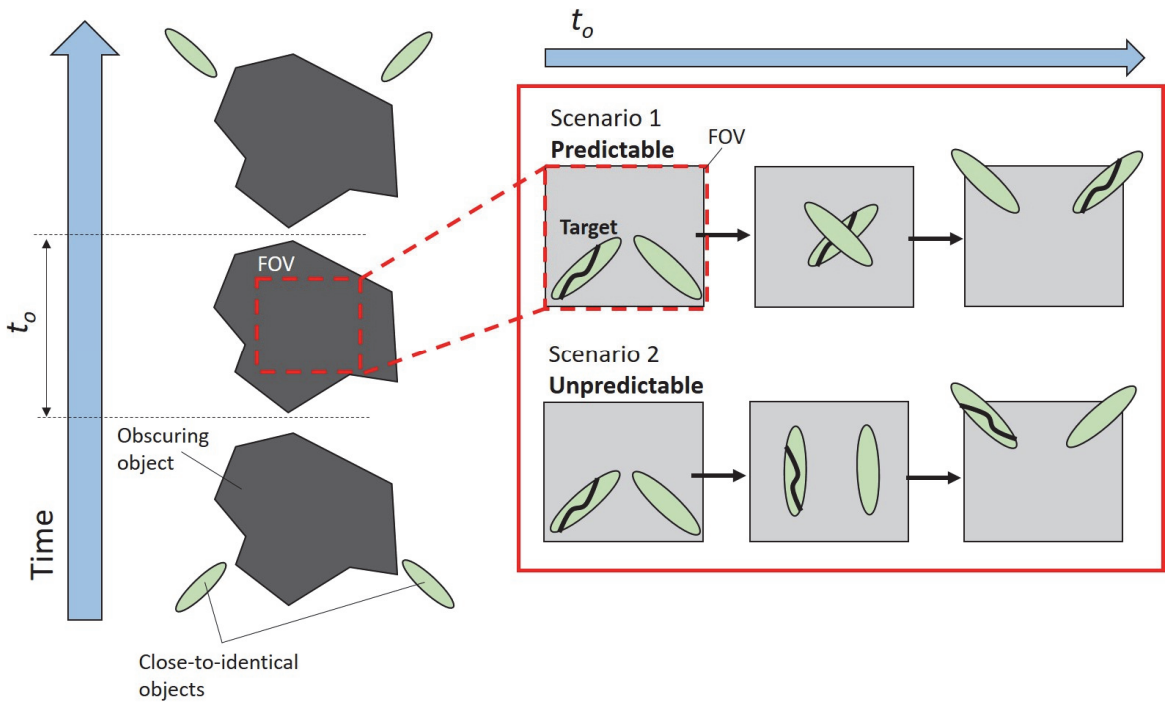

Figure 1.5: Occlusion problem in predictable and unpredictable situations.

1.5 Applying Stimulation

The stimulation of microorganisms demonstrates a very challenging task. In fact, the difficulty of stimulation depends highly on its type and the required level of observability of the stimulus-response. For example, applying chemical or electrical stimulation, which does not require direct contact with the microorganism, is relatively easier compared to mechanical stimulation where the stimulation tool should directly touch the target microorganism. A number of conventional methods and devices have been developed for the purpose of mechanical stimulation and manipulation of cells. In case of mechanical stimulation, observing the stimulus-response with a high spatial resolution (high magnification) requires us to pay much attention to the amount of fluidic disturbance that the stimulation microtool generates when applying stimulation, where the size of the tool plays a substantial role, as shown in Figure 1.6.

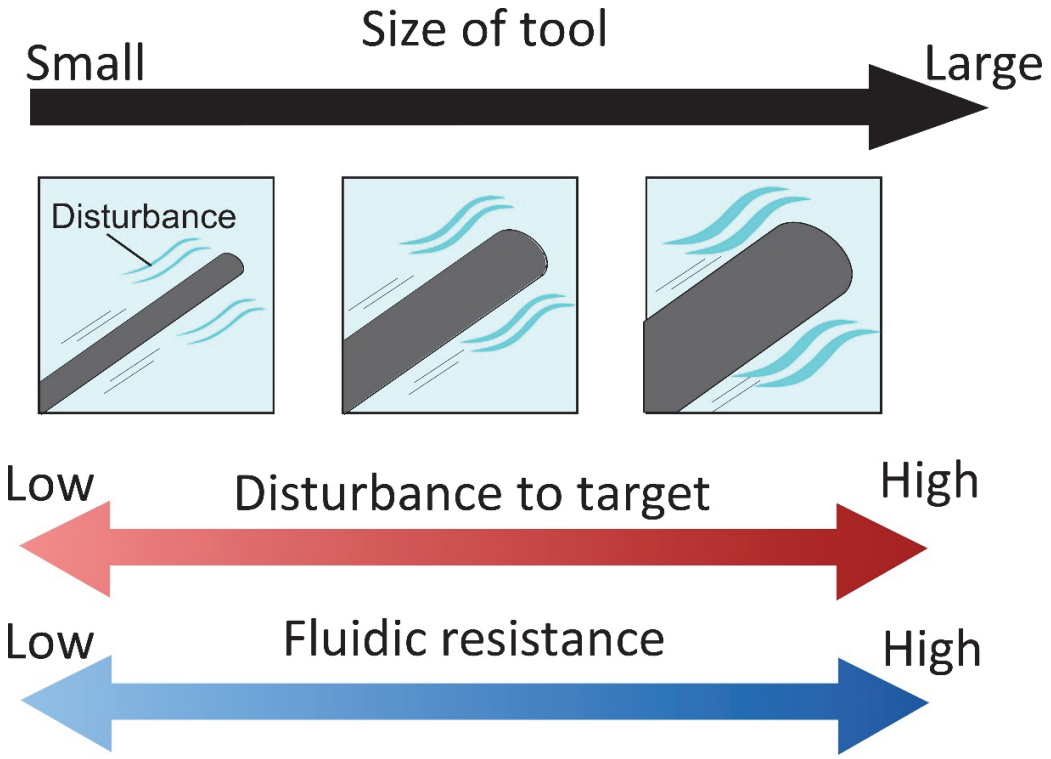

Figure 1.6: Effect of stimulation tool size on the generated fluidic disturbance.

1.5.1 Micromanipulators

Conventionally, mechanical investigation of cells has been achieved through manual operation or using relatively large micromanipulators. In this case, the sample microorganism is introduced inside the culture medium in a petri dish under the microscope, and two micromanipulators, equipped with microtools such as microneedles or microcapillaries, are set to both sides of the microscope to carry out the investigation. Although these manipulators are suitable for handling adhesive cells, they are less suitable for floating or motile cells because they generate a large amount of fluidic flow as a disturbance when actuated, which affects the position and the visibility of the target cell and drastically increases the difficulty to observe the stimulus-response. Moreover, micromanipulators cannot be used in closed environments and are comparatively difficult to operate since they are actuated in 3D. Nonetheless, a number of works introduced automation techniques to enhance the handling of floating cells such as embryos using image feedback. For example, Arai et al. [54] have developed a bio-micromanipulation system for embryos and yeast cells using conventional micromanipulators together with virtual reality (VR). The system constructs a 3D model of the target in real-time and allows for 3D actuation of the micromanipulators. Tanikawa et al. [55] have developed a two-fingered micromanipulators simulating chopsticks, for the handling of micro bio-objects. However, a common limitation for micromanipulator-based systems is the relatively slow actuation speed due to the high generation of fluidic disturbance in case of high-speed actuation.

1.5.2 Atomic force microscopy (AFM)

AFM has been widely used for biological applications in the past two decades. The main part of an AFM is a cantilever beam that scans a specimen in the two-dimensional (2D) plain.

When the tip of the beam reaches the proximity of the sample, forces such as van der Waals forces and electrostatic forces attract the tip of the cantilever causing deflection. The resultant deflection is then measured using a reflected laser beam. Conventionally, AFM has been used for imaging sub-micrometer biological entities such as viruses and proteins, where optical microscopes reach their theoretical limits (Abbe diffraction limit). Nonetheless, AFMs have been recently used for single-cell applications such as stimulation, handling, and mechanical sensing. Afrin et al. [56] have used AFM to create holes at designated locations on cell membranes for investigating the cell's viability, targeted gene delivery into the cell, and visualization of intracellular structure through the hole. The holes were created using beads coated with phospholipase A2 (PLA2). The coated beads were attached to the cantilever beam and actuated to touch the membrane of the cell to create holes. Fluorescent images proved the creation of holes and the intracellular structure of the cell was confirmed through the hole.

On the other hand, a relatively new modification of AFM called Fluid Force Microscopy (FluidFM), provides the ability to deliver liquids to the cell through microchannels fabricated inside the cantilever beam and can be used for cell manipulation, and injection [57]–[59]. Dörig et al. [60] have utilized FluidFM with pressure controlled microchannels to achieve displacements of living cells with micrometer precision. Using their system, they succeeded in the spatial manipulation of *S. cerevisiae* and *E. coli* cells. Although AFM can be used for precise manipulation and handling of static cells or floating cells, it proves not suitable for motile cells manipulation. The accurate manipulation of the cantilever beam and the force interaction requires careful and slow manipulation, which is not practical in case of high-speed moving cells. Moreover, similar to a micromanipulator, AFM can only be used in open spaces because of its tethered nature.

1.5.3 Microrobots

Recently, microrobots have been widely developed for biological applications because of their small size, precision, and ease of manipulation. The small nature of microrobots makes it difficult to integrate actuators, such as motors, inside the robot. Therefore, microrobots are mostly actuated using force fields such as magnetic or electrical fields. Microrobots can achieve relatively high actuation speed with good positioning accuracy suitable for cell applications. Moreover, because the stimulation tool is completely disconnected from the actuator, the stimulation and handling experiments can be conducted in a completely closed environment such as a microfluidic chip. Ye et al. [61] proposed a dynamic trapping mechanism of motile microorganisms by making use of the rotational flow field generated by a magnetically driven microrobot. Their approach achieved 2D selective trapping and transportation freely swimming bacteria successfully. Even though the motile cell could be trapped and transported using fluidic currents, there is a constant fluidic force exerted on the cell that would make it difficult to observe a fully natural stimulus-response.

In addition, Hagiwara et al. [25][62] have proposed an on-chip magnetically actuated microrobot for cell investigation applications. By utilizing ultrasonic vibrations and a 3D patterned surface, the positioning accuracy, actuation speed, and generated force of the microrobot were drastically enhanced and were adequate for a wide range of cell manipulation. Moreover, the small size of the robot helped in reducing the fluidic disturbance generation. Nonetheless, the fabrication of the patterned surface was relatively complicated and time-consuming. In addition, the control of the robot for continuous tracking of a motile microorganism reduced its performance in both speed and accuracy.

1.6 Objective

Based on the background discussed above, the objective of this research is to; continuously observe the swimming behavior and the stimulus-response of a single motile microorganism for a relatively long period. The target is motile microorganisms that are ten to several hundred micrometers. This size range includes motile microorganisms with maximum speeds of several millimeters per second (e.g., *Euglena*, *Paramecium*, and *C. elegans*).

As mentioned in Section 1.2, the high motility and the susceptibility to fluidic disturbance of the motile microorganism along with its small size are the main difficulties that should be addressed in order to continuously observe and examine the stimulus-response of the target. As discussed in Section 1.3, two main steps should be considered to observe the stimulus-response of a motile microorganism, observation, and stimulation.

Figure 1.7 shows an illustration of the objective of this dissertation. First, the continuous observation is achieved by developing an observation platform that utilizes a high-speed online vision sensor to tracking the motile microorganism in such a manner that it will constantly keep the target inside the microscope's FOV. As a result, the motility problem of the target microorganism is solved. Next, a stimulation platform that utilizes a microtool with a proper size that would generate as low fluidic disturbance as possible is then used, and hence the susceptibility to fluidic disturbance problem is solved. Each of these solutions would participate in making the stimulus-response of a motile microorganism observable. Finally, the two platforms are integrated to make a functional platform that drastically reduces the difficulty of observing the stimulus-response of a motile cell making its observation comparable to an adhesive cell.

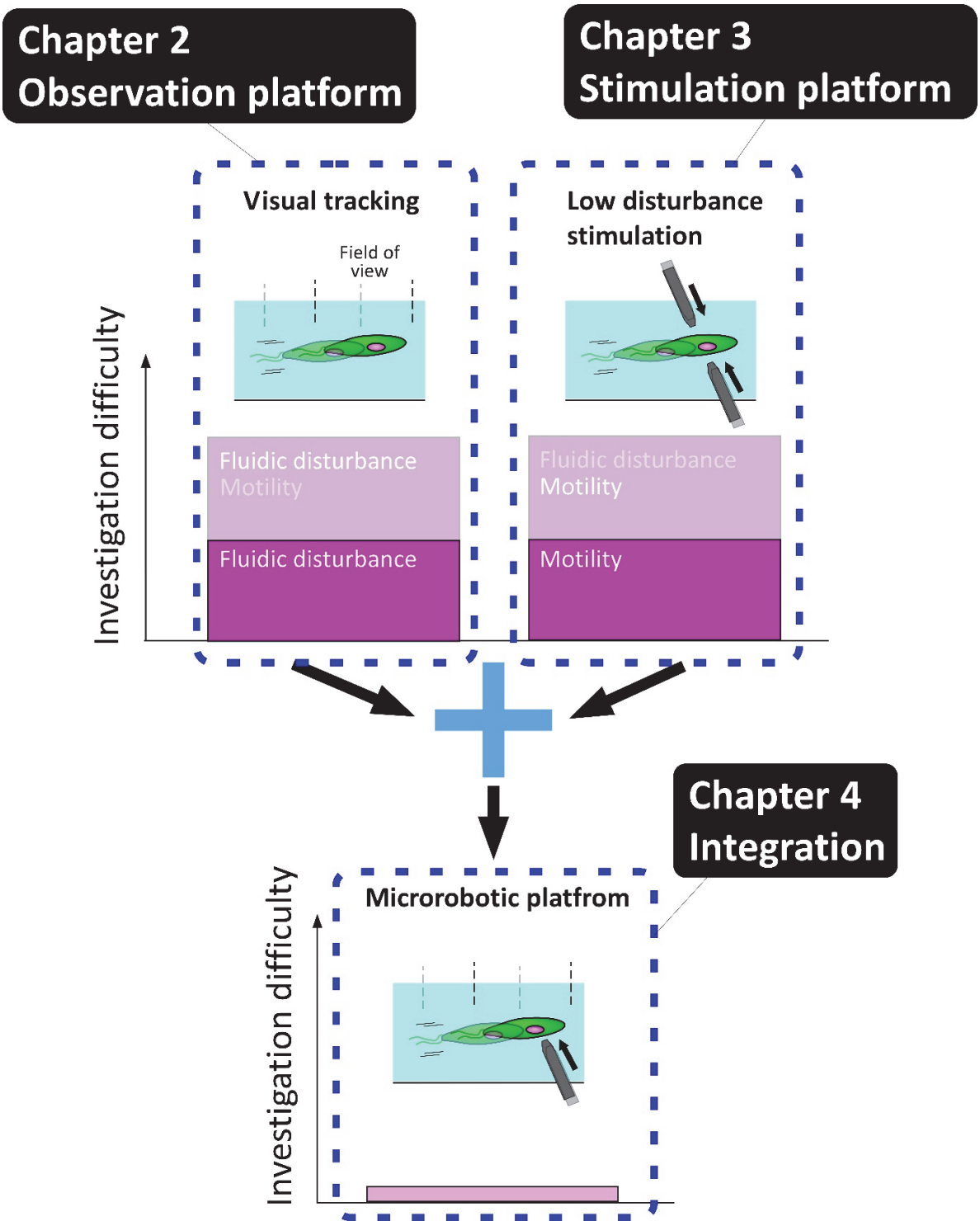

Figure 1.7: Conceptual image illustrating the objective of the dissertation.

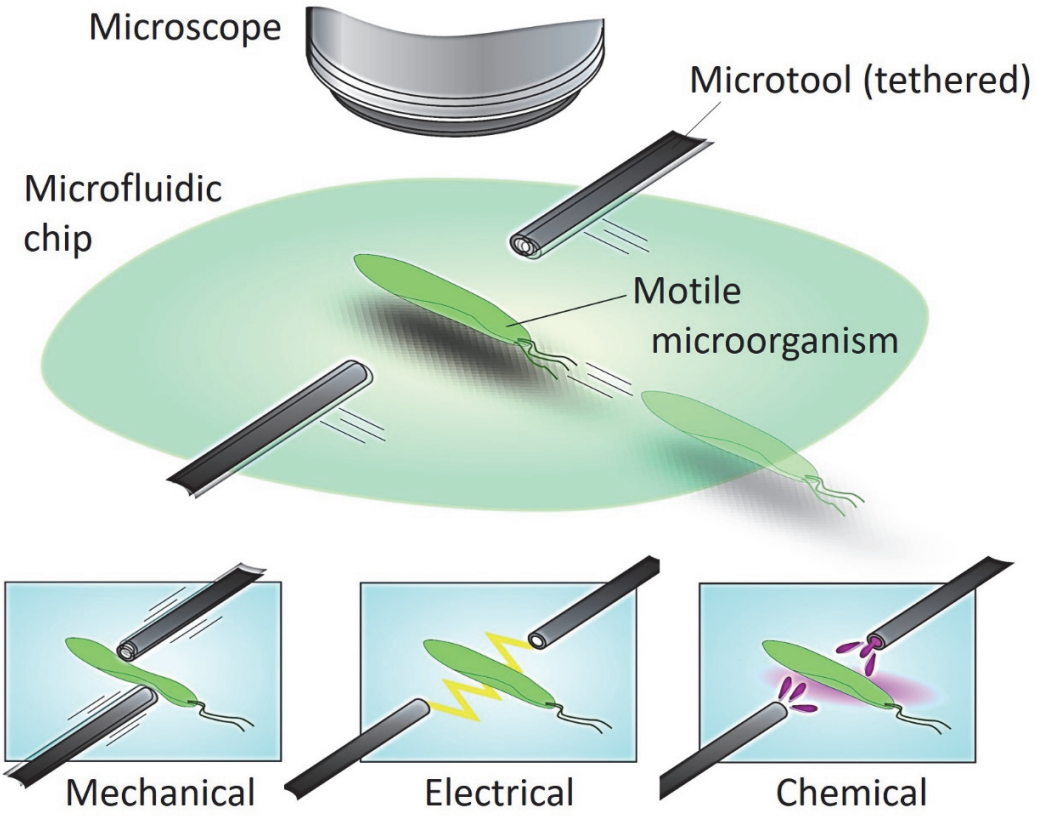

Figure 1.8: Conceptual image of the proposed approach for motile microorganism investigation.

A conceptual image for the proposed approach of this dissertation is illustrated in Figure 1.8. The microorganism can be observed continuously without immobilizing it, even when applying stimulation. The applied stimulation will be the only force exerted on the microorganism, and hence we can observe nearly natural reaction unaffected by external factors.

1.7 Outline of the Dissertation

The dissertation includes five chapters that are organized as follows:

Chapter 1: background, related works, and the objective of this dissertation are discussed.

Chapter 2: in this chapter, continuous observation, which is the first step for investigating single motile cell, is discussed. The two subsystems, the magnification system, and the tracking system that constitutes the platform are presented. First, the platform components and the basic algorithm for the tracking and the magnification systems are introduced. Next, the design of a noise elimination algorithm for robust and long-time tracking is shown. Finally, the performance of both the tracking and the magnification systems is demonstrated through the basic experiment and the limitation of the platform is confirmed.

Chapter 3: the next step for investigating freely swimming motile cells, which is to apply stimulation without disrupting the tracking of the cell, is introduced. The reason for choosing thin microtools and the difficulties in actuating such tools are discussed. Next, a drive method for deflection compensation of thin microtools actuated inside a fluidic microchip is proposed. The hydrodynamic drag force acting on the tool is modeled and estimated, and the magnetic force generated by a number of permanent magnets is used to counteract the drag force. Finally, basic experiments to design the arrangement of the permanent magnets, and to confirm the effectiveness of the drive method are conducted.

Chapter 4: in this chapter, the integration of the observation and stimulation platforms is described. Next, as a biological application, the final platform performance was verified on an actual motile cell, the *Paramecium.* First, the performance of the observation platform was demonstrated by conducting long-time tracking experiments on *Paramecia* inside a microfluidic chip. Next, a number of stimulation experiments, mechanical and electrical stimulation, were conducted to show the effectiveness of the final developed platform.

Chapter 5: finally, the contribution of the dissertation is summarized, and the possible future work is discussed.

Chapter 2

Observation Platform

In this chapter, the first step in developing an investigation platform for a single motile microorganism, the observation platform, will be introduced. The required specifications and the difficulties of observing a freely swimming motile cell will be discussed. An observation platform with a variable magnification mechanism and a high-speed tracking system will be developed. The specific design of the observation platform will be described and the limitation and robustness of the tracking system will be confirmed through basic experiments.

2.1 Required Specifications

An aquatic microorganism swims in all directions inside the water environment. This 3D movement poses a huge difficulty when tracking a single microorganism, and drastically increases the overall system complexity. Combined with the high motility and small size of the microorganism, continuous observation becomes a very challenging task. Specifically, observing the stimulus-response of the target cell requires a solution that considers the special characteristics of motile microorganisms. In order to build an observation platform that can

continuously track the microorganism for a long time and observe its stimulus-response, the following requirements should be taken into consideration:

1. Reduce the movement dimensions of the microorganism: instead of using a 3D tracking system, a hardware approach can be used to control the environment of the target cell and reduce the dimensions of its motion. This can be done by introducing the microorganism inside a microfluidic chip with an appropriate height that will almost eliminate the movement of the cell in the vertical axis. Consequently, the cell moves only in the horizontal plane, which would drastically reduce the complexity of the tracking system. The thickness of the flat space can be precisely adjusted by using a microfabrication technique. It is worth mentioning that the moving directions of the motile cell could be further decreased from 2D to 1D by introducing the cell into a flow path with a microchannel on a microchip. However, in the case of a motile microorganism, a laborious procedure is required to induce it to the desired position of the microchannel by fluidic control.

2. Locate a microorganism in a short time: as mentioned earlier, detailed observation of the target where the cell mostly fills the FOV of the microscope is preferable. Nonetheless, it is difficult and time-consuming to find the target microorganism in a highly magnified environment. Therefore, a variable magnification mechanism would drastically reduce the searching time by changing from low to high magnifications depending on the task being conducted and would increase the efficiency of the overall experimental conduction. For this purpose, a number of parameters should be controlled when changing the magnification ratio to maintain the quality of the observed image. Specifically, both the focal distance and the illumination of the microscope should be controlled.

3. Keep the microorganism inside the FOV of the microscope: even in a 2D environment, motile microorganisms can easily swim outside of the FOV of the microscope. In fact, it is relatively easy to observe the position and movement of a motile microorganism in a low-magnification environment. However, a high magnification ratio is preferred to observe specific behaviors and reactions. Consequently, the relative speed of a motile microorganism increases with an increasing magnification ratio because the time duration of microorganism in the observation FOV decreases, and hence tracking the position of a single motile microorganism continuously becomes difficult. Therefore, to obtain observations with a high magnification ratio, together with a high spatial resolution, a high-speed visual servoing implementing a high-speed online vision sensor is required.

4. Enhance the robustness of the tracking system for long-time observation: the fluidic environment mostly contains debris and bubbles (image noises) that make the extraction of accurate position information of the target cell using conventional image processing a very difficult task. On the other hand, when applying stimulation, the stimulation tool might reduce tracking stability, especially when the tool is in direct contact with the target cell (e.g., mechanical stimulation). Moreover, the microorganism behavior must be observed after applying the stimulation to confirm its stimulus-response. Therefore, to build an effective tracking system, the position of the target must be recognized regardless of other objects visible in the FOV that can be considered as noise. In fact, it is possible to eliminate the image noises using conventional image processing algorithms for object detection and classification. Nonetheless, when dealing with high-speed online vision sensors, the processing time for each frame is small and thus it would be difficult to use time-consuming detection algorithms. Hence, a maximally simplified, robust image processing technique is required.

2.2 Platform Components

Based on the required specifications, a 2D high-speed tracking platform with variable magnification mechanism was built. The objective of the tracking platform was to keep the tracked target at the center of the FOV of the microscope for a long period with high spatial resolution. The platform mainly consisted of a high-speed online vision sensor and a high-speed motorized stage. Figure 2.1 shows the basic components of the developed observation platform and the coordination system of the platform. A high-speed online vision sensor (IDP-ExpressR2000, Photron Inc., Tokyo, Japan) [19] was implemented into the microscope for high-speed image capture. The vision sensor can capture images of 512 × 512 pixels at 2000 FPS. A CCD camera (ZBR2-PGEHD-28S4C-CS, Point Grey Research Inc., Now FLIR Integrated Imaging Solutions Inc., Richmond, BC, Canada) was also attached to the microscope for observing the behavior of the microorganism. The CCD camera can capture color images of 1920 × 1080 pixels at 15 FPS. A 140× lens was installed into the digital microscope (DVM2000, Leica Microsystems Inc., Buffalo Grove, IL, USA), and the magnification ratio could be seamlessly changed from 140× to 1400× by rotating the magnification dial attached to the lens barrel of the microscope. A metal scale was attached to the magnification dial, along with an optical sensor (VP-90, Keyence Inc., Osaka, Japan) to detect the dial's position. The microscope was mounted onto a Z stage (SGSP 26-50, Sigma Koki Inc., Tokyo, Japan), which was controlled by the PC to maintain the focal length when changing the magnification ratio. The Z stage was driven by a stepping motor with a positioning accuracy of 3 μm and a maximum drive speed of 30 mm/s. Depending on the change of the magnification ratio, the light source (LA-

HDF 5010, Hayashi Watch-Works Inc., Tokyo, Japan) was also adjusted to maintain the consistency of the light intensity.

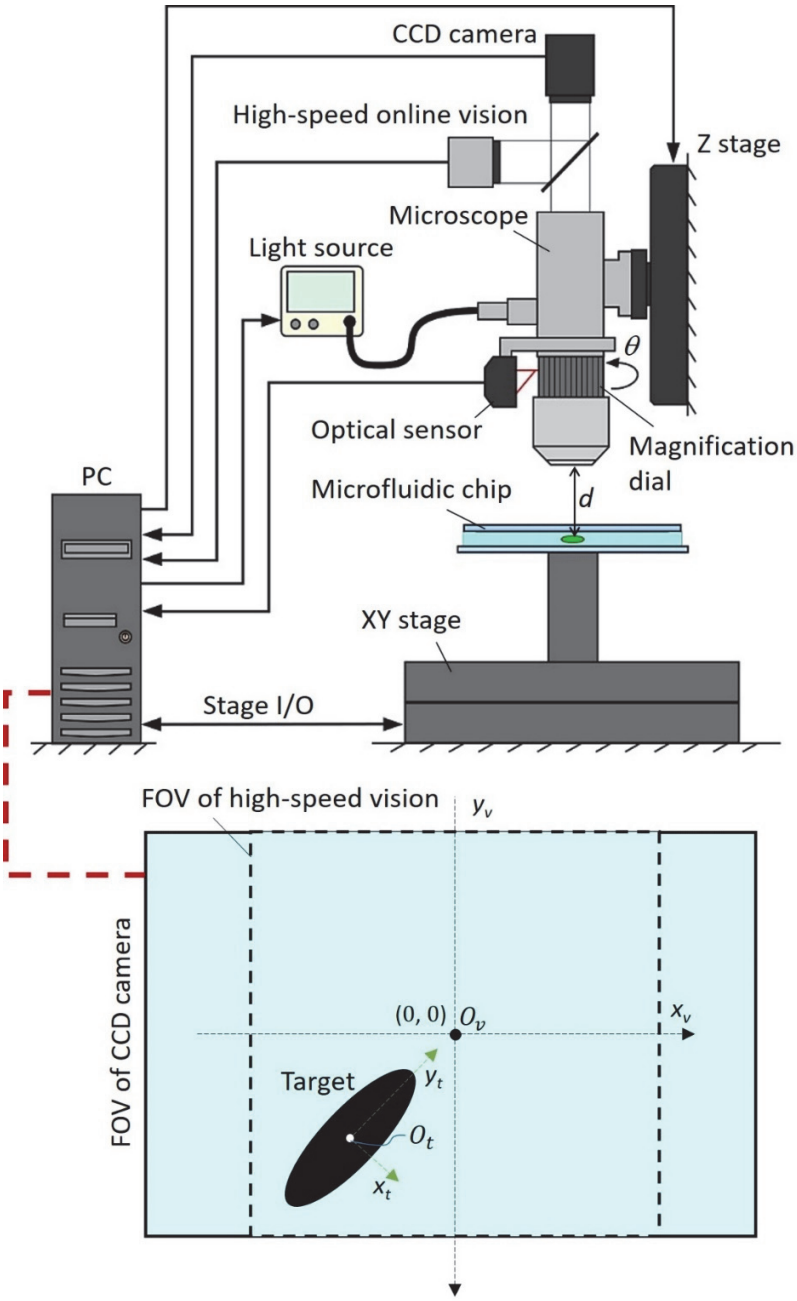

Figure 2.1: Main components and coordinates system of the developed observation platform. The subscripts *v*, *t* indicate the high-speed online vision coordinates, and the target coordinates, respectively.

The specific control method for the magnification ratio of the microscope will be detailed in Section 2.3. By obtaining the target position data from the online vision sensor, an xy stage (SGTMM03-065AH20A, Yasukawa Electric Inc., Kitakyushu, Japan) was controlled by the PC to maintain the microorganism in the FOV of the microscope. It was driven by a linear AC motor with a positioning accuracy of 200 nm and a maximum drive speed of 1500 mm/s. The target microorganism was introduced inside a microfluidic chip, made of a glass-PDMS-glass sandwich.

The complete block diagram of the tracking system is shown in Figure 2.2. The controller can be mainly divided into two sub-controllers, tracking controller, and magnification controller. The tracking controller uses an image feedback loop for position control of the xy stage. On the other hand, the magnification controller uses feedforward control to adjust three components that are required for achieving a variable magnification mechanism. It is important to note that there is a linking parameter between the two sub-controllers, which is the pixel pitch p. The pixel pitch is the distance from the center of a pixel to the center of the next pixel measured in millimeters, as shown in Figure 2.3. This parameter changes according to the change in the magnification ratio and is crucial for achieving a stable tracking control with online variable magnification. The control of the pixel pitch and other parameters required for variable magnification control will be discussed in the next section. The visual tracking algorithm will be explained in Section 2.4.

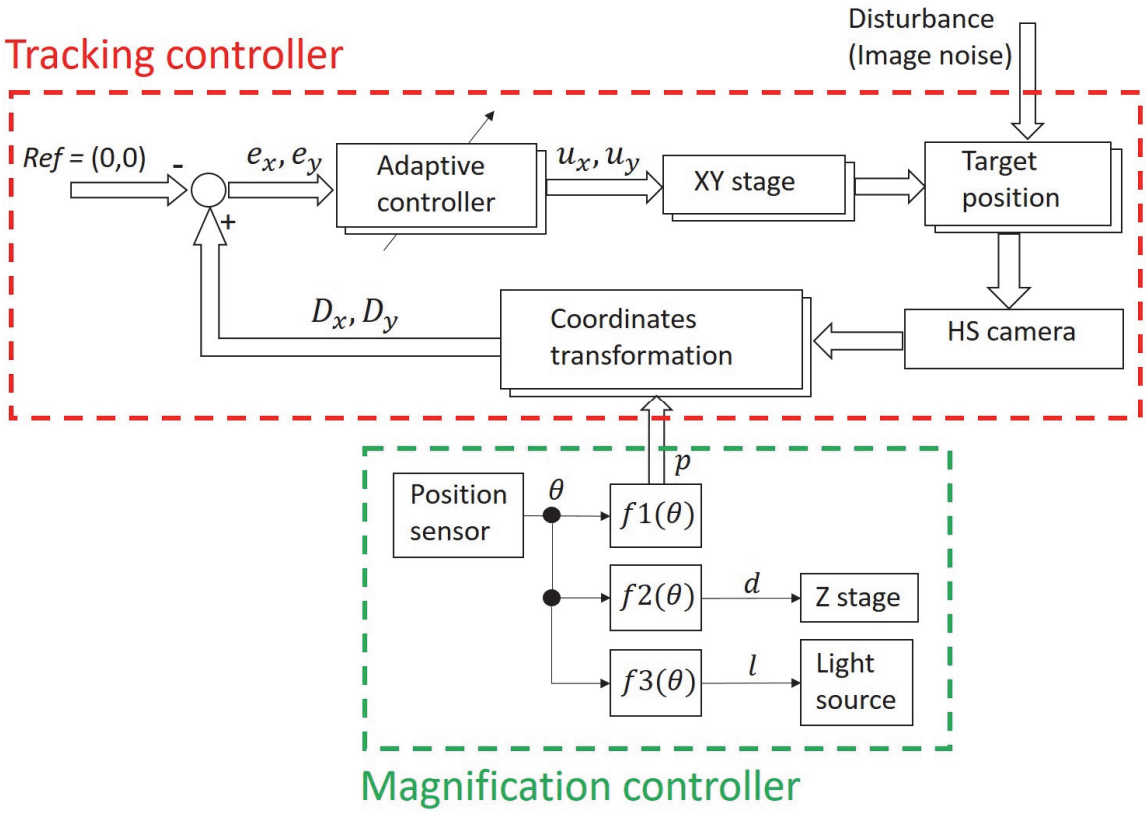

Figure 2.2: Complete block diagram of the developed observation platform.

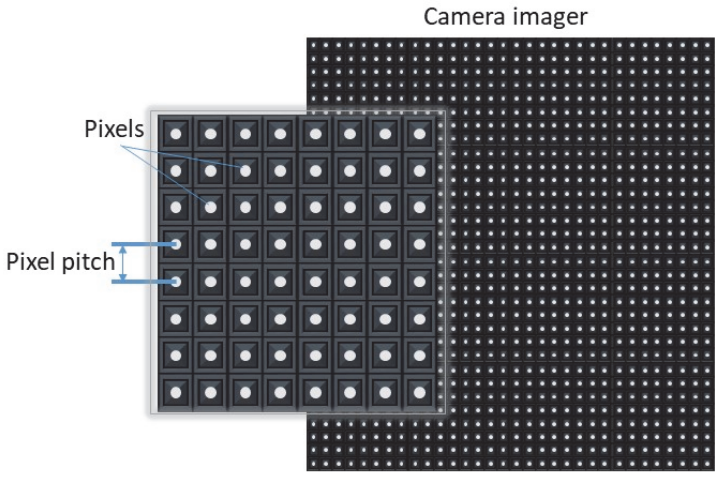

Figure 2.3: Definition of pixel pitch.

2.3 Variable Magnification Mechanism

To improve the efficiency of the motile microorganism investigations, it is better to start the experiment from a low magnification ratio to quickly find a target microorganism. The magnification ratio of the microscope is then changed seamlessly to a high magnification for obtaining high-resolution images. It is well known that changing the magnification ratio of the microscope would affect the quality of the image and could result in highly blurred and dim

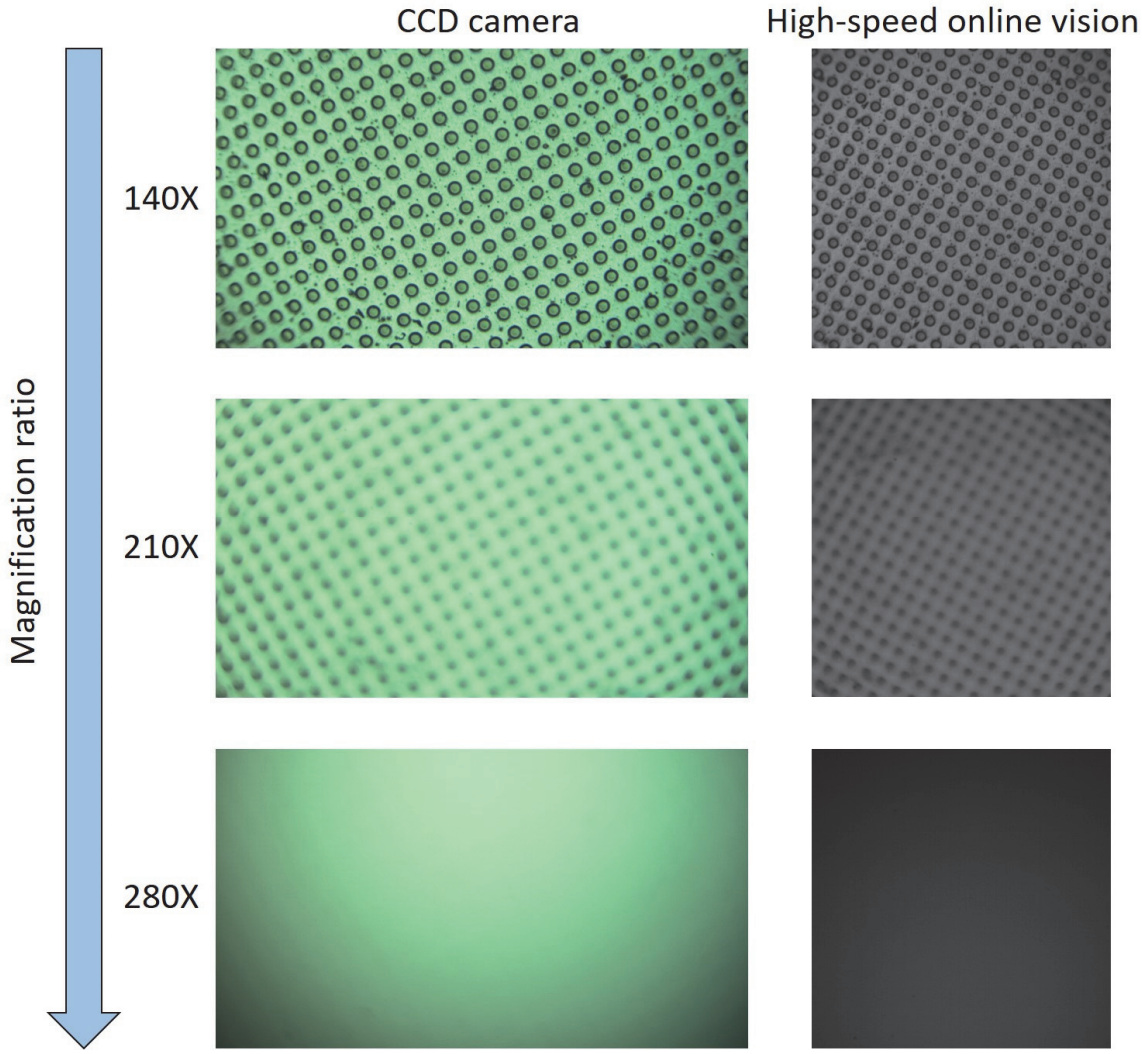

Figure 2.4: Effect of changing the magnification ratio on image quality without feedforward control.

images, as shown in Figure 2.4, which would also drastically affect the stability of the visual tracking control in later steps. Therefore, both the image quality and the target tracking control should be maintained while changing the magnification ratio. To realize this function, three main factors that affect the image quality and the tracking control continuity should be considered, as shown in Figure 2.2. These three parameters are the focal length *d*, the light intensity *l*, and the pixel pitch *p*, where only the pixel pitch has a direct effect on the tracking control and no effect on the image quality. In the developed system, the magnification ratio can be changed without replacing the lens by manually rotating a magnification dial on the microscope to zoom in and out. Because the magnification dial rotational degree θ indicates the currently applied magnification ratio, each of the parameters can be mathematically modeled as a function of θ as follows:

$$\begin{bmatrix} p \\ d \\ l \end{bmatrix} = \begin{bmatrix} f_1(\theta) \\ f_2(\theta) \\ f_3(\theta) \end{bmatrix}. \tag{2.1}$$

Therefore, real-time control of the three parameters would be achievable, allowing for a seamless change of the magnification ratio without affecting the image quality nor the tracking stability. The modeling functions were obtained by a calibration process for each parameter. To realize this method, at each calibration point, the pixel pitch was measured, and both the focal distance and the light intensity were adjusted and measured. At the same time, the rotational degree at each calibration point was measured using an optical rotation sensor in real-time. Using the calibration data, the mathematical models of the three parameters were obtained by fitting curves. The order of each polynomial was determined using the coefficient of determination (R^2), where the order was increased until $R^2 = 0.99$. The fitting curves for the

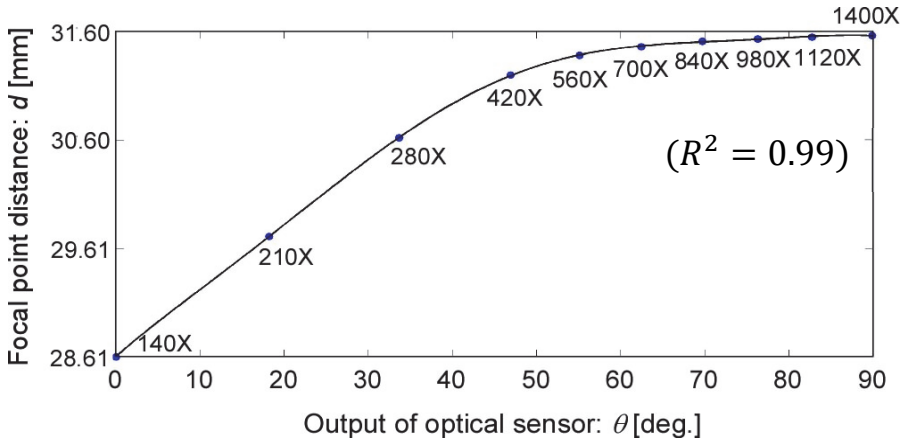

$d = f_2(\theta) = 0.0001\theta^3 - 0.0015\theta^2 + 0.0702\theta + 28.6101$

Figure 2.5: Relationship between magnification ratio (dial) and focal point distance of the microscope. The focal distance d is described as 3rd order polynomial of θ (The dial rotational degree measured by the optical sensor). The coefficient of determination R^2 is shown on the figure.

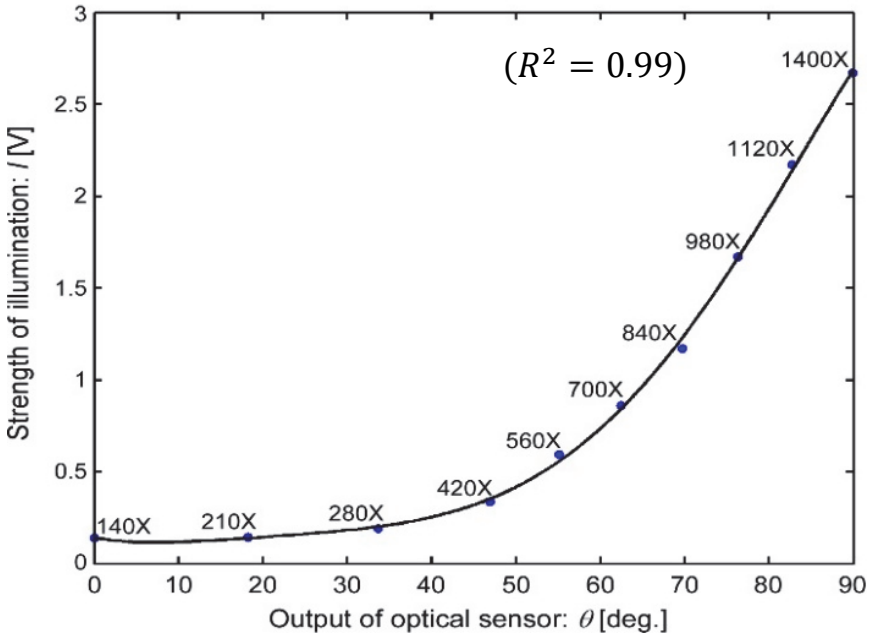

$I = f_3(\theta) = -0.0513\theta^5 - 0.1058\theta^4 + 0.1912\theta^3 + 0.7398\theta^2 - 0.8423\theta + 0.5083$

Figure 2.6: Relationship between magnification ratio (dial) and the light source illumination intensity. The illumination I is described as 5th order polynomial of θ (The dial rotational degree measured by the optical sensor). The coefficient of determination R^2 is shown on the figure.

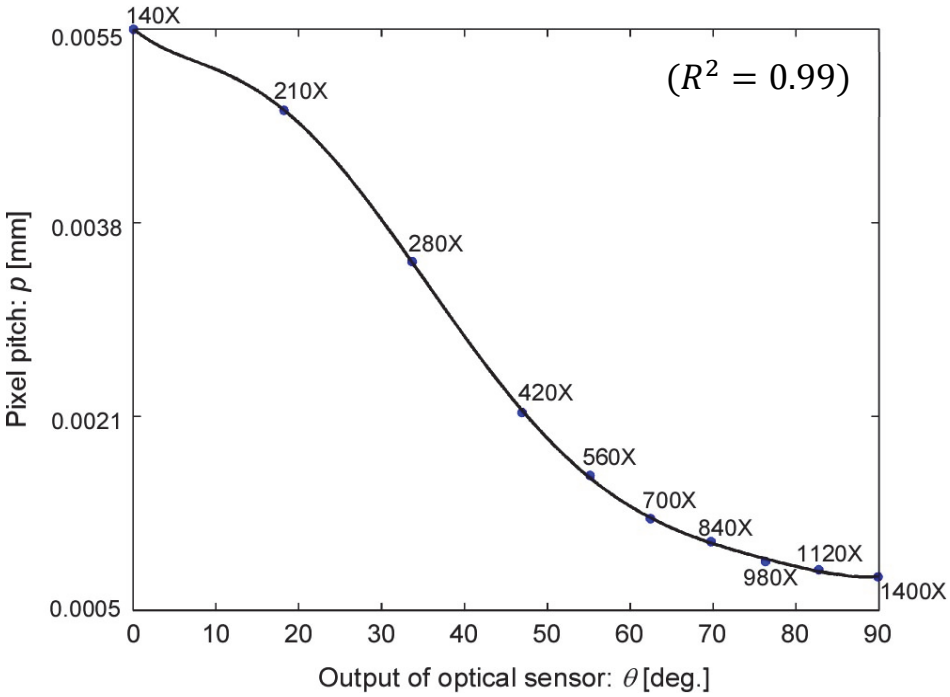

$$p = f_1(\theta) = 0.0001\theta^6 + 0.0001\theta^5 - 0.0006\theta^4 - 0.00003\theta^3 + 0.0014\theta^2 - 0.0018\theta + 0.0017$$

Figure 2.7: Relationship between magnification ratio (dial) and the pixel pitch of the HS camera. The pixel pitch p is described as 6th order polynomial of θ (The dial rotational degree measured by the optical sensor). The coefficient of determination R^2 is shown on the figure.

focal distance, light intensity, and pixel pitch, along with the curve equations are shown in Figures 2.5, 2.6, and 2.7, respectively.

To seamlessly change the magnification ratio, the optical sensor attached to the microscope measures the rotational degree θ of the magnification dial and sends this information to the controller, where the three parameters (p, d, and l) are calculated using the curve equations. The controller then sends commands to each of the Z stage and the light source to adjust both the focal distance and the light intensity. The pixel pitch is also adjusted simultaneously.

2.4 High-speed Visual Tracking Algorithm

2.4.1 Determining high-speed vision frame rate

In order to track the target, a sufficient number of image frames should be captured while the target passes through the FOV of the high-speed online vision. To determine the appropriate frame rate, the equation proposed in [63] was used:

$$FPS = \frac{s_i / w_{FOV}}{1 - s_i / w_{FOV}} v \tag{2.2}$$

where s_i, w_{FOV}, and v are the target size, FOV width, and relative velocity in terms of the body length per second ($v = vs_i$), respectively. This equation is specific for targets which lengths are smaller than the observation FOV and does not hold for the other cases where the target is equal or larger than the FOV. Figure 2.8 shows the results of the numerical simulation based on Equation (2.2). In this simulation, we set s_i = 200 μm and according to the FOV of the microscope, w_{FOV} was set from 1.4 to 0.21 mm. When the magnification ratio of the microscope was increased, w_{FOV} decreased and hence the required frame rate increased towards infinity. In addition, the speed of the target also affects the required frame rate, where higher speeds require higher frame rates.

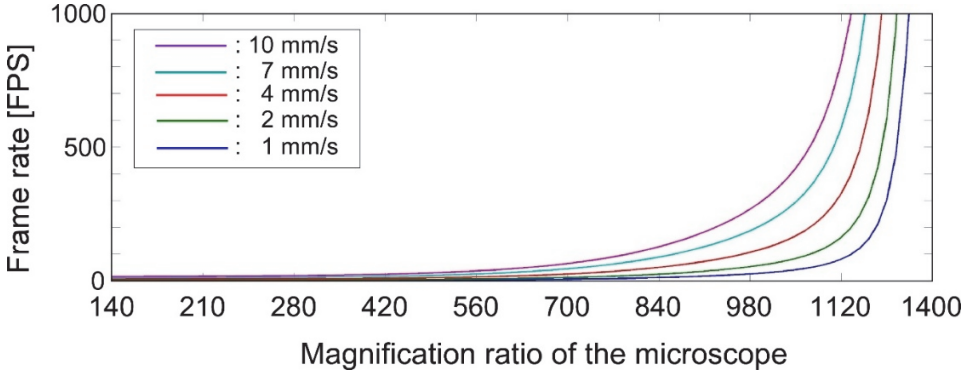

Figure 2.8: Required FPS for tracking.

2.4.2 Basic algorithm for tracking

The tracking control objective is to maintain the located swimming microorganism in the center of the microscope FOV. For this purpose, a visual servoing system was implemented. The servo system is composed of two components: 1) an online high-speed camera acting as a visual feedback sensor, and 2) a high-speed linear AC motor xy stage acting as an actuator. The vision sensor detects the position of the microorganism and feeds this information back to the xy stage controller that initiates the appropriate command in order to maintain the target in the center of the FOV.

In order to detect the target's position, a grayscale image captured by the vision sensor is converted into a binary image. In our algorithm, an adaptive thresholding technique [64] is used to adaptively change the threshold value to compensate for illumination variations in real-time. Although it requires much processing time compared to other adaptive thresholding algorithms, it proves to be very robust against sudden illumination changes. The center of gravity (COG) of the target (X_g, Y_g), as shown in Figure 2.9, can then be calculated from the 0th- and 1st-order moments of the binary image as follows:

$$M_{i,j} = \sum_x \sum_y x^i y^j I(x,y) \tag{2.3}$$

$$X_g = \frac{M_{1,0}}{M_{0,0}} \tag{2.4}$$

$$Y_g = \frac{M_{0,1}}{M_{0,0}} \tag{2.5}$$

In addition, the posture of the target ϕ can be obtained from the 2nd-order moment,

$$\phi = \frac{1}{2}\tan^{-1}\left(\frac{2M_{1,1}}{M_{2,0} - M_{0,2}}\right) \tag{2.6}$$

where $M_{i,j}$ represents the *i,j*-order image moment, X_g, Y_g represent the image COG coordinates, and $I(x, y)$ represents the pixel intensity at the index (x, y). The COG coordinates obtained from the image moments are represented in pixels. However, in order to feed this information back to the xy stage, it should be transformed into the metric scale. This will give us the microorganism coordinates in millimeter with respect to the center of the microscope's FOV. The transformation is expressed as in the following equation:

$$\begin{bmatrix} D_x \\ D_y \end{bmatrix} = p \begin{bmatrix} X_g - W/2 \\ Y_g - H/2 \end{bmatrix} \tag{2.7}$$

where D_x, D_y represent the distance between the image COG (the microorganism COG) and the center of the FOV in millimeters, and *W, H* are the image frame width and height, respectively.

At last, the position information obtained from the vision sensor will be used as feedback to drive the xy stage to keep the target microorganism in the center of the FOV. Adaptive control [65] was used in order to control the xy stage to compensate for friction and nonlinearities. The control law is described in the following equations:

$$u_x = K_x e_x \tag{2.8}$$

$$u_y = K_y e_y \tag{2.9}$$

where u_x, u_y are the control inputs, K_x, K_y are the adaptive gains, and e_x, e_y are the error signals.

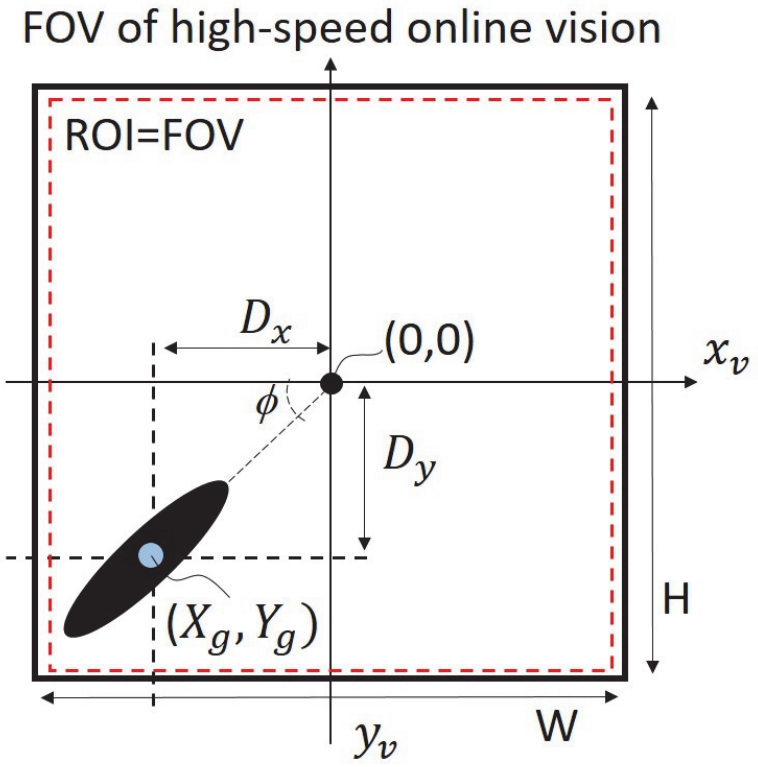

Figure 2.9: Basic algorithm for target tracking.

2.4.3 Noise elimination algorithm

The main difficulty in implementing a visual tracking system for motile microorganisms is a large number of image noise surrounding the target organism. Because there are many objects that can cause image noises in actual environments, it is quite difficult to track the target for a long time because the wrong position of the target COG is obtained. As a result, visual tracking fails immediately, especially in the case of a highly magnified environment. In fact, a microfluidic chip includes significant debris and bubbles together with motile microorganisms, and the edge of the chip recognized as a darker area should be considered as image noise. The highly magnified environment could aid in reducing the effect of surrounding image noise, although it does not guarantee a stable tracking in all situations. For instance, when we attempt to apply stimulation to the target using microtools, the calculated COG is moved from the target to the microtool, and the platform tracks the tool. This means that we cannot continue the observation of the target after the stimulation process. Although many effective algorithms to eliminate surrounding noise have been proposed and implemented in the field of image processing, the computing cost of their approaches is relatively high [66][67]. To realize a high-speed tracking system, many images must be processed in real-time, and the control thread must be maintained in the order of milliseconds by using a simple algorithm.

To overcome this dilemma, a simple visual tracking algorithm with high robustness is introduced by actively considering the characteristic of a high-speed online vision sensor. Here, two main assumptions, as shown in Figure 2.10, are taken in mind as follows; (i) because 3D movement of motile microorganisms is limited by a microfluidic chip, there is no overlap between each microorganism (no occlusion) during the observation; (ii) because a high-speed

online vision sensor is used, the difference between consecutive image frames is very small. These assumptions contribute to simplifying the image processing algorithm. Moreover, the shape of the target will be considered in the design of the algorithm. In fact, most shapes of motile cells range from circular to elliptical or even a simple thread shape. Therefore, the equation of a circle would make the base of the image processing algorithm. To guarantee a robust tracking as much as possible, the noise elimination algorithm is initiated when the magnification ratio is increased to a predefined value while tracking the target under stable conditions.

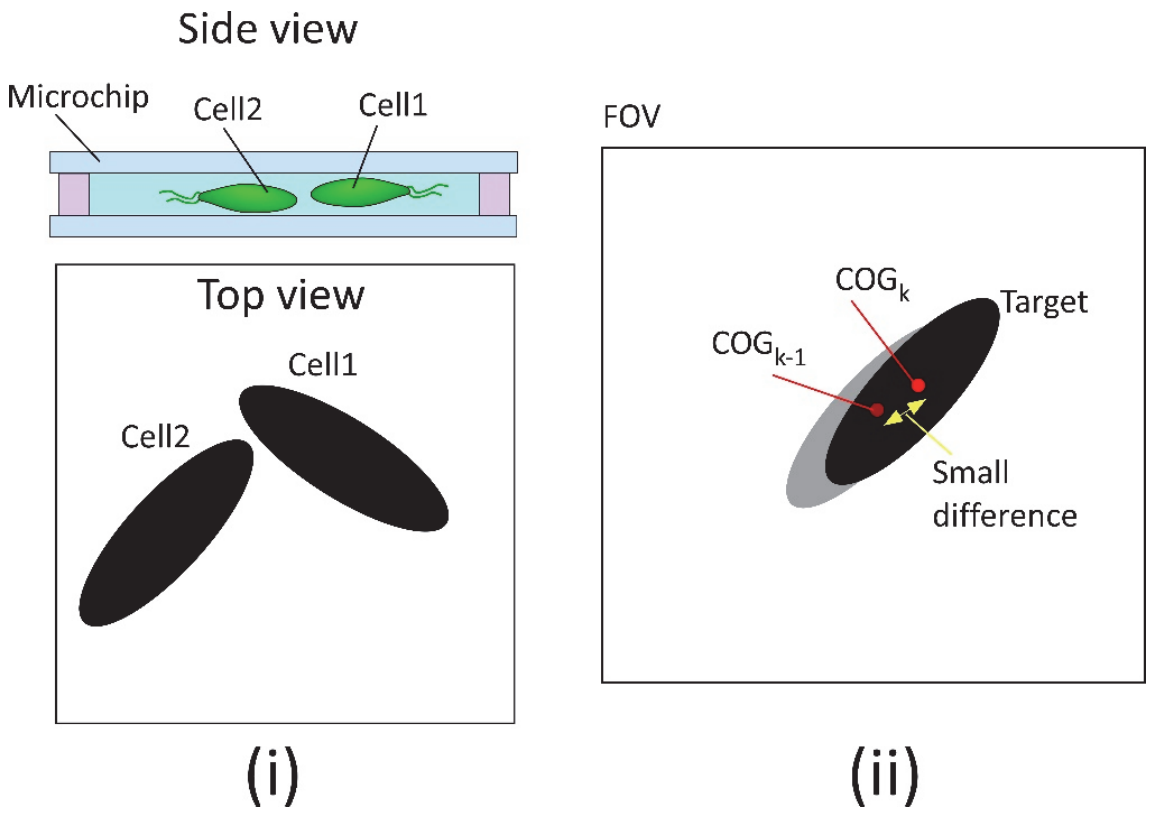

Figure 2.10: Assumptions for the design of a noise elimination algorithm.

The main concept of the algorithm is to create a region of interest (ROI) that is kept constantly around the vicinity of the target, as shown in Figure 2.11. As a first step, we can use the equation of a circle to change the shape of the ROI to a circular shape as follows:

$$\text{ROI: } (x)^2 + (y)^2 \leq r^2 \tag{2.10}$$

where r is the radius of the ROI circle and should be optimized to the size of the target. This equation would give us an ROI centered at the center of the FOV of the observation field at all times. Although this allows for the elimination of noise around the target, it fixes the ROI at the center of the FOV, which will drastically reduce the stability of the tracking control especially in case of fast targets. Therefore, instead of fixing the ROI at the center, the previous information of the target would be used, taking in mind the previously mentioned assumption

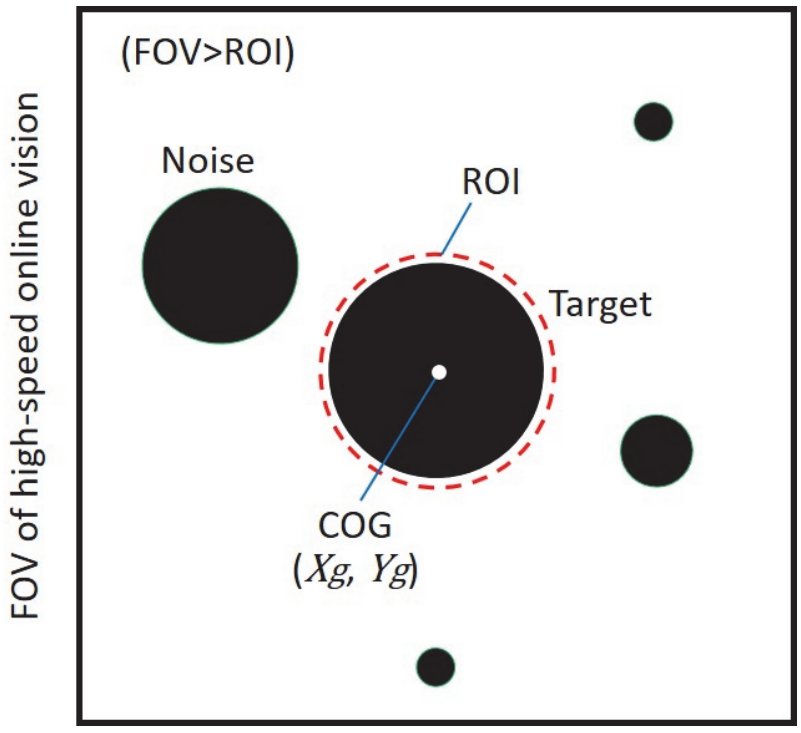

Figure 2.11: Basic concept of the noise elimination algorithm.

(ii), to keep the ROI close to the tracked target as much as possible. This can be achieved by using the target's COG information of the previous frame *k*-1, to establish the ROI at *k*-th image frame as follows.

$$\mathrm{ROI}^k: (x - x_g^{k-1})^2 + (y - y_g^{k-1})^2 \leq r^2 \tag{2.11}$$

where $k-1$ means the target's information in the previous frame.

As mentioned earlier, the shape of motile cells can range from circular to elliptical. This means that in order to be able to adjust to any possible shape, the use of the ellipse equation will give a more general way to establish the ROI. In this case, the COG information of the previous frame will not be sufficient alone, where we need the orientation information of the target. The final equation for determining the ROI shape and position is described as follows:

$$\frac{\{(x-X_g^{k-1})\cos\phi^{k-1}+(y-Y_g^{k-1})\sin\phi^{k-1}\}^2}{a^2}\frac{\{-(x-X_g^{k-1})\sin\phi^{k-1}+(y-Y_g^{k-1})\cos\phi^{k-1}\}^2}{b^2} = 1 \tag{2.12}$$

where *a* and *b* are the semimajor axis and the semiminor axis of the ellipse, respectively. In fact, by changing the values of *a*, *b*, and ϕ, the equation can cover the probable range of shapes for most motile cells, as shown in Figure 2.12. By using this equation, the ROI for image processing is shrunk to be around the target cell, as shown in Figure 2.13. In other words, by using the previous frame's information (COG and posture of the target) to determine the ROI for the current frame, we can reduce surrounding image noise and processing cost simultaneously. Although similar techniques have been used in other works with high-speed vision systems [68][69], these systems did not have a magnification changing mechanism and did not focus on long-time target tracking.

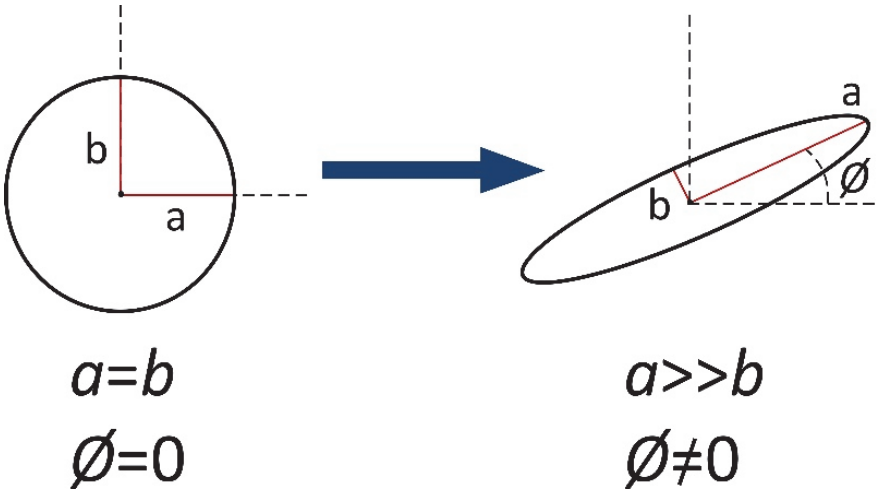

Figure 2.12: Target shapes that the noise elimination algorithm can cover.

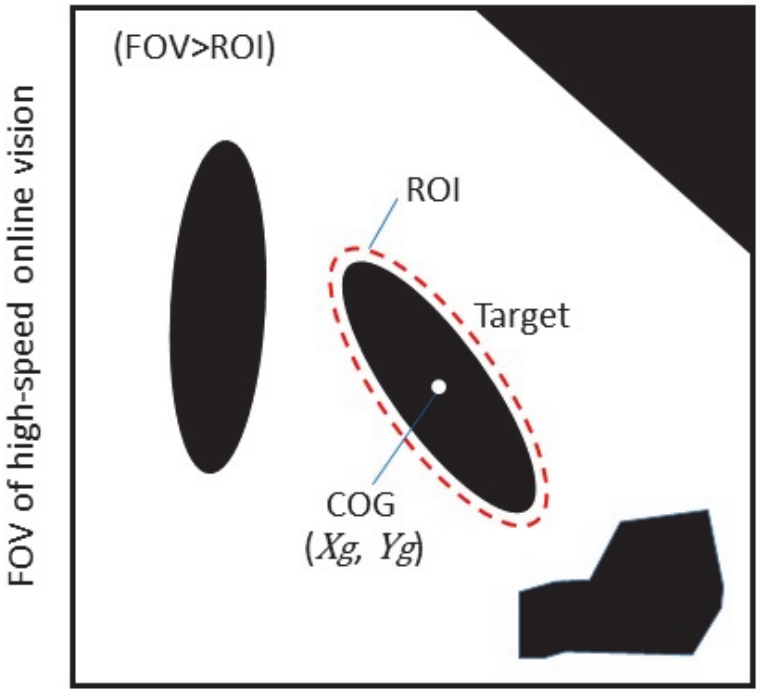

Figure 2.13: Noise elimination approach using an elliptical ROI.

2.5 Evaluation Experiments

2.5.1 Efficiency of variable magnification on searching time

To clarify the efficiency of the magnification ratio control in reducing the searching time for the target microorganism, the time required to search for a target has been confirmed. In this experiment, a number of polystyrene beads were placed on a glass substrate mounted under the microscope to simulate actual targets. The beads were scattered within a 10 × 10 mm square around the microscope's FOV. The xy stage was then moved to find a target bead in a Lissajous curve trajectory:

$$S_x = A\sin(2\pi f\alpha) \tag{2.13}$$

$$S_y = A\sin(2\pi f\beta + \pi/2) \tag{2.14}$$

where S_x, S_y are the position references for the x-axis and the y-axis of the stage, respectively, A is the maximum amplitude that matches the searching area length and width, and α, β are two constants. Consequently, the searching was terminated judging by the target area (the number of black pixels in the binary image). The searching experiment was repeated using several magnification ratios available in the platform, and the time required for each case was recorded. The FOV dimensions of the online vision ranged from 1408 × 1408 μm to 202 × 202 μm. A total of five searching experiments (n=5) were done for each magnification ratio and the mean value for each case was calculated. The polystyrene beads were all steady and had the same position with respect to the FOV in all cases to have a fair comparison. Figure 2.14 shows the searching time required for each magnification ratio. As we can see from the figure, it is clear that using a lower magnification ratio drastically reduces the required searching time, and hence

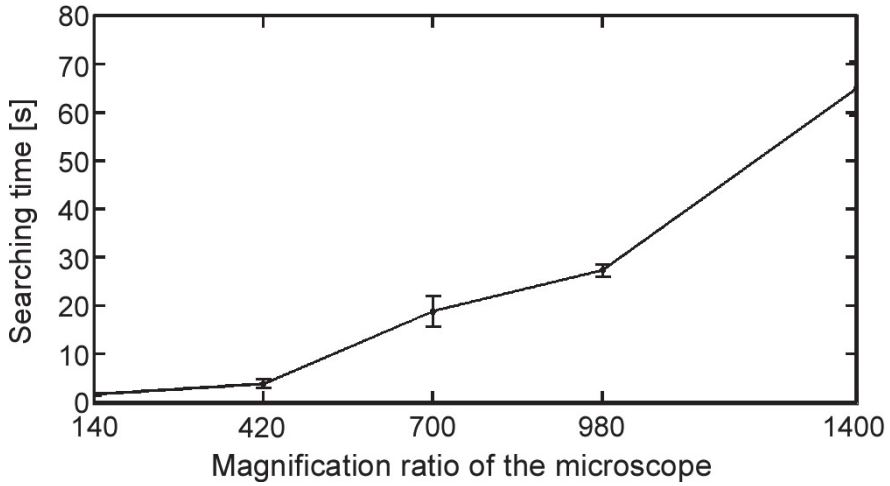

Figure 2.14: Magnification ratio control efficiency in reducing the searching time required to find a target

reducing the total experimental time, which increases the efficiency and repeatability of the experiment.

2.5.2 Validation of image quality for tracking purposes

The performance of the focal point control and its effect on image quality and image processing was verified. According to the fitting curve obtained from the measured data, as shown in Figure 2.5, the position of the microscope (Z stage) was controlled in synchronicity with the rotation of the magnification dial, which was changed manually. Figures 2.15(a) and (b) show the images (256 × 256 pixels) captured by the high-speed online vision without and with the focal point control, respectively. In this experiment, a polystyrene bead with a diameter of 100 μm was used as an artificial marker and placed at the center of the FOV. From this result, it was confirmed that the system can continuously observe the object at different magnification ratios in case of the focal point control. The effect of focal point control on image processing was also confirmed. Figures 2.15(c) and (d) show the binary images of the object obtained as a

result of the image processing. When changing the magnification ratio, the high-speed online vision and the CCD camera could not adapt to the intensity change of the illumination, even by changing the threshold in real-time. Therefore, the light source was controlled to obtain the same light intensity at every magnification ratio. Figure 2.15(d) clearly shows the effectiveness of the intensity control of the illumination.

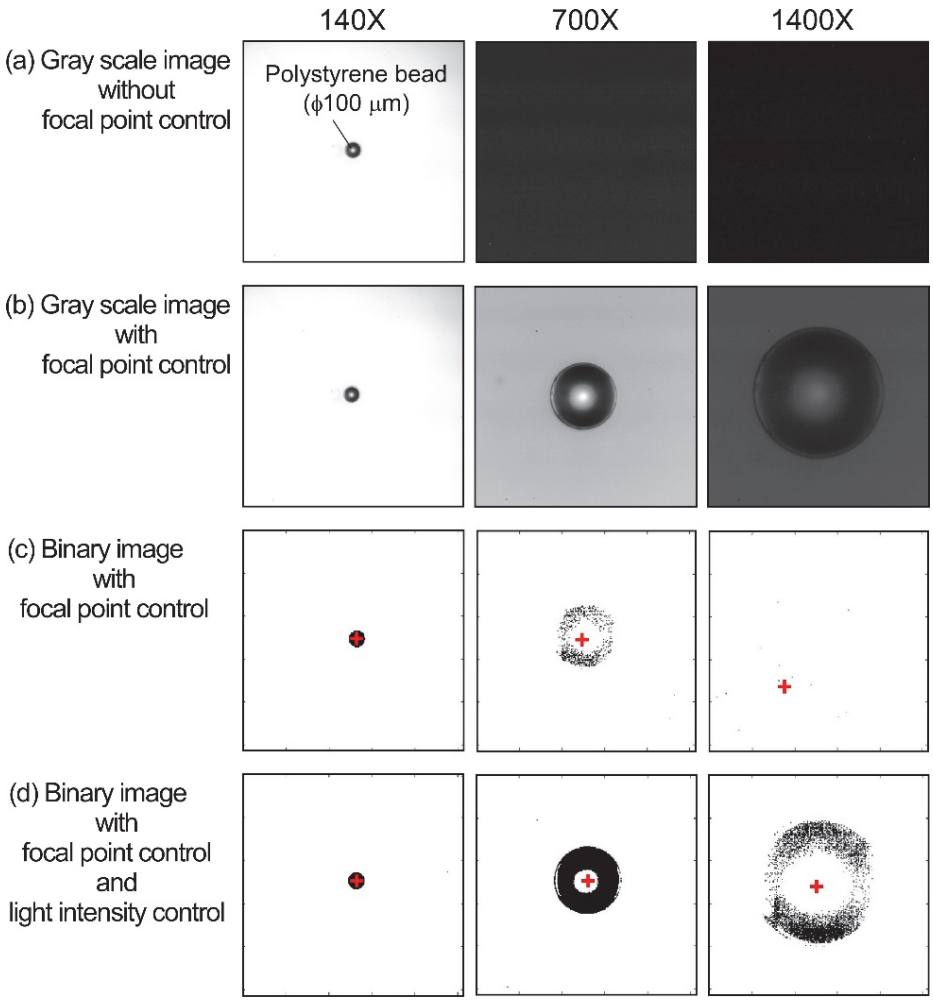

Figure 2.15: Experimental results to confirm effectiveness of focal point control and image processing with light intensity control.

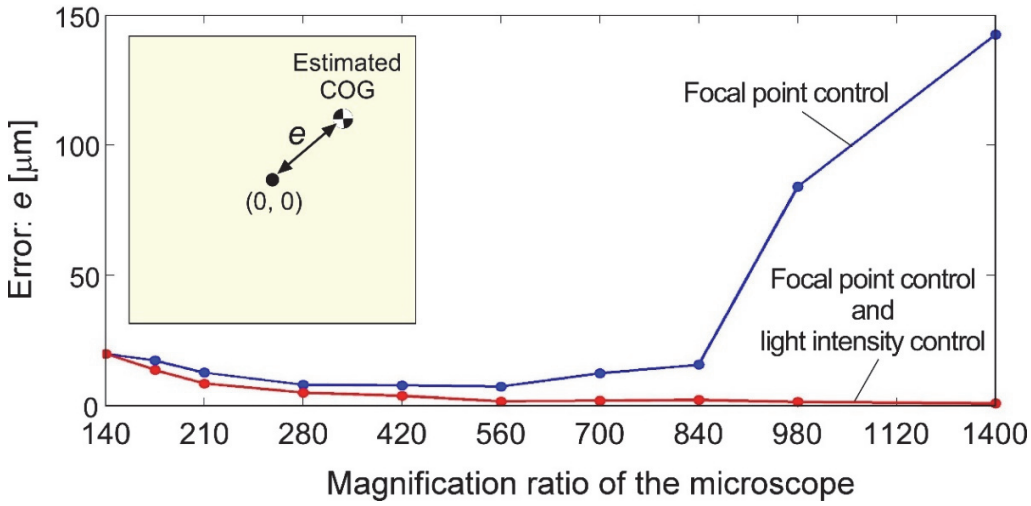

Figure 2.16: Evaluation of image processing error using the high-speed online vision.

Figure 2.16 summarizes the estimation error of the COG of the object by the image processing in Figures 2.15(c) and (d). The estimation error e is the distance in micrometers between the center of the FOV and the estimated COG of the image. From this result, it was also confirmed that when the magnification ratio and light intensity are changed, the proposed method maintains the accuracy of the image processing.

2.5.3 Configurations of high-speed online vision

The tracking system is mostly affected by the high-speed online vision configurations. Since the captured frames are processed in real-time, it is essential that we carefully choose the image resolution and FPS in order to select the best trade-off between performance and speed. For this purpose, the image processing time was investigated in different cases and the appropriate configurations were determined.

The experimental setup is shown in Figure 2.17. To investigate the camera processing time, a light emitting diode (LED) was placed under the microscope FOV. The LED was connected

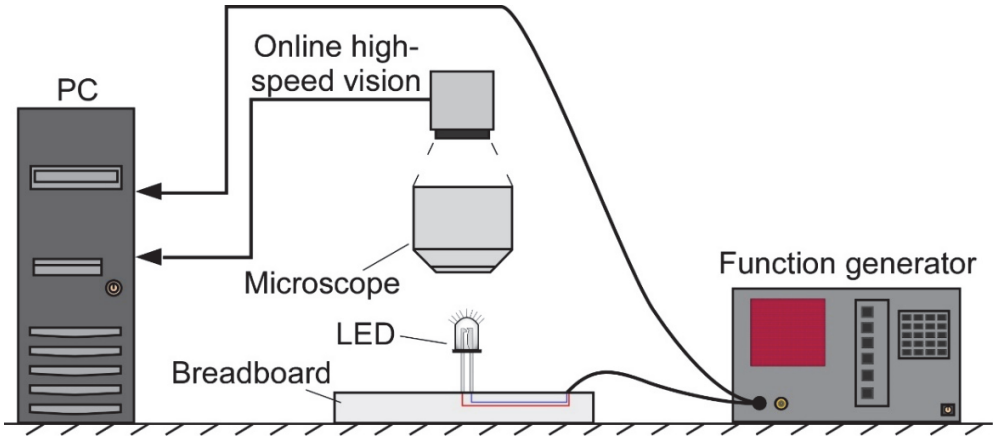

Figure 2.17: Experimental setup for investigating the processing time.

to a function generator and a voltage pulse train was applied, so the LED would turn on and off according to the frequency of the applied voltage, which was set to 1 kHz. Therefore, the illumination of the FOV would have the same frequency. The illumination change was captured by the high-speed online vision and the images were saved in the PC memory. At the same, the function generator applying the pulse train was connected to the PC through an analog-digital converter (ADC), and the applied voltage data was also saved in the PC memory with a sampling time of 1 msec. The images taken from the high-speed online vison were reconstructed into a waveform that is similar to the one generated by the function generator. This was achieved by calculating the mean value of the aggregated grayscale intensity of the total image as in the following equation:

$$m_k = \frac{\sum_i \sum_j I(i,j)}{W \times H \times I_{max}} \tag{2.13}$$

where, m_k is the grayscale mean value of frame k, $I(i,j)$ is the grayscale pixel intensity at the index i,j, and I_{max} is the maximum grayscale pixel intensity.

For comparison purposes, two situations were investigated. The first situation was without image processing on the high-speed online vision images, and the second situation was with applying the image processing algorithm explained in Section 2.4.2, and one example of each situation will be shown. In these two examples, the high-speed online vision configurations were identical so the only effective factor would be the presence or absence of image processing. The resolution of the vision was set to 512 × 512 pixels, and the frame rate was set to 500 FPS. The images mean value is plotted against the function generator voltage, as shown in Figures 2.18 (without image processing) and 2.19 (with image processing). As mentioned earlier, the sampling time of the PC was 1 msec and the function generator pulse frequency was 1 kHz, which implies that 1000 samples of the image mean value should be obtained in each voltage pulse (i.e. each one second). This is true for the signals in Figure 2.18, where one pulse contains 1000 samples. However, if we look at Figure 2.19, we can clearly see that in one pulse only 150 samples were obtained. This result tells us that, if 512 × 512 image size with 500 FPS were used the image processing algorithm would take 6 msec, and hence only 150 samples would be obtained in one second.

By conducting the same experiment and changing the camera's image resolution and frame rate, the processing time for each configuration can be confirmed. Figure 2.20 shows the obtained processing time against the image resolution and the camera's frame rate. Based on these results, the image resolution was set to 256 × 256 pixels because increasing it more results in a drastic increase in the processing time. As for setting the camera's frame rate, the figure shows that it does not have a large effect on the processing time, therefore, a high frame rate can be chosen. However, choosing frame rates higher than 500 FPS required a much stronger light source, which is not available in the current system, and the frame rate was set to 500 FPS.

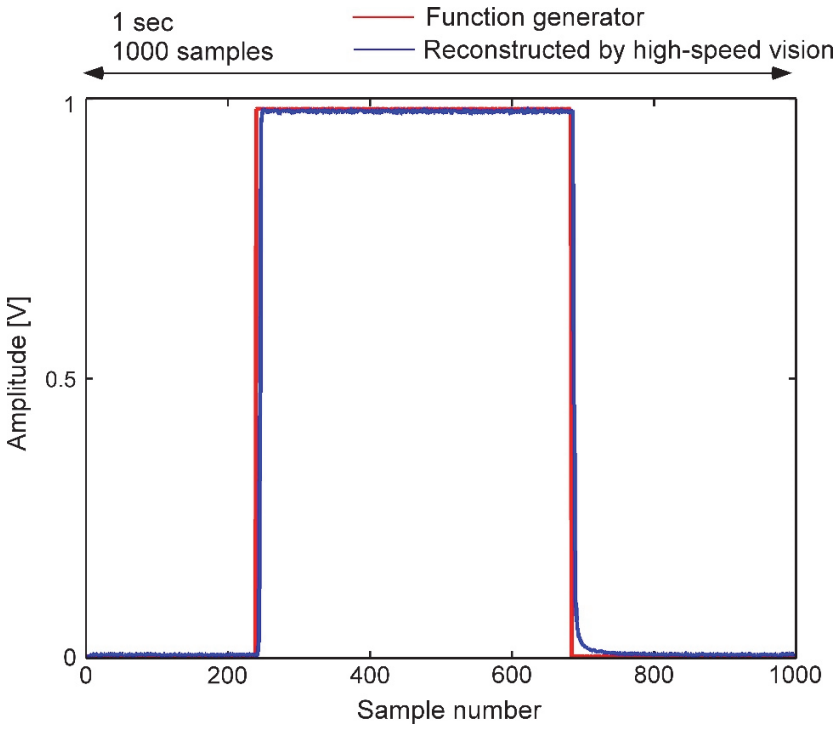

Figure 2.18: Waveform in case of no image processing at 500 FPS.

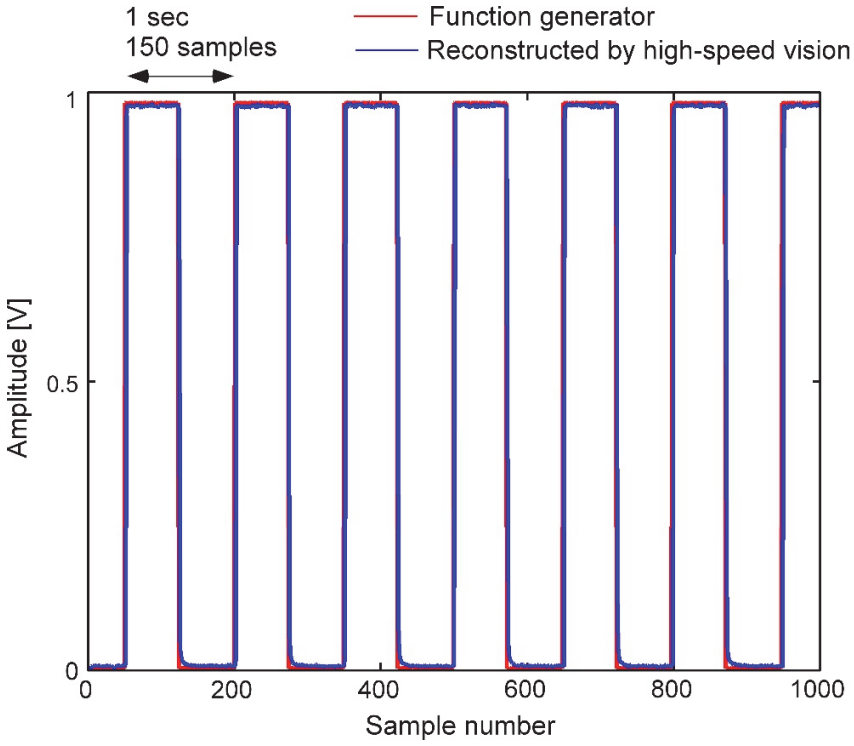

Figure 2.19: Waveform in case of applying image processing at 500 FPS.

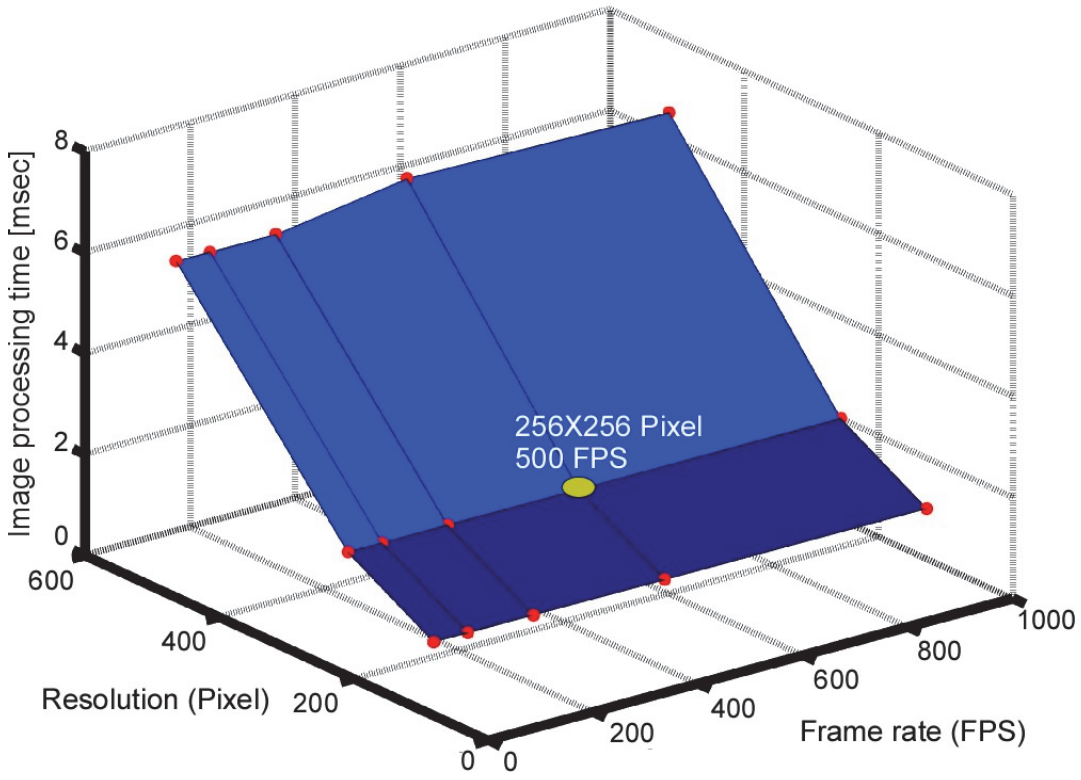

Figure 2.20: Image processing time consumption.

2.5.4 Limitations of the tracking system

The maximum tracking performance of the developed visual tracking system was first evaluated under the ideal (noiseless) condition. In this experiment, another small xy stage was mounted to simulate the movement of the motile cell, as shown in Figure 2.21(a). A polystyrene bead with a diameter of 100 μm was attached to the tip of the stage under the microscope as a tracking target and moved in a 2.0 mm circular trajectory at different moving velocities. The target was then tracked to the center of the microscope's FOV under the fixed magnification ratio. The tracking error, which is the distance between the center of the FOV and the target position, as shown in Figure 2.21(a), was calculated, where each plotted point in Figure

2.21(b)(c) is the mean value of 1000 samples, and the error bars show the standard deviation of each 1000 samples. Regarding image processing, two cases were demonstrated. In the first case, the entire FOV of the microscope was considered as the ROI for the image processing (Figure 2.21(b)). In the second case, a selected ROI as explained in Section 2.4.3 was implemented ($a = b = 20$ pixels, ϕ=0 in Equation (2.12), circle ROI) and performed (Figure 2.21(c)). The ROI parameters where determined based on the size of the target, where in this case the ROI is slightly larger than the polystyrene bead size when viewed under 140× magnification. In both cases, the computational cost of the image processing was within 3 msec.

From these results, it was confirmed that the tracking error increases with increasing target velocities, and the tracking failed at relatively large magnification ratios with target velocity greater than 15 mm/s. On the other hand, at target velocity less than 10 mm/s, the tracking performance was maintained in both cases even if the magnification ratio reached 1400×. Through the experiment, we confirmed the limitation of the target tracking on the developed platform. In the case of a noiseless environment, there was a small difference in the tracking performance between the two cases of the image processing method.

Next, the robustness of the implemented tracking method was evaluated. A noisy image situation was simulated by adding software-generated noise to the captured image in each frame. The generated noise had a circular shape with image coordinates and size that were generated and updated randomly in each frame. In this experiment, the assessment was based on the duration of tracking with the magnification ratio of 140×. Examples of noisy images are shown in Figure 2.22(a). Four different noisy situations were tested, each of which had different numbers of generated noise circles. The four situations were very low noise, low noise, medium noise,

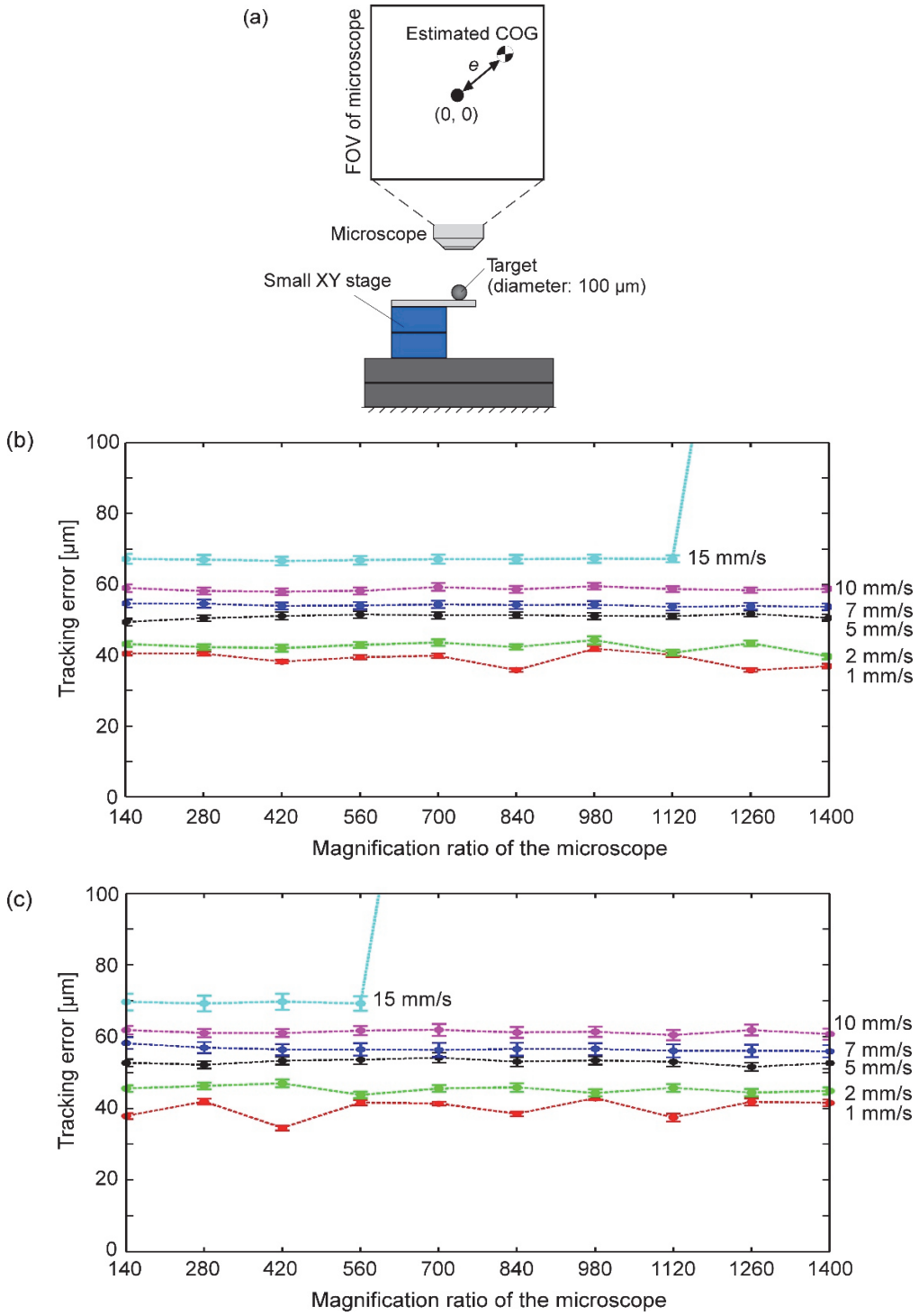

Figure 2.21: Tracking performance evaluation of developed platform. (a) Experimental setup; (b) Tracking error with basic image processing method; and, (c) Tracking error with implemented noise elimination method.

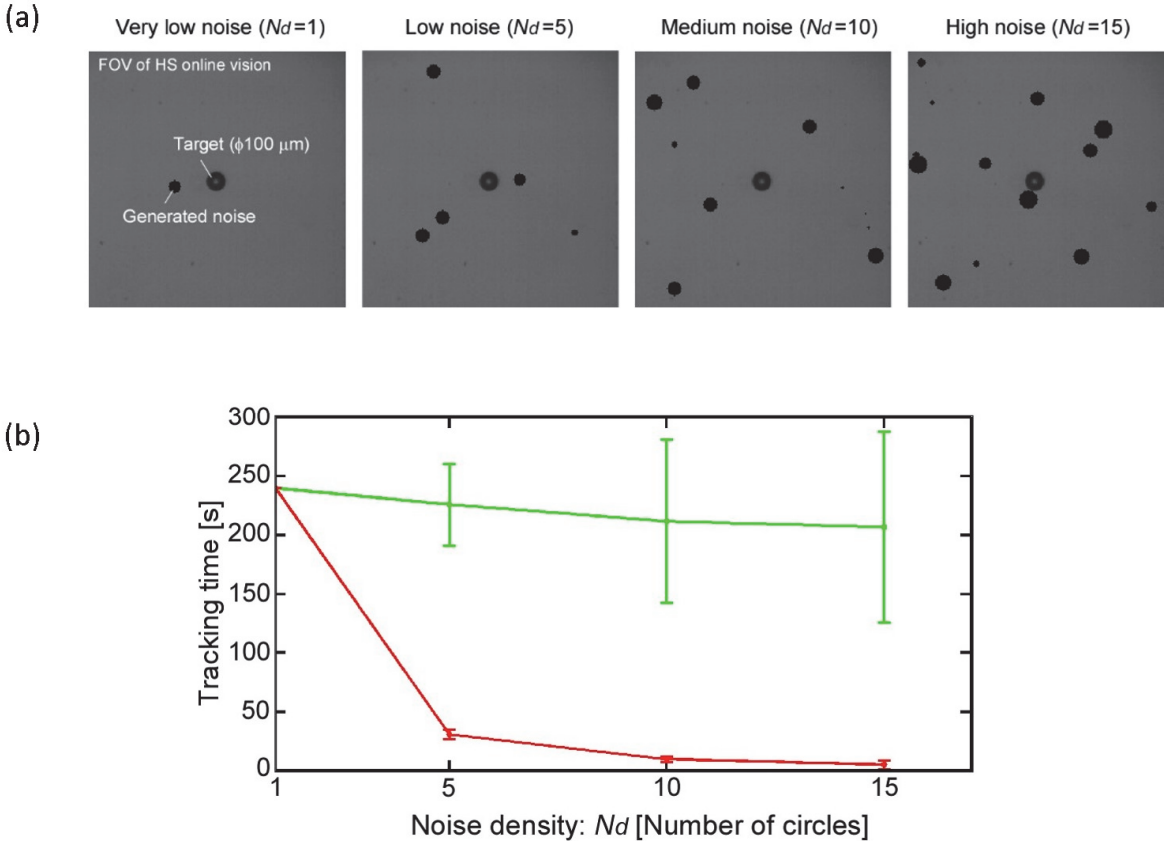

Figure 2.22: Robustness evaluation of target tracking in noisy environment. (**a**) Examples of four different noisy situations; (**b**) Total tracking time with basic image processing method (red) and noise elimination image processing method (green).

and high noise density, where the numbers of circles in each situation were 1, 5, 10, and 15, respectively. It is important to note that the noise was restricted from being generated in coordinates that caused it to overlap with the target because this situation is outside the scope of this work.

Figure 2.22(b) shows the experimental result. For image processing, two cases were demonstrated with the same conditions as the previous experiment. A total of six tracking experiments were performed for each noise situation, and the total tracking time was plotted.

As we can see from the result, when the entire FOV of the microscope was used as ROI (red line), the tracking time was drastically affected in a negative way by the increment in noise density. On the other hand, the effect of the noise density was reduced, and the tracking time was maintained by the implemented approach (green line) even in a highly noisy situation. In the second case, the implemented approach, the ROI was updated as explained in Section 2.4.3 ($a = b = 20$ pixels, ϕ=0 in Equation (2.12), circle ROI) in a noiseless environment. The image noise was then generated after having a stable tracking situation. This result clearly shows the robustness of the implemented tracking algorithm, which has high potential to maintain the target tracking for a long time with a low computational cost. It is worth mentioning that the tracking time in the first case (red line) can be maintained for a long time when N_d=1. This is due to the COG being located continuously on the line connecting the target and the random noise object since only one noise object exists.

2.5.5 Tracking with magnification

Figure 2.23 shows the time response of the target position during the tracking control with magnification. In this experiment, the target was moved at a velocity of 1 mm/s along a 2.0 mm circular trajectory. When changing the magnification dial from 140× to 1400× and from 1400× to 140× by manual operation, the tracking was continued up to 7 sec. The time required to change from the lowest magnification ratio (140×) to the highest magnification ratio (1400×) was approximately 500 msec. After that, the tracking target was lost when the magnification ratio was changed quickly (within 200 msec). Through the experiments, the basic characteristics of the developed platform were confirmed, which included robust and high-speed image processing, stage control, and focal point control.

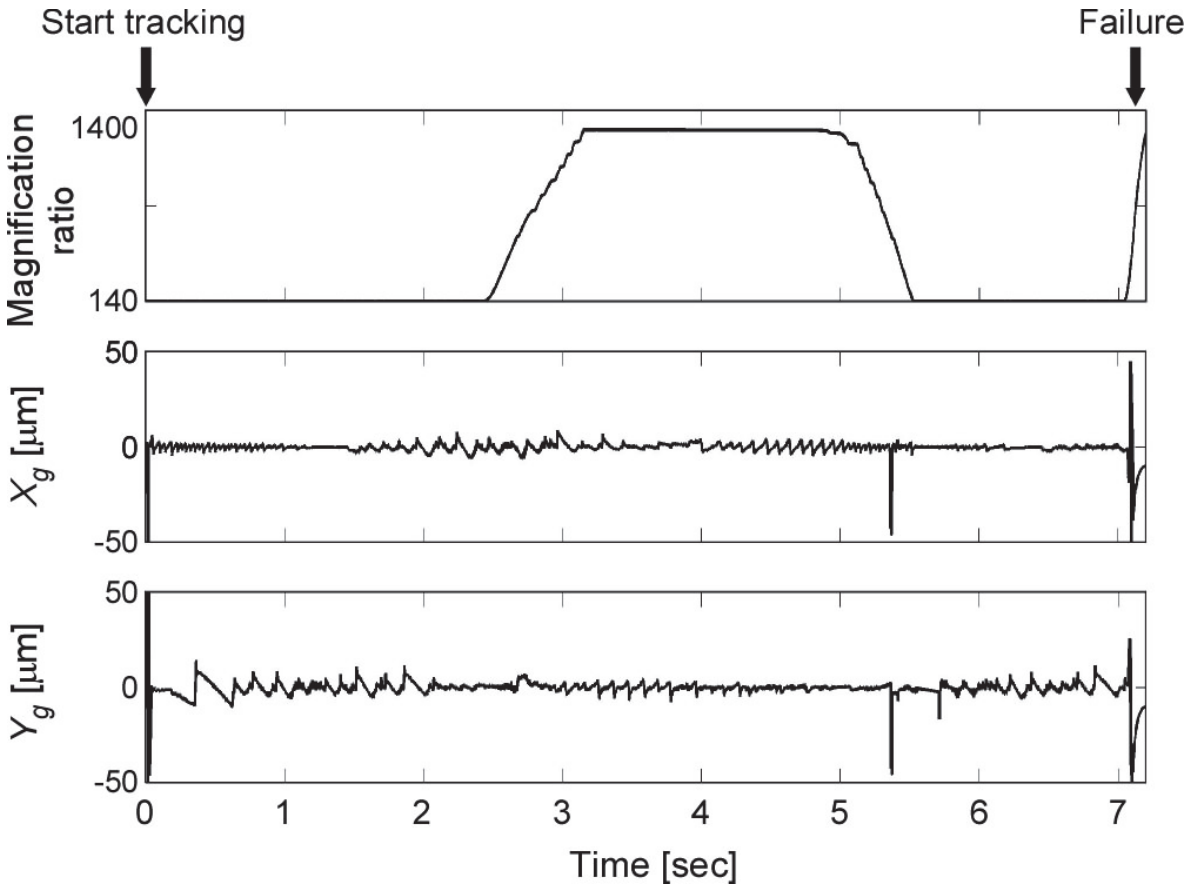

Figure 2.23: Results of target tracking with magnification control.

2.6 Concluding Remarks

In this chapter, the design and implementation of the observation platform were explained. Based on the required specifications, a high-speed tracking system with variable magnification mechanism was proposed. To realize robust real-time target tracking with variable magnification, the block diagram of the tracking and magnification controllers were shown, including the pixel pitch, focal length, and illumination control for the adaptive tracking. To achieve long-time tracking, the image noise was eliminated using a simple image processing technique that utilizes the small spatial difference between consecutive frames. Finally, basic experiments were conducted to evaluate the performance of the variable magnification mechanism and the high-speed tracking system. The platform could successfully track targets that move with a velocity of up to 10 mm/s even when using the highest magnification ratio available in the platform regardless of the presence of image noise, which showed the robustness of the observation platform.

Chapter 3

Stimulation Platform

In this chapter, the second step in developing an investigation platform for a single motile microorganism, the stimulation platform, will be introduced. The difficulties of applying stimulation to a freely swimming motile cell will be first discussed, and the method to overcome these difficulties will be introduced. A stimulation platform using thin microtools driven by a magnetic compensation method will be developed. The specific design of the stimulation platform will be described and the effectiveness of the new positioning method for the microtools will be confirmed through both numerical simulation and basic experiments.

3.1 How to Realize Stimulation of a Motile Cell?

There are a number of ways to stimulate a motile microorganism depending on the type of stimulation. In this work, achieving mechanical stimulation has the highest priority. As discussed in Chapter 1, the major difficulty in mechanical stimulation is the ability to touch the target cell. This means that the tool should be actuated inside the environment of the cell, where many factors come into play, specifically the fluidic disturbance. Conventionally, the target cells are introduced inside a droplet for observation and investigation, as shown in Figure 3.1(a).

Although this method is very simple, it does not allow for the control of the thickness of the environment, which is very crucial for achieving the continuous observation of the cell in a 2D environment. In this case, the height of the aquatic environment is either very small restricting the movement of the cell or is very large not limiting the vertical movement.

In order to be able to control the height of the environment, a closed microchip can be used, as shown in Figure 3.1(b). Consequently, the closed nature of the chip necessitates the use of untethered microtools (microrobots) controlled by an external force such as magnetic fields. By carefully designing the microrobot and its driving method, high positioning accuracy with high output force can be achieved, as proposed by Hagiwara et al. [70]. However, these microrobots were only used for floating cells applications such as oocytes and were not designed

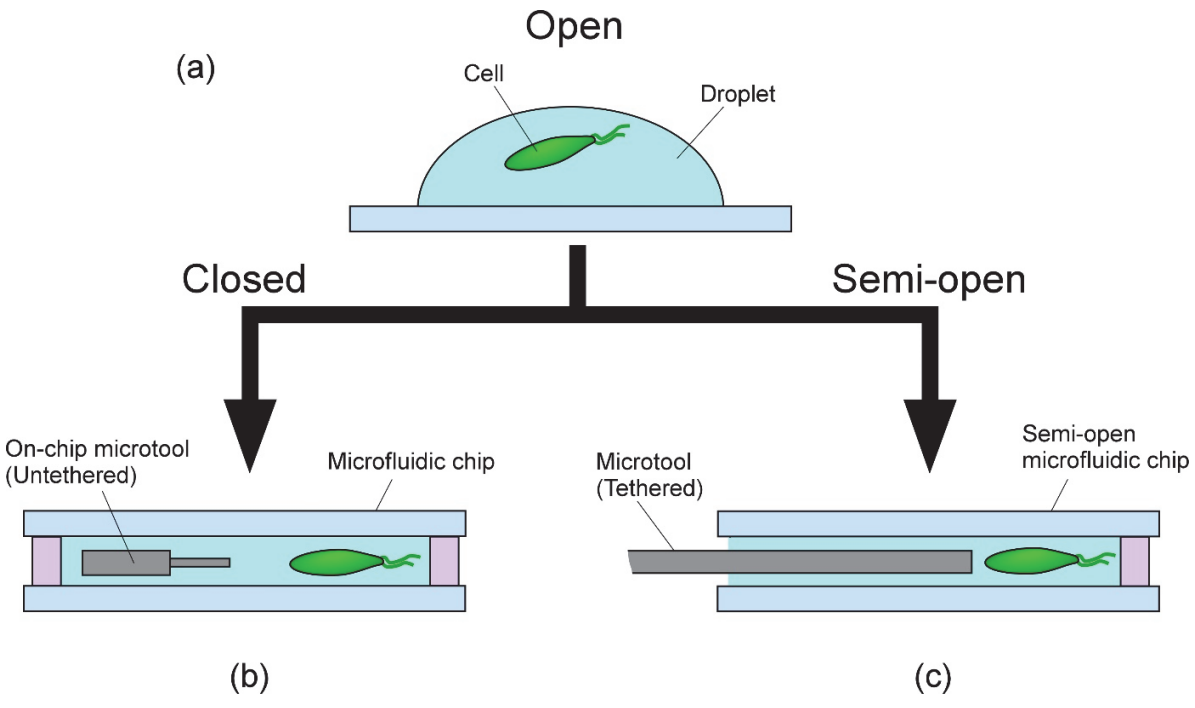

Figure 3.1: Different environmental setups for cell investigation. (a) Conventional open environment, (b) Closed environment using a microfluidic chip, and, (c) Semi-open environment for the insertion of tethered microtool.

for continuously moving targets such as motile cells. In fact, when the microtool is completely untethered and actuated by an external force, any unexpected noise such as vibrations could cause a driving failure as the microrobot constantly moves. The recovery from failure would be problematic even when using electromagnets as driving units, because of the difficulty in acquiring the position information of the microrobot after failure, especially when using image feedback for position control of the microrobot in highly magnified environments.

The use of tethered microtools could solve the previous problems. The tethered nature of the microtool would drastically reduce the probability of a driving failure. However, a completely closed microchip cannot be used in this case. Therefore, one side of the microchip should be left unsealed to allow for the insertion of the tethered tool, as shown in Figure 3.1(c). The main merit of using tethered microtools is that the tool can be directly fixed on the driving stage. The stage and the microtool would have the same coordinate system and hence the position information of the tool can be acquired easily. In fact, it is highly advantageous to make the position information of the tool available at all times, particularly when dealing with continuously moving targets such as motile cells, which increases the chances of the recovery from driving failure.

As discussed in Chapter 1, the size of the microtools greatly affects the stimulation procedure depending on how much fluidic disturbance is generated by the tool. Figure 3.2 shows a comparison between the fluidic disturbance generated by microtools with different sizes. When applying stimulation to a motile microorganism using a relatively thick microtool, generated fluidic disturbance is large and it would drastically affect the position of the target cell, as shown in Figure 3.2 (a). In contrast, a relatively thin microtool would greatly reduce the amount of fluidic disturbance generated when applying stimulation, and hence stimulation

could be applied because the position of the target motile cell would not be affected, as shown in Figure 3.2 (b).

The stimulation of the motile microorganism will be conducted inside a microfluidic chip. Therefore, the tool size should be smaller than the height of the microchip with a thickness of

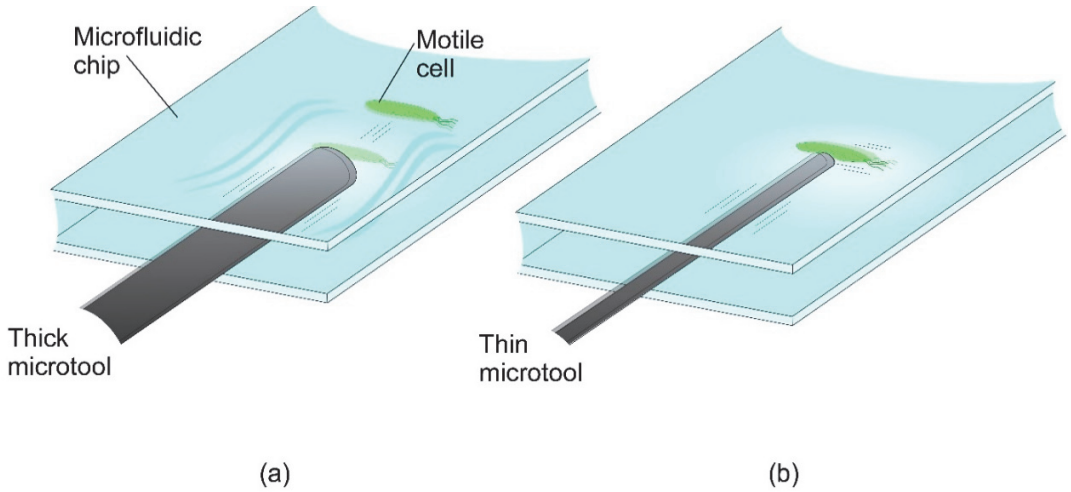

Figure 3.2: Fluidic disturbance problem when stimulating motile cells. (a) Thick microtool. (b) Thin microtool.

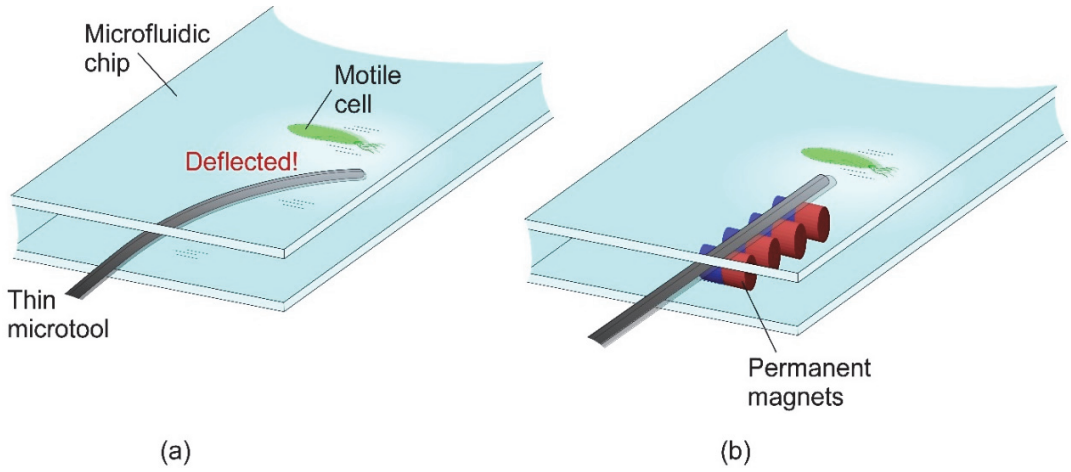

Figure 3.3: Conceptual image of the microtools drive method.

several tens of micrometers. However, as discussed earlier, the microtool would bend easily due to the hydrodynamic drag force exerted while moving the tool in the fluid, as shown in Figure 3.3(a). In order to overcome this problem, the magnetic force was introduced as an opposing force to keep the total force on the tool balanced. To do that, a number of permanent magnets were aligned under the tip of the microtool, as shown in Figure 3.3(b).

To apply stimulation to the target motile microorganism, a microtool is used in a tethered configuration as shown in Figure 3.4. The tool is attached to a xy motorized stage (Physik Instrumente Inc.), driven by a piezo-actuator with a positioning accuracy of 200 nm and drive speed of 400 mm/s, to control the position of the tool by sending commands from the PC. The stage reference position is sent from the PC and the appropriate position command u_r is initiated from the proportional-integral (PI) controller according to the error signal e_r using the

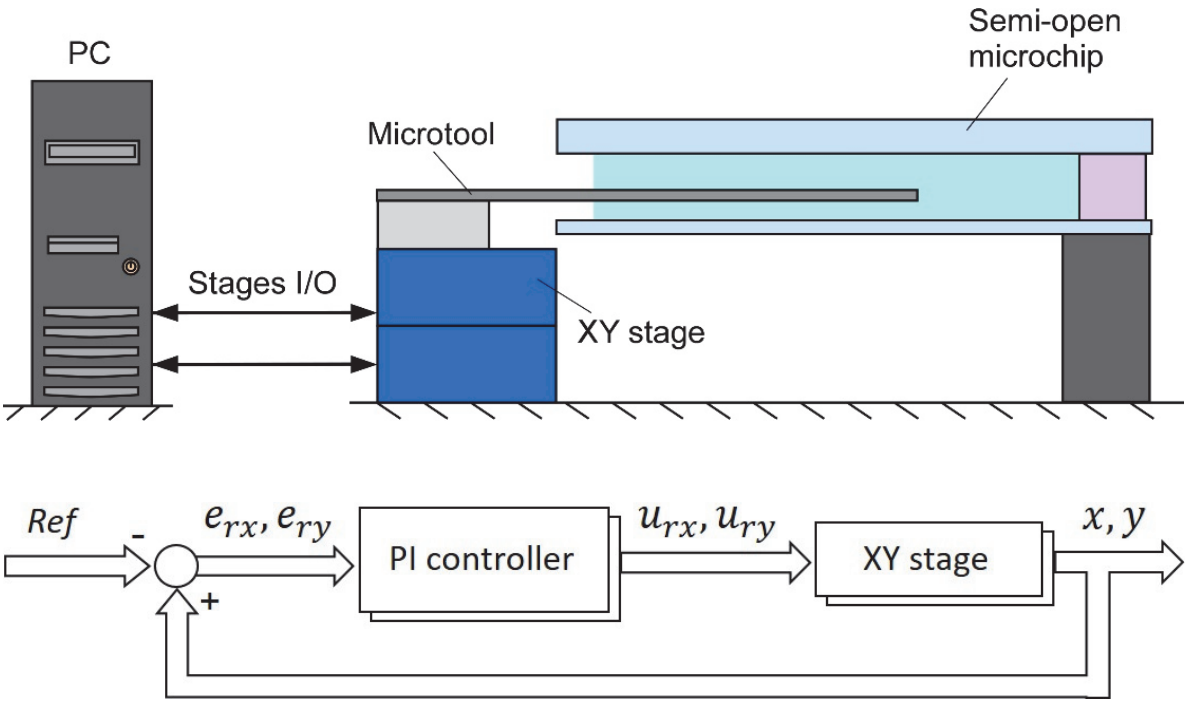

Figure 3.4: Setup of the stimulation system and the control block diagram.

following equation:

$$u_r = K_p e_r + K_i \int e_r \tag{3.1}$$

where K_p, K_i are the proportional gain and the integral gain, respectively. The design of the microchip is changed here from completely closed to a semi-open microchip. An aperture is made on the side of the chip in order to insert the microtool. Thanks to the high water tension at the aperture, no water leakage was observed during the actuation of the tool.

3.2 Modeling of Microtool

Figure 3.5 (a) shows the forces acting on a free microtool supported from one end and immersed in a fluid. In this case, gravity and buoyancy act on the tool and they nearly cancel each other. In fact, gravity depends on the total mass of the tool (the length from the supported end to the unsupported end) and is insignificant in water as long as the tool's length is not extremely long.

When actuating the microtool in the fluid, a hydrodynamic drag force is generated, as shown in Figure 3.5(a). The drag force would cause the tool to deflect opposite to the actuation direction, and the deflection quantity depends on the actuation velocity of the tool. In order to compensate for the tool's deflections, the hydrodynamic drag force should be first estimated. The drag force caused by the motion of a body through a fluid is given by the equation:

$$F_h = \frac{1}{2} C \rho A_{mt} v_{mt}^2 \tag{3.2}$$

where C is the drag coefficient, ρ is the density of the fluid, v_{mt} is the velocity of the body relative to the fluid, and A_{mt} is the cross-sectional area of the body perpendicular to the flow

direction. To estimate the drag force we need to know the drag coefficient, since it differs from one fluid to another, and tends to have larger values in fluids with low Reynolds number which is the case of microfluidics [71]. The drag coefficient is estimated experimentally by calculating the maximum deflection of the microtool when actuated in the fluidic environment. To do that, the tool is modeled as a cantilever beam, as shown in Figure 3.5(b).

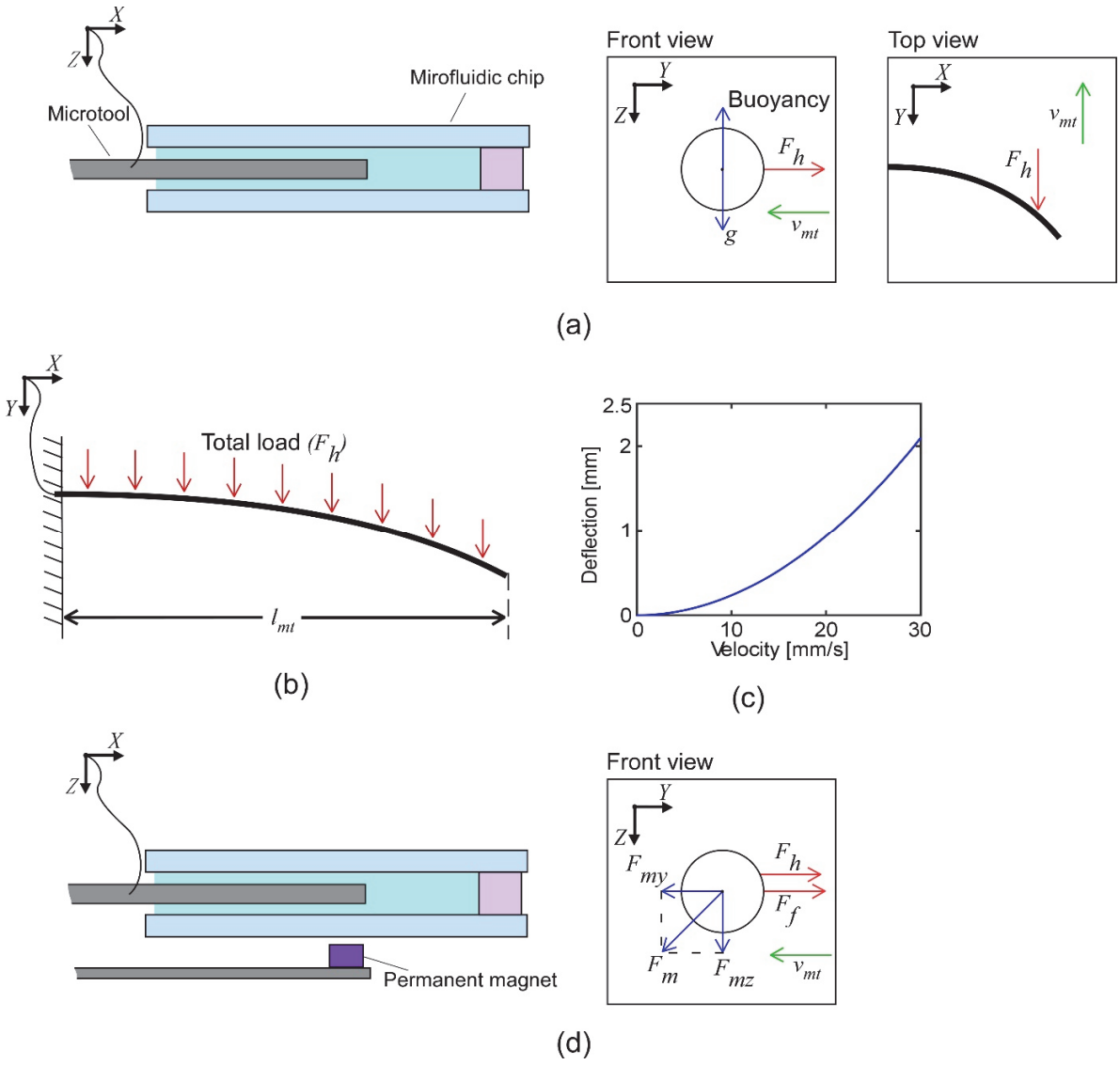

Figure 3.5: Modeling of the microtool.

The maximum bending (deflection at the unsupported end) of the beam is given by the following equation:

$$y_{mt} = \frac{F_h l_{mt}^3}{8EI_{mt}} \tag{3.3}$$

where l_{mt} is the beam length, E is the modulus of elasticity and I_{mt} is the moment of inertia. We consider the hydrodynamic drag F_h to be the total uniform load acting on the beam. By substituting F_h from Equation (3.2) and then solving for C we get the following equation:

$$C = \frac{16 y_{mt} E I_{mt}}{\rho A_{mt} v_{mt}^2 l_{mt}^3} \tag{3.4}$$

The maximum deflection y_{mt} is identified experimentally by actuating the microtool in a microfluidic chip and measuring the maximum deflection at the unsupported end of the microtool. As for the actuation velocity, it was set to the maximum speed that the tracking system can reach since it is considered as the platform's limitation. After confirming the maximum deflection, the drag coefficient can be calculated using Equation (3.4). Consequently, the hydrodynamic drag is calculated from Equation (3.2). The drag at the maximum speed (maximum drag) was confirmed to be in the order of the millinewton. Figure 3.5(c) shows the estimated deflection of the microtool using a rearranged form of Equation (3.4), where: $l_{mt} = 27$ mm, $\rho = 1 \times 10^{-3}$ kg/mm^3, $A_{mt} = 1.35$ mm^2, $I_{mt} = 120.2 \times 10^{-7}$ kg×mm^2, $E = 2 \times 10^5$ N/mm^2, and $C = 3.37 \times 10^{-3}$.

In order to compensate for the deflections of the microtool using permanent magnets, the opposing magnetic force should also be from the same order. The magnetic force generated by the magnets would have both vertical F_{mz} and horizontal F_{my} components, as shown in Figure 3.5(d). F_{mz} would pull the microtool towards the glass of the microchip resulting in a friction

force F_f opposite to the actuation direction. Our interest is the horizontal component F_{my}, which will counteract the hydrodynamic drag F_h and the friction F_f. In order to balance the horizontal forces acting on the microtool the following relation should be true:

$$F_{my} = F_h + F_f \tag{3.5}$$

The hydrodynamic drag force F_h is mainly the result of the tool's movement so it cannot be avoided or reduced unless the shape and dimensions of the tool are changed, which is a laborious task. On the other hand, the friction force F_f is the result of the tool movement against the chip surface, caused by the gravity (can be neglected) and by F_{mz}. Therefore, the friction force can be reduced by reducing F_{mz}.

$$F_f = \mu_s F_{mz} \tag{3.6}$$

where μ_s is the friction coefficient. In fact, increasing F_{my} by increasing the flux density conventionally would also result in increasing F_{mz}, thus increasing the friction force consequently. One of the possible solutions for this problem is to reduce F_f by using a number of permanent magnets with an arrangement that would decrease F_{mz} while enhancing F_{my} at the same time, which would result in better positioning accuracy of the tool. The effect of the magnet arrangement on the positioning accuracy will be further investigated in the experimental section of this chapter.

3.3 Evaluation Experiments

3.3.1 Design and fabrication of microfluidic chip

The microtool will be actuated inside a microfluidic chip to apply stimulation to the target microorganism. Therefore, a semi-open microchip was fabricated with an aperture on one side for the insertion of the tool. The thin nature of the microchip increased the water tension on the side aperture, which prevented water leakages. The microfluidic chip was made of a glass-PDMS-glass sandwich with a chamber size of l_c, w_c, and h_c (length, width, and height). The fabrication process is shown in Figure 3.6 and is described as follows:

First, a 1 mm diameter hole is opened in a No. 5 glass substrate (≈500 μm thick) using an ultrasonic driller to serve as an inlet. Next, Polydimethylsiloxane (PDMS) adhesive sheets

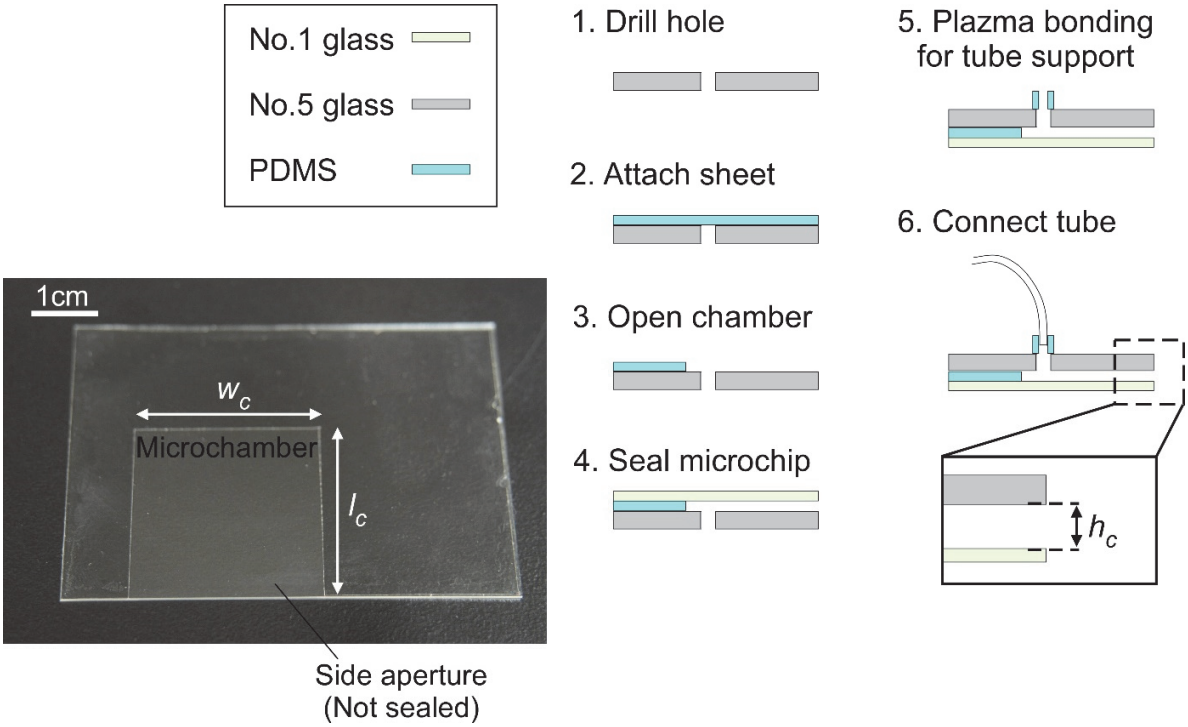

Figure 3.6: Fabrication of microfluidic chip.

(50, and 100 μm thick) were attached to the No.5 glass substrate. The number of attached sheets depended on the required thickness of the chip. After that, a 30 × 30 mm chamber was cut in the PDMS layers in a way that left an aperture on one side of the microchip for the later insertion of a microtool. Next, No.1 glass (120~170 μm thick) was used to seal the microchip. Finally, tube support made of PDMS was bonded to the chip using plasma ponding, and a tube was connected to the inlet of the microchip. Figure 3.6 shows an example of a fabricated chip.

3.3.2 Determination of the microtool size

After determining the thickness of the microchip, the tool size was determined. In the following experiment, two microtools with different diameters were actuated inside a microfluidic chip. Microbeads (diameter: 5 μm) were diluted in sterilized water to be used as a liquid in the microchip. The two microtools were actuated using the same velocity. When actuating a relatively thick microtool (diameter: 1.1 mm), large fluid flows were generated and the position of the microbeads inside the fluid was largely changed, as shown in Figure 3.7(a). In contrast, the microtool with the smaller thickness (diameter: 0.3 mm) generated less flow, where the position change of the microbeads was much lower, as shown in Figure 3.7(b). Therefore, the use of a relatively thin microtool is highly required.

On the other hand, because the stimulation of the swimming microorganism was conducted inside a microfluidic chip, the tool size had to be smaller than the height of the microchip with a thickness of several tens of micrometers. Consequently, a microtool with a diameter of 50 μm was used for the stimulation platform, as shown in Figure 3.8. The microtool was made of ferromagnetic stainless steel (SUS 304), and we can clearly see the bending in the tool caused by gravity alone, which gives some perception of how challenging it is to drive such a tool.

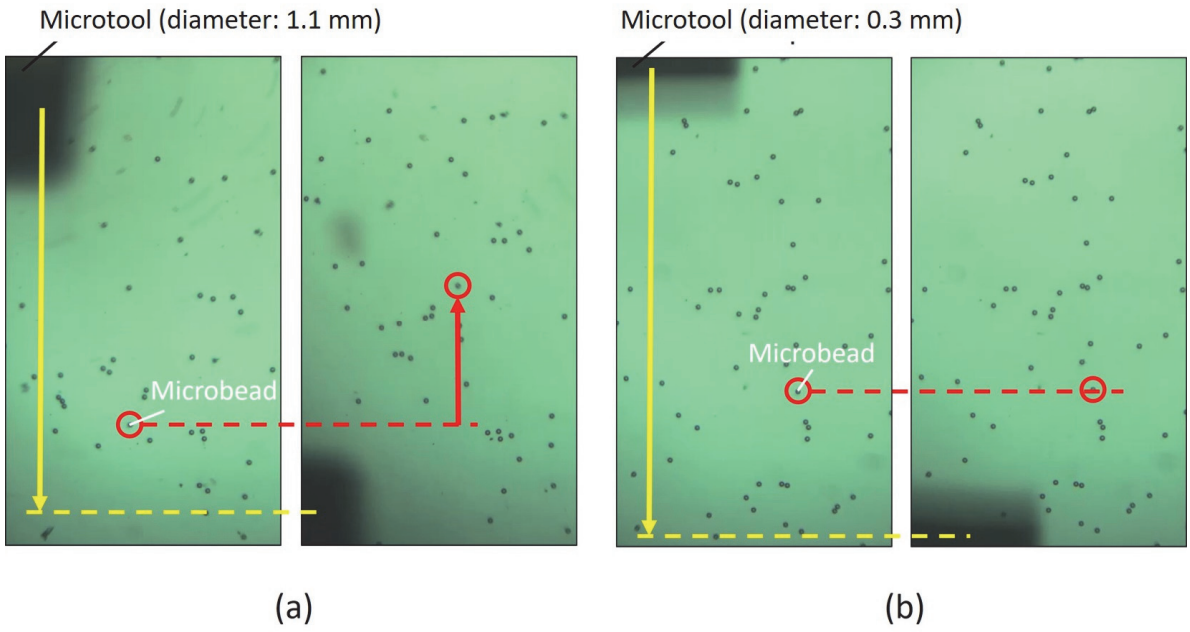

Figure 3.7: The effect of the size of the microtool on the fluidic flow.

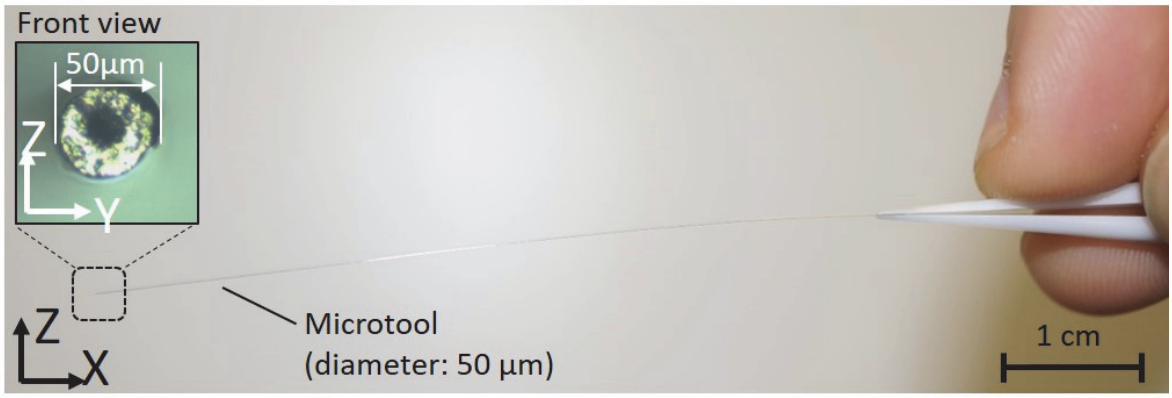

Figure 3.8: An overview of the microtool (tubular structure) with a diameter of 50 µm.

3.3.3 Effect of permanent magnets arrangement

The design of the magnets arrangement in the microtool drive method is very crucial to achieve higher positioning accuracy. As mentioned earlier in Section 3.2, we are interested in the horizontal component of the magnetic force to compensate for the microtool deflection. Therefore, the magnetization axis of the permanent magnets is arranged horizontally with the magnetization axis parallel to the hydrodynamic drag force, which drastically enhances the horizontal component of the magnetic force acting on the microtool [70]. In order to design the magnetic flux and change the resulting force, two or more magnets are used in different arrangements that will allow for the change in the magnetic flux shape, and hence changing the horizontal and vertical components.

Numerical simulation was first used to confirm the effect of the magnets arrangement on the magnetic forces. COMSOL Multiphysics® simulation software was used for the numerical simulation [72]. Two arrangements were used in simulation, as shown in Figure 3.9(a); in the arrangement (1), all the magnets had the same orientation of the magnetization axis, whereas, in the arrangement (2), each magnet had an opposite orientation of the magnetization axis compared to neighboring magnets (alternating polarity). In the simulation, 1.0×1.0 mm cylindrical magnets with a magnetization of 300 kA/m along the height of the cylinder were used. Figure 3.9(b) shows the numerical simulation results for the flux density of each magnets arrangement. In this simulation, eight magnets were used in each arrangement (n_m=8), and the magnetic flux was measured along the x-axis passing on the side of each magnet in the arrangement. It is clear from the figure that arrangement (1) produce a larger flux, where the magnets act as one large magnet, compared to the arrangement (2).

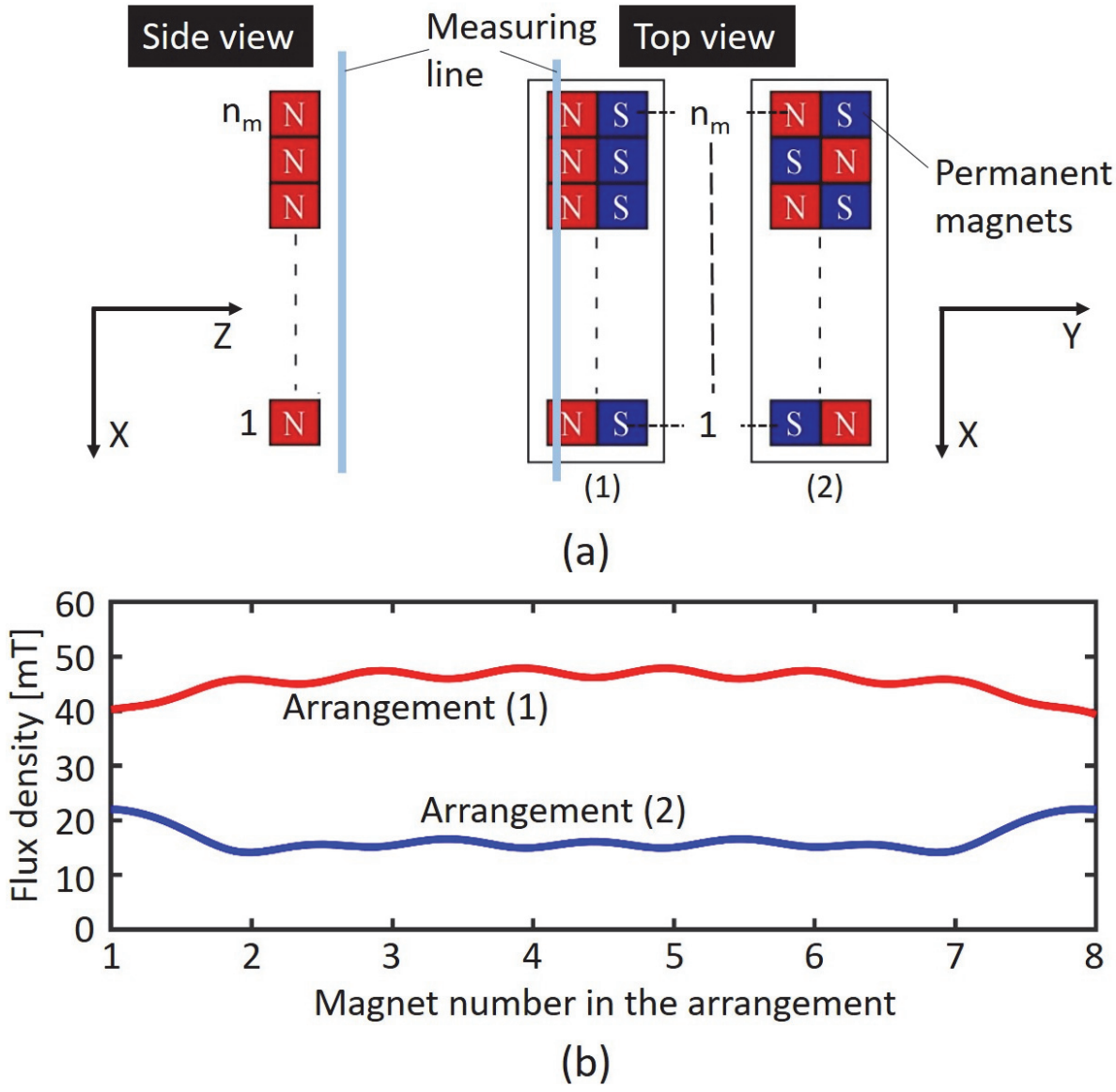

Figure 3.9: Numerical simulation of the magnetic flux generated by two permanent magnets arrangements. (a) Magnets arrangements setup. (b) Flux simulation.

Figure 3.10 shows the numerical simulation of the magnetic force generated by each arrangement, mainly the vertical component (z component) and the horizontal component (y component). The force was measured along the y-axis, as shown in Figure 3.10(a). In arrangement (1), the z component is approximately 6 times larger than the y component along

the y-axis, as shown in Figure 3.10(b). As mentioned in Section 3.2, the z component would pull the microtool towards the glass surface of the microchip and hence the friction force acting on the tool would be drastically increased in this arrangement. On the other hand, in the arrangement (2) the z component stars at a large value and then drops in a parabola shape, whereas the y component forms two peaks, as shown in Figure 3.10(c). The point where the y component reaches its peak value, shown as point F_{yp}, is the point where we have a good driving force on the horizontal axis and a comparatively small force on the vertical axis (less friction force).

The next step is to confirm the validity of the numerical simulation and the performance of each magnets arrangement. In the following experiment, the importance of designing the magnetic flux to achieve higher positioning accuracy was demonstrated. The experimental setup is shown in Figure 3.11(a), a tesla meter (Kanetec inc.) was placed above a group of cylindrical neodymium permanent magnets (diameter: 1.0 mm, height: 1.0 mm) and was separated from the magnets using a 0.12 mm thick glass slide to simulate a microchip. The magnets were aligned inside a jig which is mounted on a manual xy stage. The xy stage was moved to measure the magnetic flux around each individual magnet in the group and the number of magnets inside the jig was changed in each experiment. The magnets arrangements were the same as the arrangements used in the numerical simulation.

Figure 3.11(b) shows the magnetic flux density at one side of each individual magnet in case of eight magnets (n_m= 8) arrangement for both, arrangement (1) and (2). As we can see, the flux shape from the actual measurement is similar to the results of the numerical simulation. In arrangement (1), increasing the number of magnets resulted in a large increment in the magnetic flux at the end sides of the magnets, where the magnets acted as a one large magnet

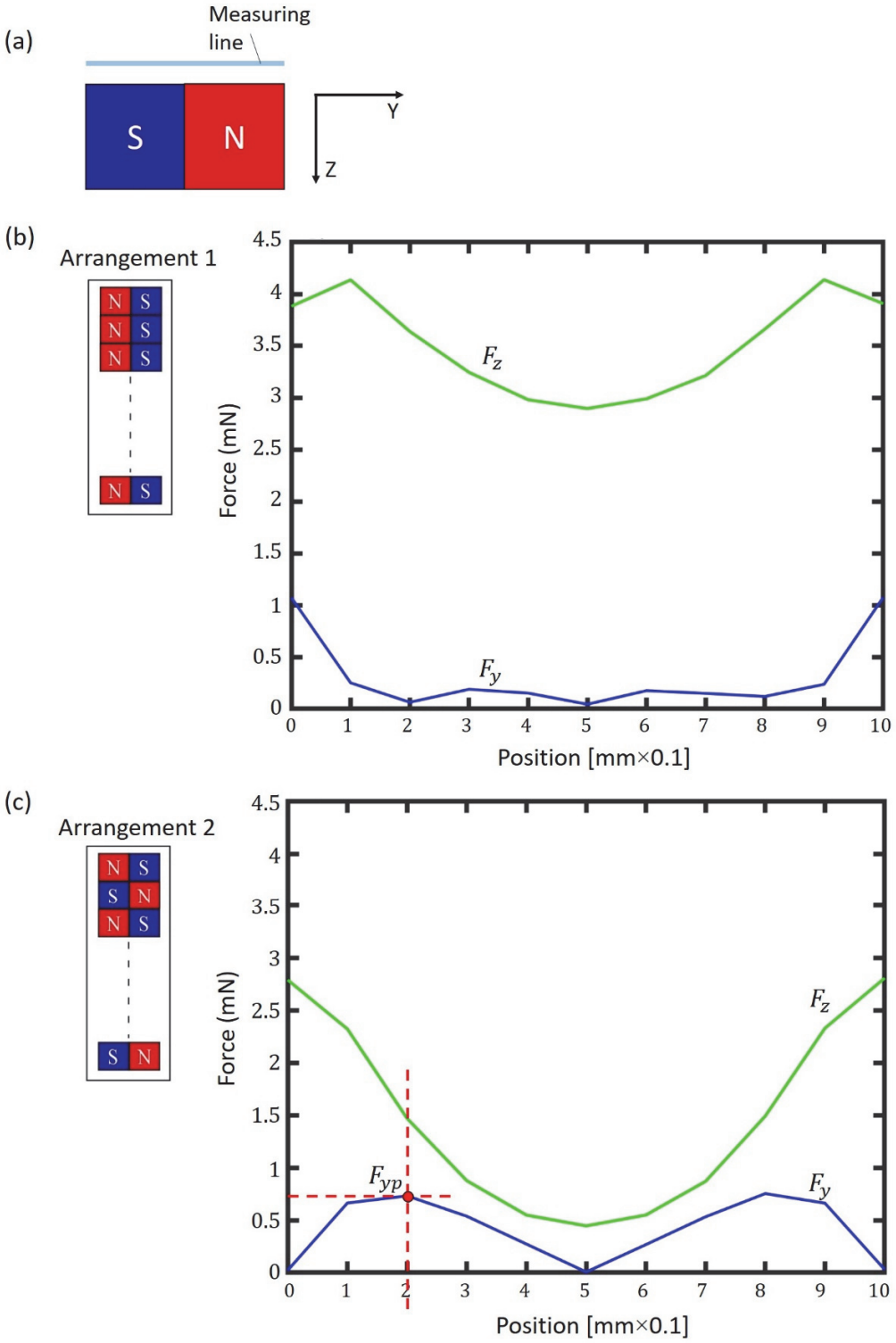

Figure 3.10: Numerical simulation of the magnetic force generated by two permanent magnets arrangements. (a) Simulation setup, (b) Force in arrangement (1), (c) Force in arrangement (1).

with one peak flux appearing around the central magnet of the arrangement. When applying this arrangement to drive the microtool, the microtool was only driven at the end sides of the magnets and the positioning error was drastically increased to approximately 1 mm, even when using relatively low actuation speeds. On the other hand, in the arrangement (2), there was no considerable increment in the magnetic flux when increasing the number of magnets. However,

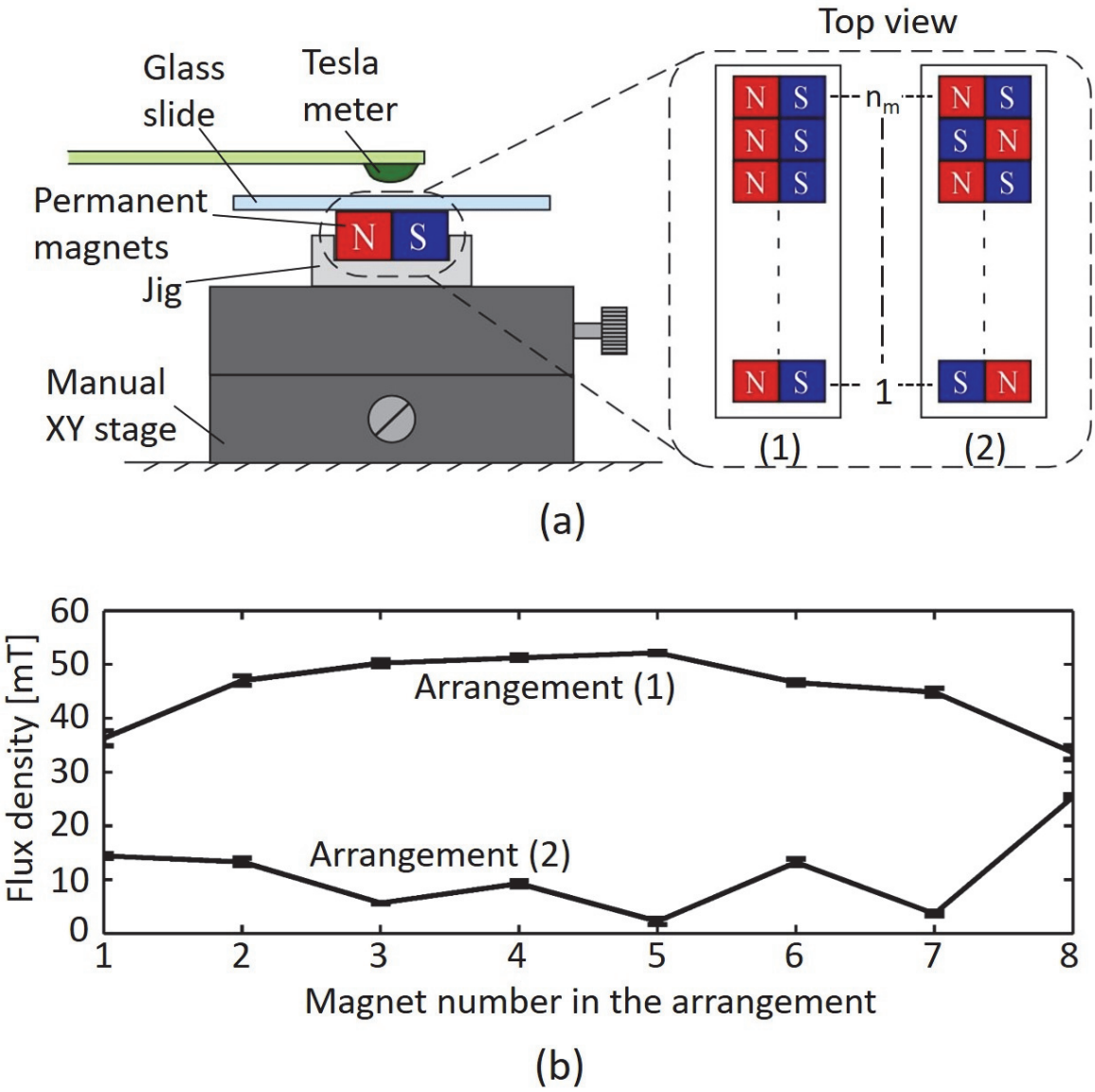

Figure 3.11: Actual measurements of the magnetic flux generated by the two permanent magnets arrangements. (a) Experimental setup, (b) Flux density.

contrary to the arrangement (1), multiple flux peaks were formed along the end sides of the total arrangement. When applying this arrangement to drive the microtool, positioning error was considerably reduced and the maximum error was approximately 200 μm, even when using relatively high actuation speeds, as will be shown in the next section. These results coincide with the simulation results where the point F_{yp} is located at 200 μm from the edge of the magnet. Consequently, we can assume that the shape of the flux around the tool is a more effective factor in regards to the positioning accuracy, compared to the flux density. It is important to note that arrangement (2) is not an optimal arrangement for driving the microtool, and better arrangements are possible. Arrangement (2) will be used in all the following experiments.

3.3.4 Positioning accuracy of the microtool

After determining the arrangement of the permanent magnets, the performance of the microtool actuation method was evaluated. In order to confirm the effectiveness of the driving method, the positioning errors in case of using magnets and without magnets were compared. A number of microtools with different thicknesses, ranging from 50 to 700 μm, were fixed one at a time to the xy stage and inserted from the side aperture in microchips with different thicknesses ranging from 130 μm to 1 mm to suit each of the tools thicknesses.

Each microtool was actuated inside the fluidic environment using multiple speeds ranging from 1~30 mm/s. The hydrodynamic drag force has a minimum effect on the tool's position in the x-direction, i.e. in the direction parallel to the tool's length, due to the small cross-sectional area and the hollow nature of the tool. Therefore, the actuation was only conducted in the y-direction, i.e. in the direction perpendicular to the microtool's length, because the hydrodynamic drag is strongly active in this direction due to the larger cross-sectional area of the tool. The

difference between the tip position of the microtool, measured by a high-speed offline camera (FASTCAM Mini UX100, Photron Inc., Tokyo, Japan) that can capture images of 1280 × 1024 pixels at 4000 FPS, and the position of the actuating xy stage was considered as the positioning error in each frame, as shown in Figure 3.12(a). A total of 25 frames were captured in each experiment and the maximum positioning error was plotted against the microtool's actuation velocity, as shown in Figure 3.12(b) and (c). Figure 3.12(b) shows the deflection caused by the hydrodynamic drag force when no magnets were aligned underneath the microtool. As we can see from the figure, the deflection in the 50 μm thick microtool was considerably large (mm order error) compared to the case of relatively thicker ones (tens to hundreds of micrometers order error). This shows the importance of the tool's stiffness for precise actuation and clarifies the difficulty of precisely actuating a thin tool inside the fluidic environment. On the other hand, as we can see from Figure 3.12(c), which shows the deflection after aligning a number of magnets underneath a 50 μm thick tool, the positioning error is reduced approximately more than ten times. This shows the effectiveness of the proposed driving method and makes it possible to actuate the microtool with higher precision.

It is also relevant to confirm the effect of the microtool's length on the positioning error since the tool's deflection is proportional to its length as shown in Equation (3.3). A longer tool will allow it to reach longer distances and hence the experimental space can be expanded. However, since the magnetic force, which counteracts the drag force, only affects the tip of the tool, and considering that the drag force is acting uniformly on the tool, other sections of the tool can be vulnerable to deflection. Therefore, increasing the microtool's length would increase the total drag force acting on the tool. These deflections along the length of the tool can affect the tip position of the tool, especially in high velocities where the drag force is larger.

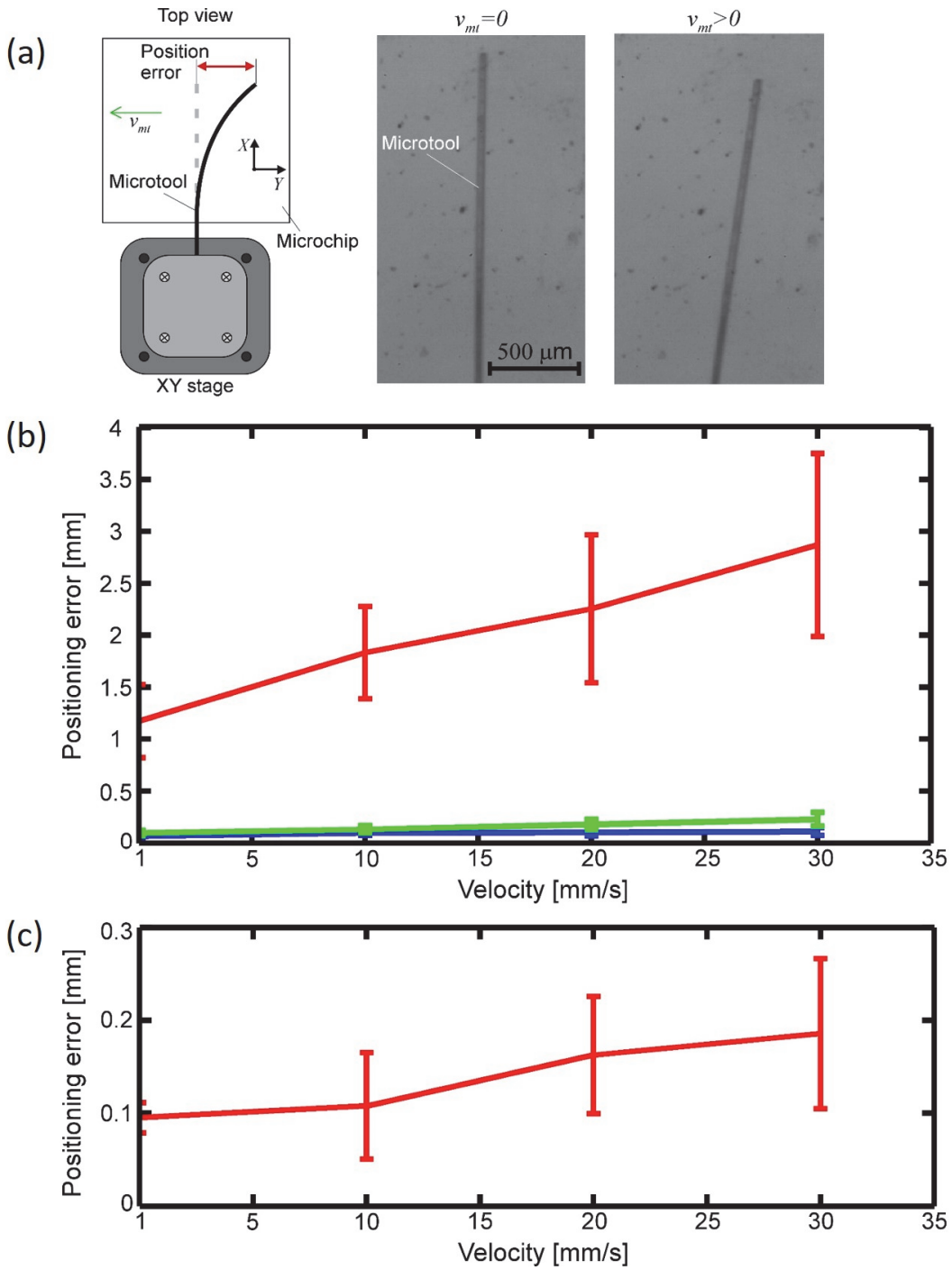

Figure 3.12: Positioning error of the microtool against the actuation speed. (a) Definition of the position error for the microtool actuation. (b) Without magnets for microtools with diameters of 700, 300 and 50 µm (Blue, green and red respectively). (c) With magnets for a microtool with a diameter of 50µm.

The microtool's length effect on the positioning error was confirmed by measuring the deflection for tools with different lengths. In fact, very short tools (1~10mm) showed less deflection compared to longer counterparts. However, the actual deflection increment for longer tools was insignificant and negligible especially within the length and speed range required in our platform, which ranges from 20~40 mm for a maximum speed that reaches 30 mm/s.

3.4 Concluding Remarks

In this chapter, the development of the stimulation platform for single motile microorganism was shown. The performance and accuracy of the platform were confirmed through the basic experiments. The choice of the tool size depending on the amount of generated fluid flow was first discussed. Next, the magnetic drive method for driving thin microtools in the fluidic environment was introduced. The hydrodynamic drag force acting on the very thin tool was significant and the resultant deflection was compensated by utilizing the eight permanent magnets.

To achieve the magnetic drive, permanent magnets' arrangement that reduced the vertical component and enhanced the horizontal component of the magnetic force was first confirmed through numerical simulation and actual experiment on the thin microtool with a diameter of 50 μm. Finally, the positioning accuracy of the stimulation platform was confirmed through the basic experiment and the maximum positioning error of the microtool was approximately 200 μm. The proposed magnetic drive enhanced the accuracy of the microtools more than ten times compared to normal actuation without magnets.

Chapter 4

Application to Actual Motile Microorganisms

In this chapter, the integration of the tracking and stimulation platforms into one final platform will be discussed. The performance and practicality of the final integrated platform will be demonstrated through a number of tracking and stimulation experiments on actual motile microorganisms.

4.1 Integrated Platform

The final step in building the motile microorganism investigation platform is to integrate the observation and stimulation platforms into one functional platform. As explained in Chapters 2 and 3, the two systems have been designed taking in mind the integration step. The main functionalities that allow for the system integration are summarized as follows:

- **Observation:** the noise elimination algorithm designed in section 2.4.3, is the core algorithm in the tracking system that allows for stimulating the target microorganism

without disrupting the tracking control. Otherwise, the stimulation tool would case a tracking failure when entering the ROI of the high-speed online vision.

- **Stimulation:** the low fluidic disturbance generated by the thin microtool is the core technique that allows for integration with the observation platform. By reducing the disturbance, the effect of stimulation on the position of the target microorganism is minimized, and hence the stimulus-response could be observed.

Figure 4.1 shows the final integrated platform and the coordinate system of the platform. As shown in Figure 4.1, the xy stages (stage 2 and 3) that will actuate the microtools are mounted on xy stage 1 to reduce vibration effects caused by long jig arms. Consequently, stages 2, and 3 should be actuated to keep track of the target at all times. To achieve that, the controller reverses the command sent to stage 1 (D_x, D_y) from Equation (2.7), and sends it to drive stages 2, and 3 as follows:

$$\begin{bmatrix} D_{2x} \\ D_{2y} \end{bmatrix} = \begin{bmatrix} D_{3x} \\ D_{3y} \end{bmatrix} = - \begin{bmatrix} D_x \\ D_y \end{bmatrix} \tag{4.1}$$

where, $D_{2x}, D_{2y}, D_{3x}, D_{3y}$, are x and y distance commands for stages 2 and 3, respectively.

Figure 4.2 shows the software architecture of the platform. The main PC (control PC), executes two control program concurrently in real-time. The first program is responsible for image grabbing from the high-speed online vision, image processing, motorized stages control, and data logging. The second program is responsible for controlling the focal distance through z-direction control, and for controlling the light source intensity. The second program also communicates with the first program to send the information for the pixel pitch in order to achieve target tracking in different magnification ratios. A second PC (video recording PC)

equipped with large disk space, is used to record high-resolution images and videos of the CCD camera that is fed through an image splitter.

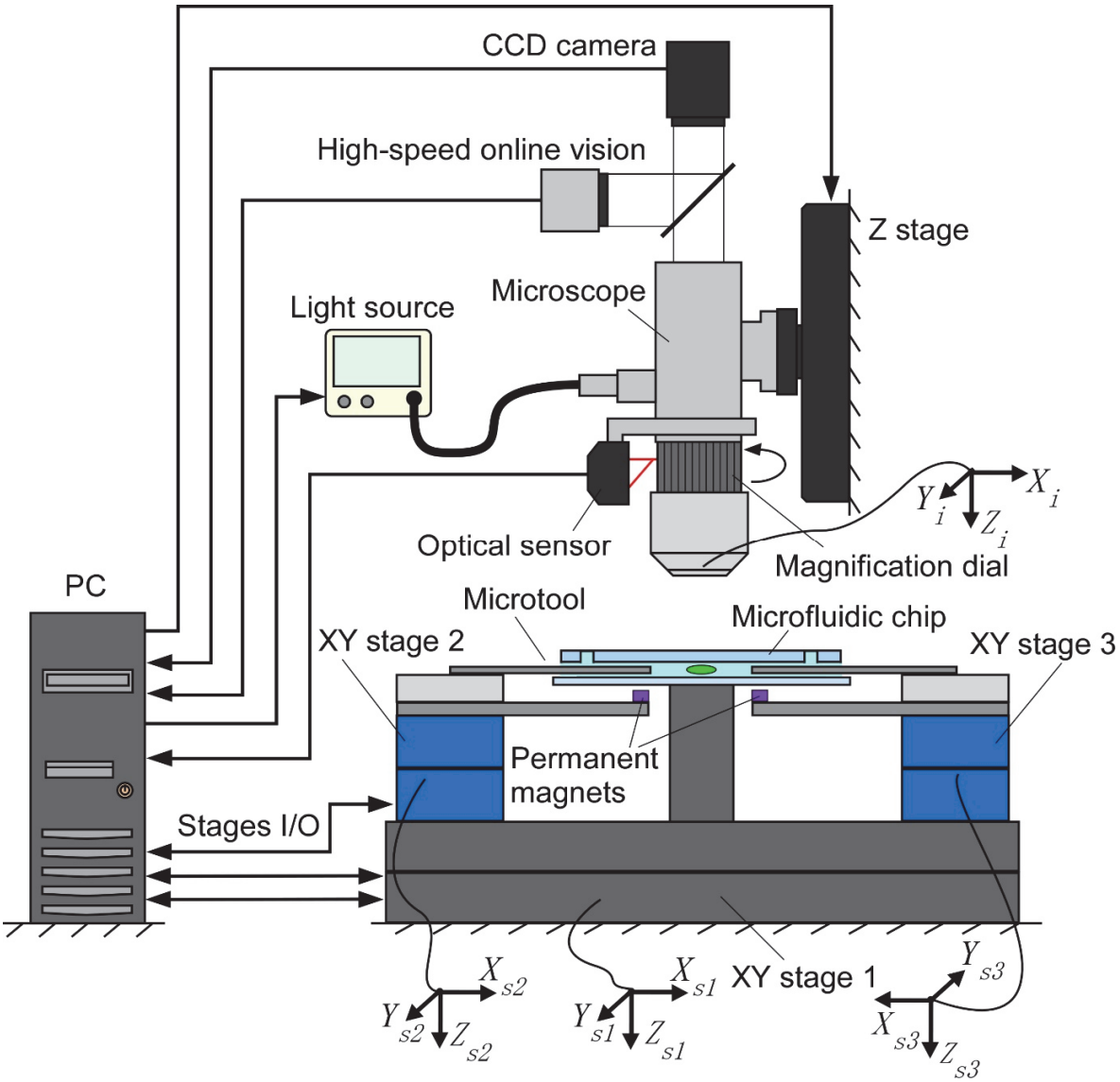

Figure 4.1: Final integrated platform.

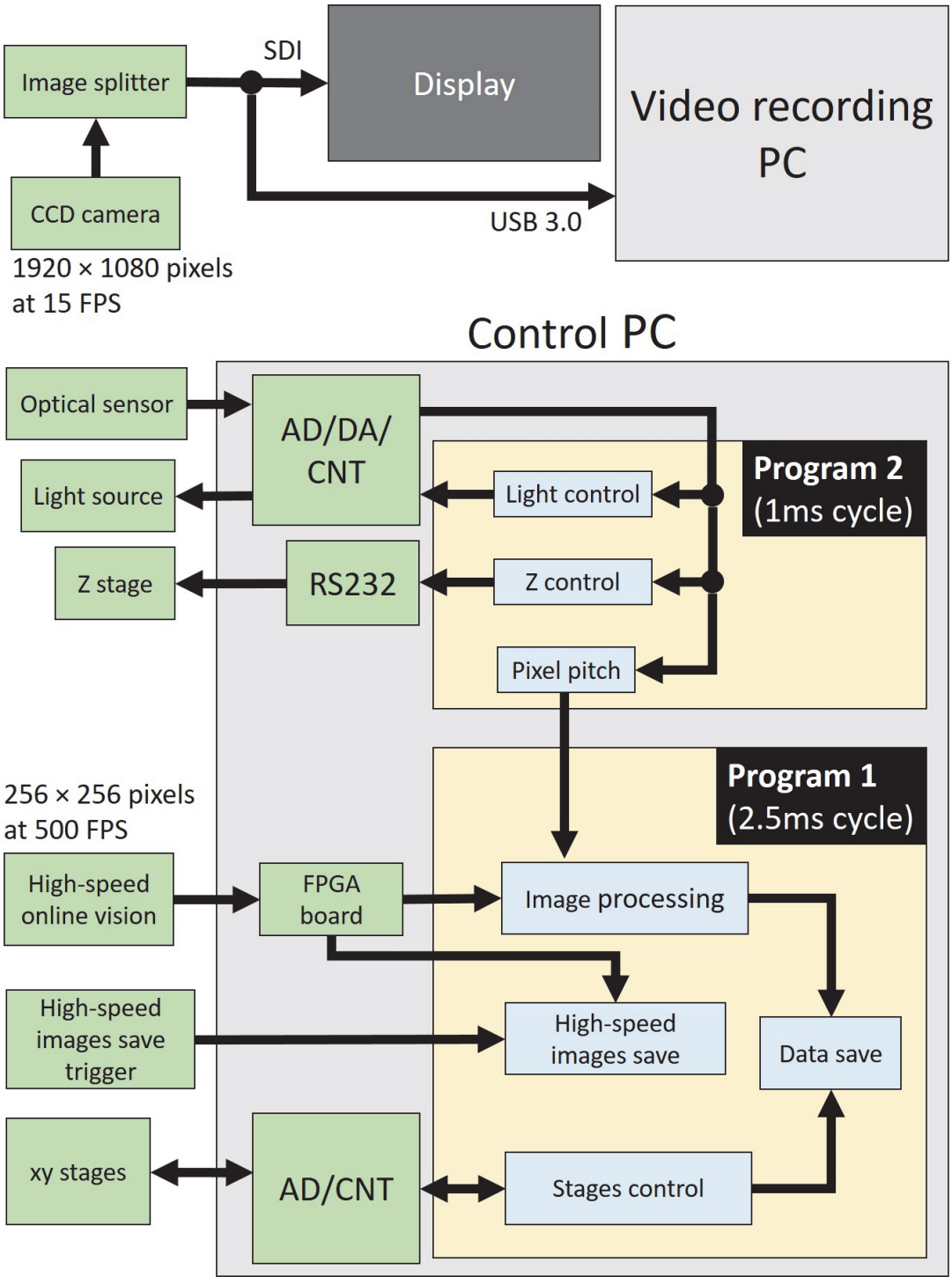

Figure 4.2: Software architecture of the integrated platform.

4.2 The *Paramecium*

The *Paramecium* was chosen as a target microorganism. *Paramecium* is a model organism and is one of the most studied motile cells because of its characteristics such as a large number of cilia [73]–[75]. The *Paramecium* is a unicellular microorganism that belongs to the ciliated group, it can be found in freshwater like small ponds. As shown in Figure 4.3, the *Paramecium* has an ovoid and elongated body shape with a body length of 100–200 μm [76]. As well known, *Paramecia* basically propel themselves by whiplash movements of 10 μm long cilia (Figure 4.4 (a)), which give it a moving speed of approximately 1 mm/s. However, the *Paramecium* speed can reach up to 10 mm/s if it is stimulated; this is due to another actuator called the trichocyst, as shown in Figure 4.4 (b). The trichocyst are thin and long threads that are discharged (ejection speed is within 80 ms) from inside the body for a quick escape when the cell feels stimulation or danger [77]–[80]. The undischarged trichocysts inside the *Paramecium* body are approximately 3–4 μm in length, and they elongate by 6–8 times when discharged [80]. This behavior is remarkable, where one cell exhibits two actuators producing two different gaits. Erxleben et al. have studied the change in potential in the *Paramecium* membrane and its effect on trichocyst discharge through local chemical stimulation [79]. Hamel et al. succeeded in observing the trichocyst reaction by stimulating the *Paramecium* with local heat stimulation using a focused laser beam [78]. Although they found several new gaits of the *Paramecium* by the trichocysts, the specific dynamic behavior of swimming *Paramecium* is still unknown.

For the experiments in this chapter, wild-type *Paramecia* (*P. aurelia*) were prepared and cultivated in a culture medium with an incubator at 25 °C. The medium was made by diluting

50 µl of soymilk inside 50 ml of sterilized water, 12 ml of the mixture were then inserted in a culturing flask and 1 ml of *Paramecia* was finally added.

Figure 4.3: *Paramecium* image.

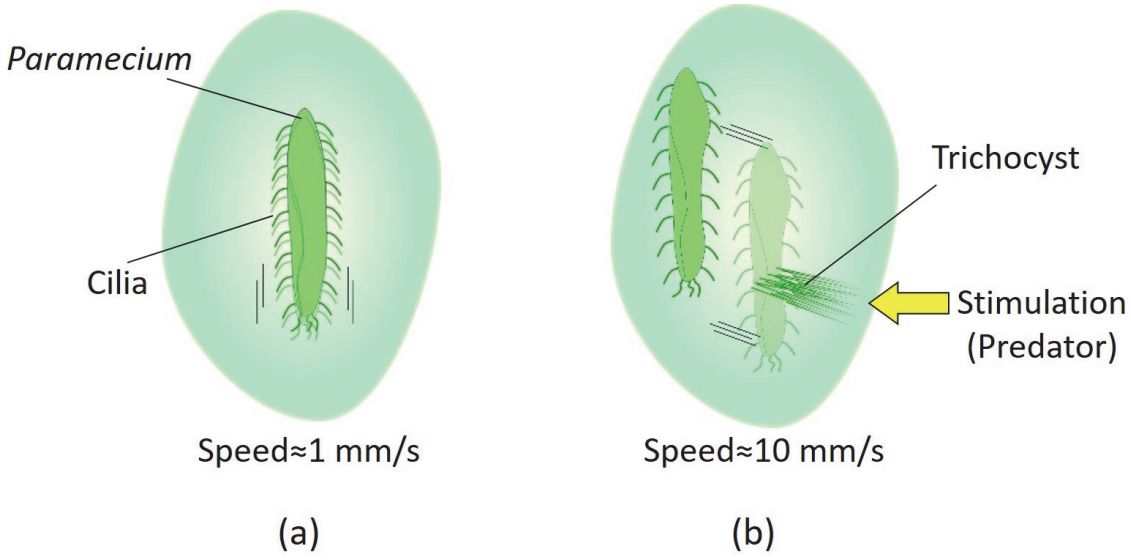

Figure 4.4: Single *Paramecium* equipped with two different actuators.

4.3 Determining the Thickness of Microchip

One of the main motivations to use a microfluidic chip is to eliminate the occlusion between cells, without affecting their swimming mode as much as possible. This could be achieved by choosing the appropriate thickness of the chip (h_c). Therefore, microfluidic chips with a workspace thickness of 50, 100, 150, and 200 μm each were fabricated. A small number of *Paramecia* were then introduced from the inlet of the chip, and the behavior of the *Paramecia* was observed by the microscope. In the case of the 50-μm chip, as shown in Figure 4.5(a), the *Paramecium* frequently touched the upper and/or lower glass substrate, and the swimming mode was slowed down. On the other hand, the overlap of *Paramecia* occurred by a thick workspace with 150 and 200 μm, as shown in Figure 4.5(b). Therefore, in the following experiments, a microchip with a thickness of 100 μm was used, as shown in Figure 4.5(c). The microchip had no occlusion problem and did not have any noticeable effect on the *Paramecium* swimming mode.

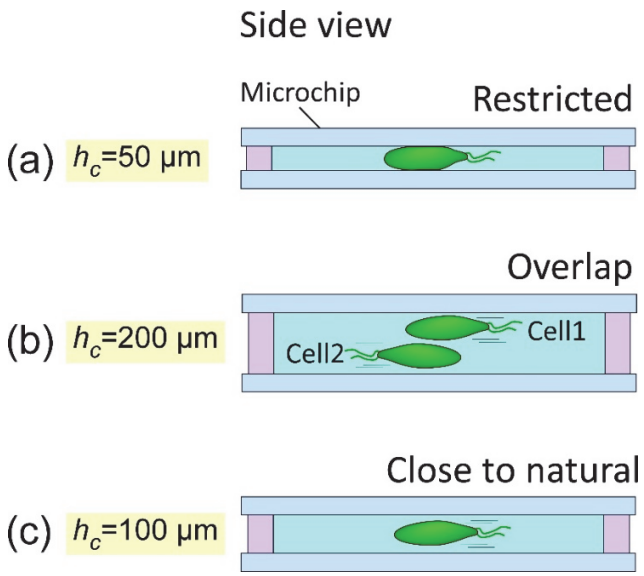

Figure 4.5: Determining the microchip thickness.

4.4 Long-time Tracking

In Chapter 2, it was confirmed from the basic experiment on the tracking system that the speed limitation is up to more than 10 mm/s. Therefore, the *Paramecium* maximum speed is within the limitation of the tracking system. The tracking experiment was done inside a microchip, where a small number of *Paramecia* were introduced. The platform started by searching for a target single *Paramecium* using the lowest magnification ratio available in the platform, to quickly find the target. After a target was located, tracking started at the lowest magnification ratio and was then increased gradually.

Figure 4.6(1–3) shows the searching, tracking, and magnification procedures in the experiment. By considering the shape and size of the *Paramecium*, an elliptical ROI (a = 100 pixel, b = 20 pixels in Equation (2.12)) with 840× maximum magnification ratio was used for all experiments. The tracking was successfully conducted for more than 30 min regardless of image noises, such as microchip edge, debris, and other cells, as shown in Figure 4.6(4–8). Figure 4.7 shows the experimental data and we can clearly confirm that the target is maintained around the center of the FOV for the whole tracking experiment. A total of four experiments were conducted for different *Paramecium*, and the average tracking time was approximately 35 min. Figures 4.8–4.11 show examples of *Paramecium's* swimming path during the tracking experiments. The maximum swimming speed of the *Paramecia* was approximately 2 mm/s in all the experiments. The *Paramecium* position information was taken from the xy stage encoders and the online vision data, where the mean value of the xy stage positioning error (the mean difference between the reference position and the actual positon taken from the stage encoders)

was approximately 40 µm. From these experiments, the effectiveness of the combined magnification control and visual tracking for efficient and long-time tracking was confirmed.

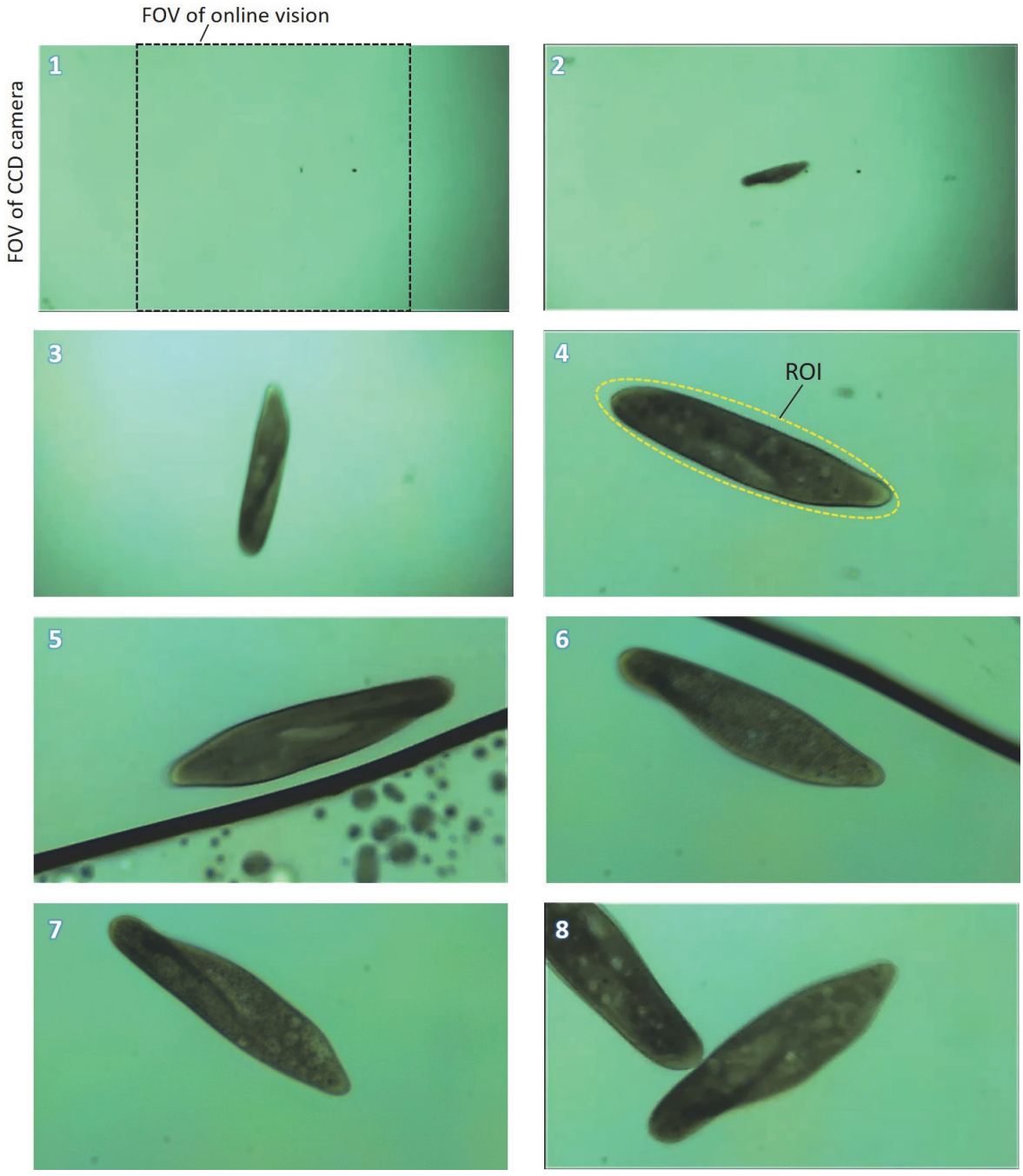

Figure 4.6: Results of long-time tracking of single *Paramecium* in a microfluidic chip. (Experiment no. 1)

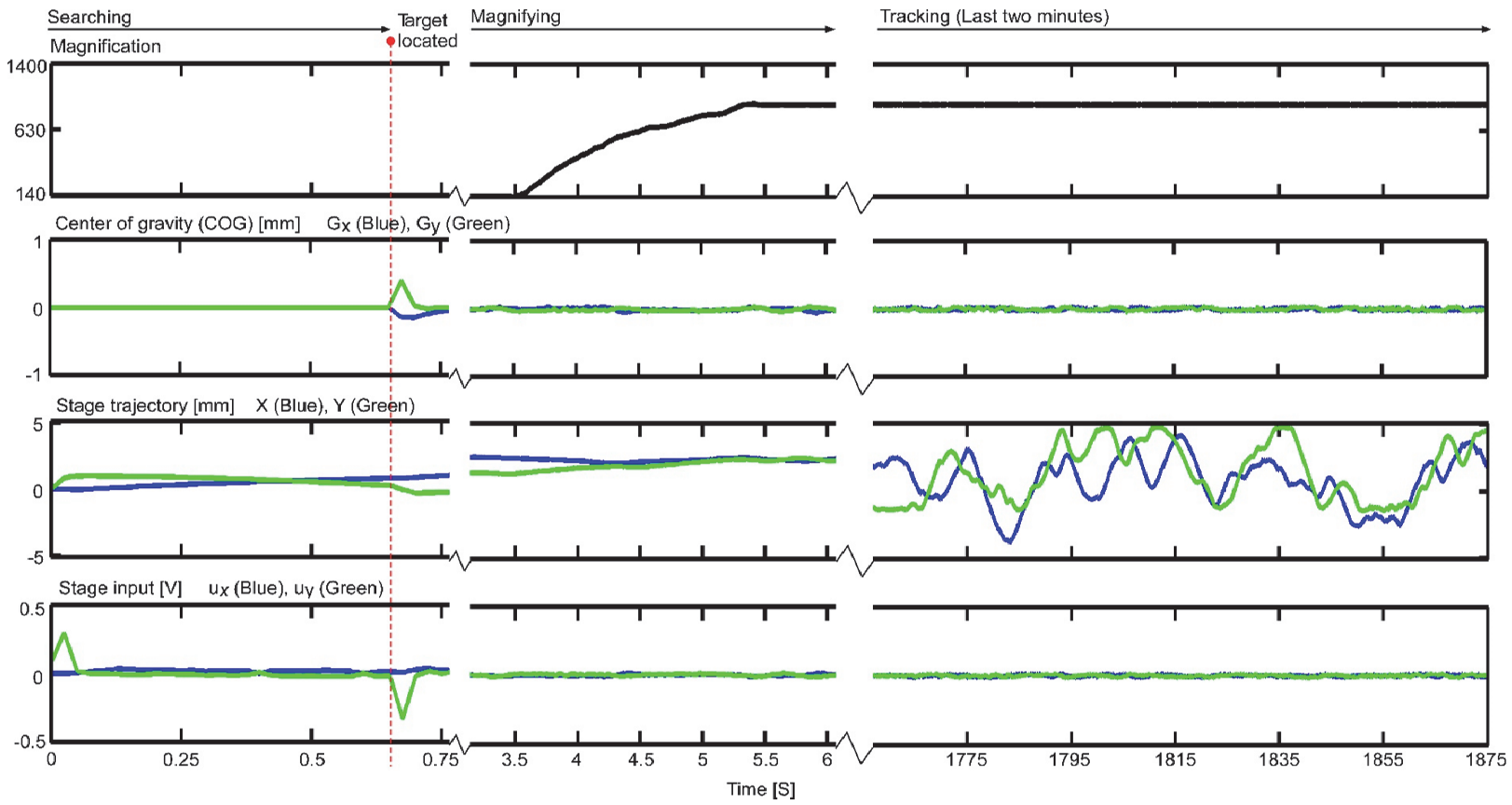

Figure 4.7: Data log measured by the developed platform during the target tracking experiment no. 1. (data sampling cycle was 10 ms)

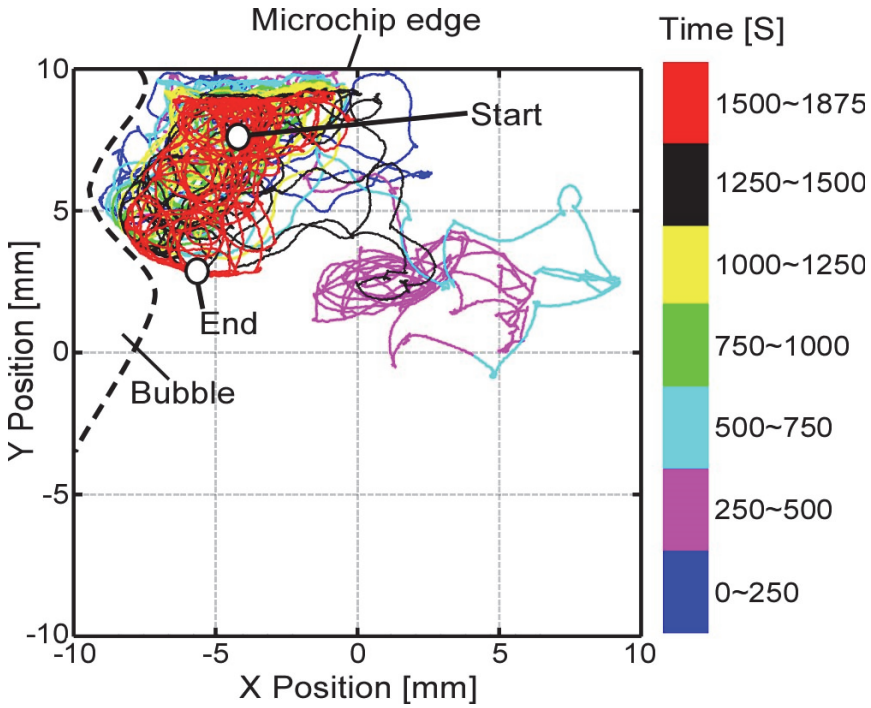

Figure 4.8: Swimming path of single *Paramecium* during 31 min and 15 s of target tracking. (Experiment no. 1)

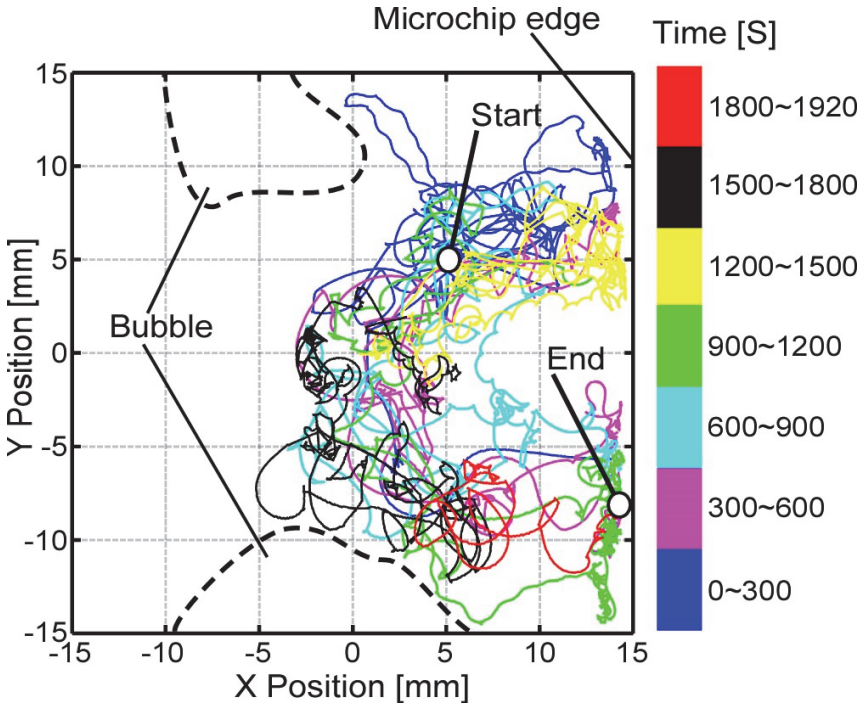

Figure 4.9: Swimming path of single *Paramecium* during 32 min and 9 s of target tracking. Maximum swimming speed of the *Paramecium* was approximately 2 mm/s. (Experiment no. 2)

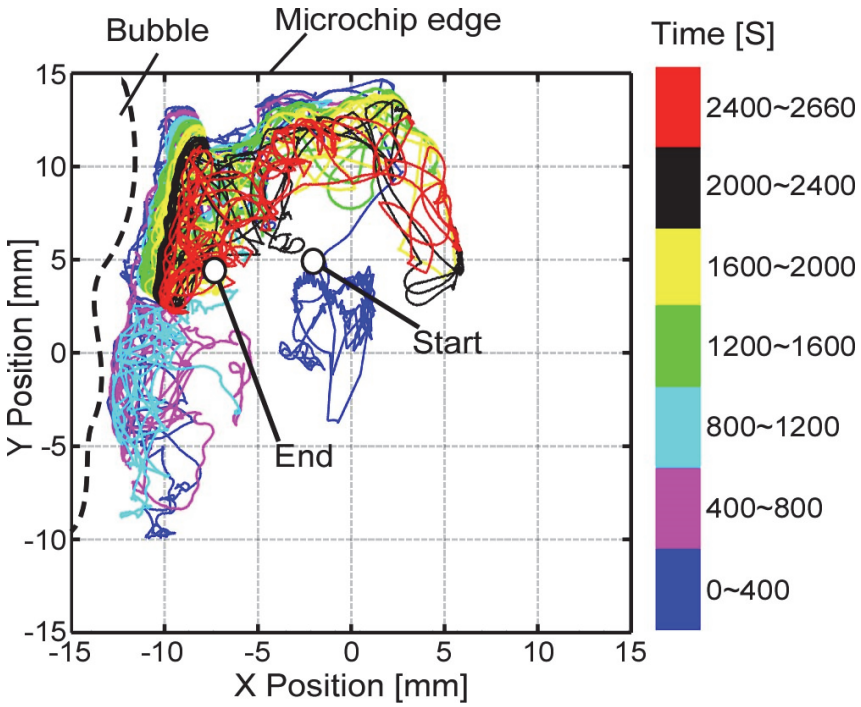

Figure 4.10: Swimming path of single *Paramecium* during 44 min and 32 s of target tracking. Maximum swimming speed of the *Paramecium* was approximately 2 mm/s. (Experiment no. 3)

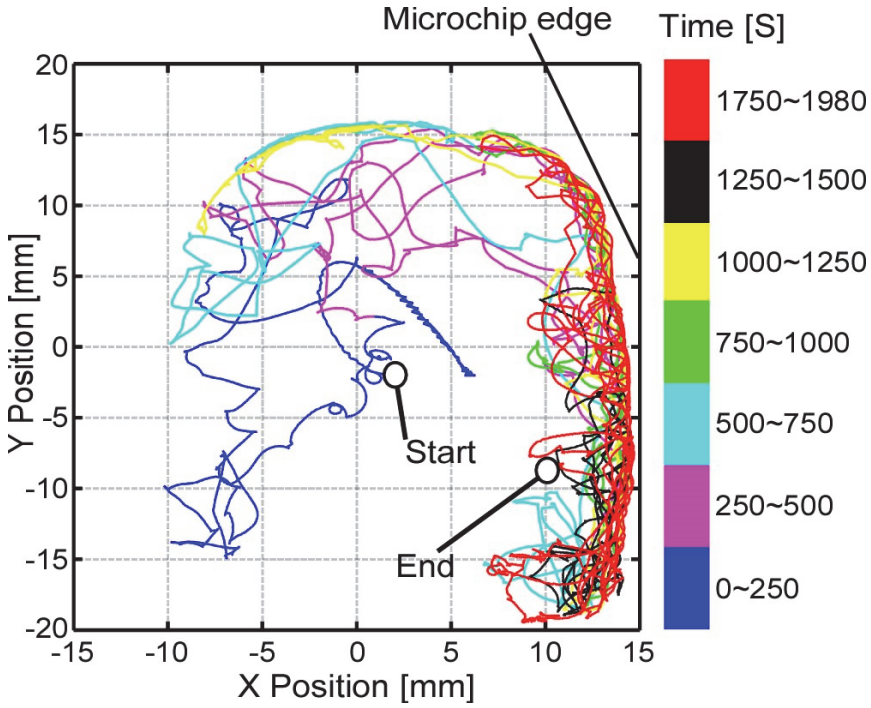

Figure 4.11: Swimming path of single *Paramecium* during 33 min and 15 s of target tracking. Maximum swimming speed of the *Paramecium* was approximately 2 mm/s. (Experiment no. 4)

4.5 Stimulation

Stimulation to a single *Paramecium* inside a microchip using microtools was done to demonstrate the performance of the developed platform. For stimulation, the microchip design had to be modified to insert the tools from the sides of the chip. The microtools were inserted from side apertures that were made on the sides of the chip with no water leakage thanks to the high surface tension. The microtools were driven using the method described in Chapter 3. Two types of stimulation experiments were conducted; mechanical and electrical stimulations.

4.5.1 Mechanical stimulation

The mechanical stimulation of a single cell is strongly required to determine the cell functions and mechanical properties. For example, this type of stimulation can reveal the mechanoreceptors properties and how the cell reacts to external mechanical stimuli [81][82].

Figure 4.12 shows the results for mechanical stimulation on a freely swimming *Paramecium*. In this experiment, only one microtool was used to apply stimulation. The system started by searching for a random target cell as shown in Figure 4.12(a-1). The located cell was maintained in the center of the FOV by utilizing the tracking system as shown in Figure 4.12(a-2 to a-3). While tracking, the microtool automatically followed the movement of the cell using the reference input obtained from Equation (4.1). Consequently, the stimulation was applied by adding additional value to the reference input of the x-axis using a joystick as shown in Figure 4.12(a-4 to a-6). The slow-motion images during the stimulation procedure were recorded at 200 fps with a spatial resolution of 1.66 μm/pixel as shown in Figure 4.12(b-1 to b-3). Figure 4.13 shows the trajectory of the cell.

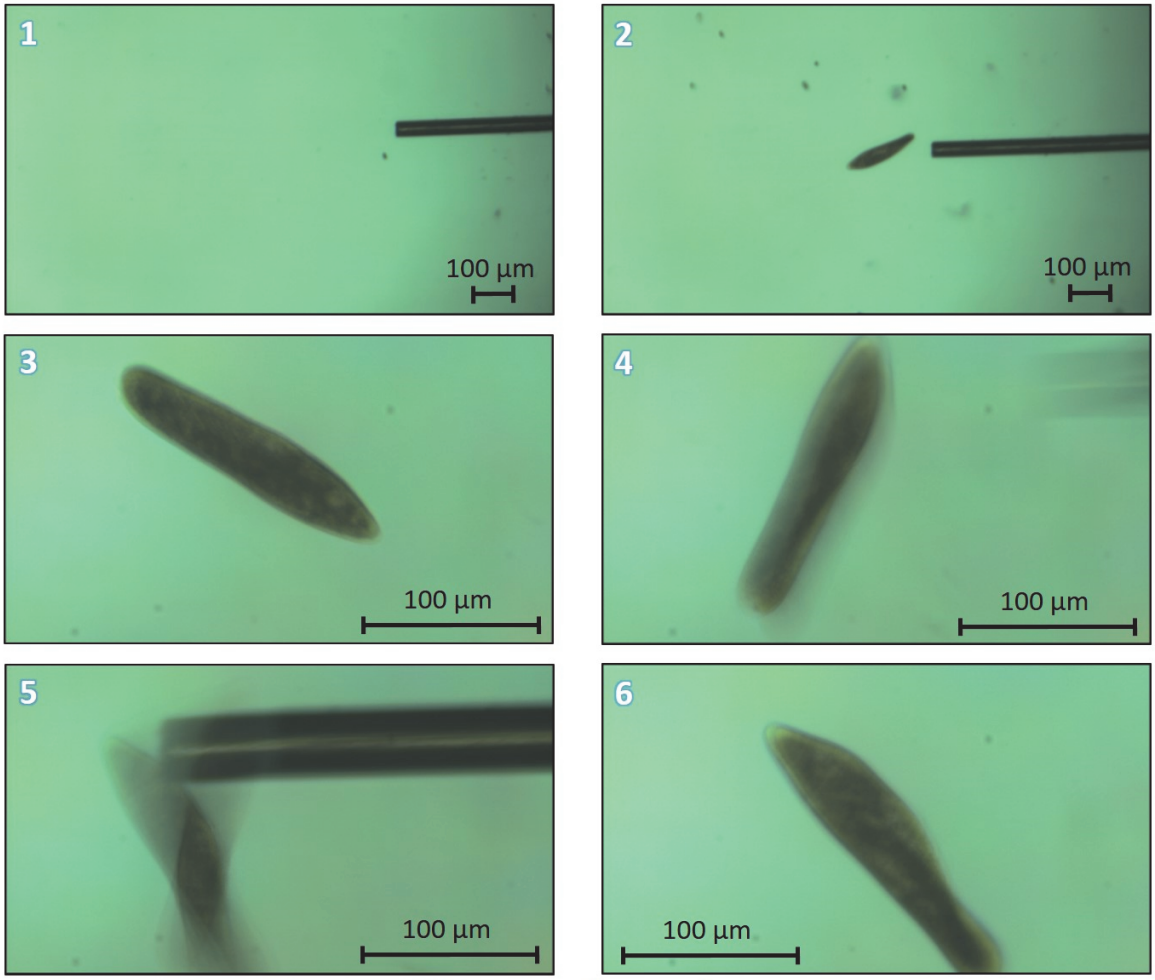

Figure 4.12: Mechanical stimulation of a single freely swimming *Paramecium*.

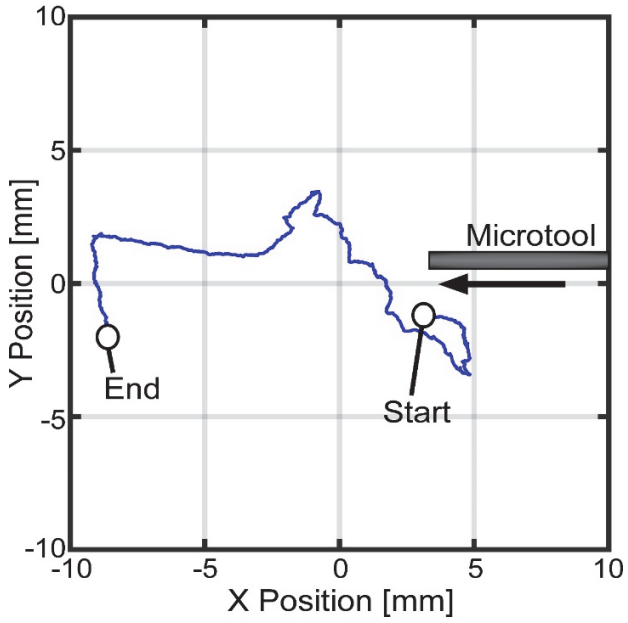

Figure 4.13: Swimming path of single *Paramecium* during mechanical stimulation.

In the experiments, the mean velocity of the target *Paramecium* was approximately 2 mm/s, and the maximum positioning error of the microtool on the y-axis was approximately 200 µm. Although the stimulation experiment was conducted successfully and the hit of the *Paramecium* by the microtool was confirmed, the trichocyst reaction could not be observed, where only the escaping behavior of the cell was confirmed. In fact, the pressure applied by the stimulation and the size of the area of stimulation might have an important role in order to initiate the trichocyst behavior. Therefore, the design and attachment of a needle-like tip to the stimulation tool will be conducted in future work.

On the other hand, the positioning accuracy of the microtool and the vertical position of the target cell played an important role in the success ratio of stimulation. The positioning error of the microtool (approximately 200 µm) caused some unsuccessful stimulation attempts, where the tool thrust behind or in front of the target cell. Moreover, some of the smaller cells were

able to swim more freely in the vertical direction, which also reduced the success ratio as the tool thrust below or above the target cell. However, thanks to the high robustness of the tracking system, the stimulation process could be attempted many times in one experiment until a successful stimulation is achieved. In fact, almost 70% of the conducted stimulation experiments had at least one successful stimulation attempt.

One of the reactions to mechanical stimulation of the *Paramecium* is called the 'avoiding reaction' [82]. This reaction occurs when the anterior side of the cell is mechanically stimulated and it helps the *Paramecium* to avoid obstacles. The reaction can be divided into three main phases as shown in Figure 4.14, these phases are: 1) backward movement, 2) change in direction (orientation), before finally 3) proceeding in a forward movement. Although the avoiding reaction could be observed in previous works, it was not possible to quantitatively evaluate this behavior due to immobilization or area confinement.

Using the developed platform, the first two phases of the avoiding reaction were quantitatively analyzed using the slow-motion images captured by the high-speed vision at the stimulation moment.

1) **Backward movement:** the first phase starts when the stimulation process is completed. To evaluate the effect of the mechanical stimulation, two parameters were confirmed, the velocity of the stimulation tool at the moment of stimulation (v_t) and the distance that the cell moves backward after the stimulation (d_p). These two parameters would show the relationship between the response of the *Paramecium* and the velocity of the stimulation tool. The backward movement distance (d_p) was defined as the distance between the center of the cell immediately after the stimulation and the center of the cell after the backward movement is completed (before

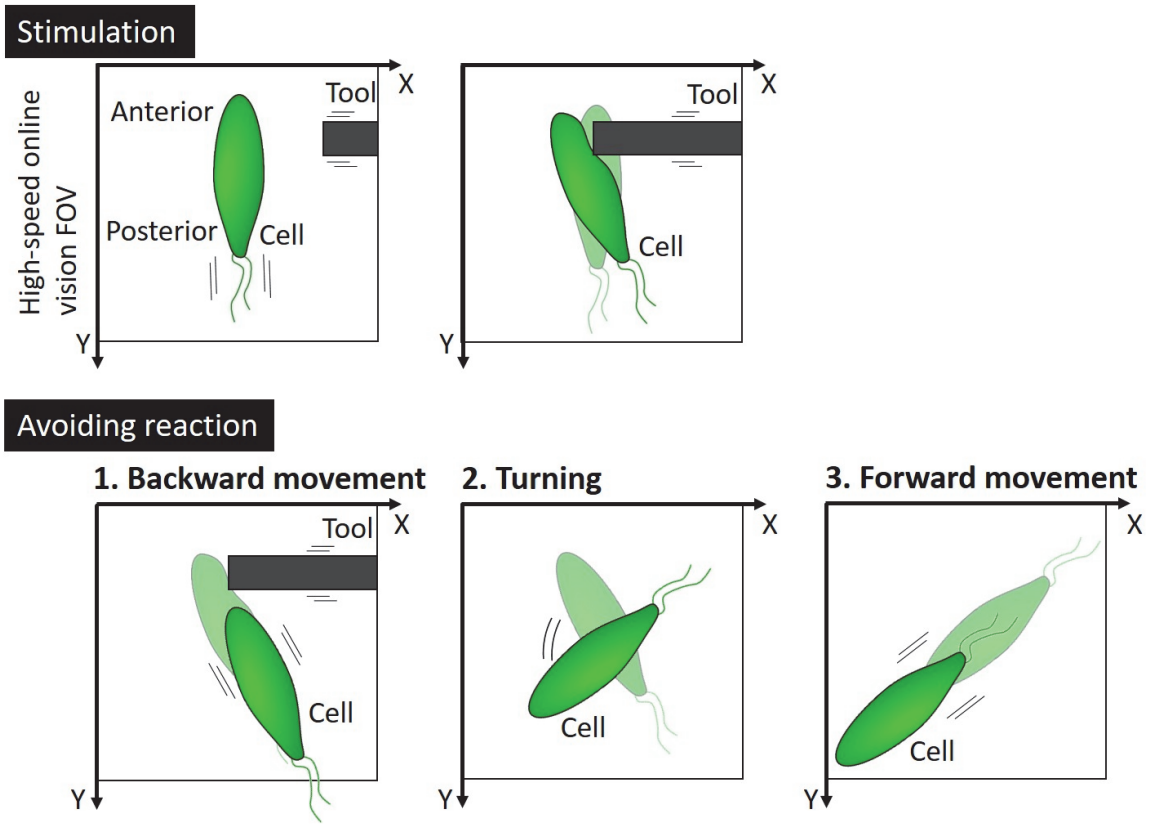

Figure 4.14: The *Paramecium* avoiding reaction to mechanical stimulation.

the start of phase 2 as shown in Figure 4.15(a). Figure 4.15(b) shows the experimental results for two experiments with two different stimulation speeds, 4 mm/s and 40 mm/s. As can be seen from the figure, d_p approximately increases five times when the velocity of the stimulation tool is increased. In fact, the results indicate that there is a correlation between the backward movement distance and the velocity of the stimulation tool. Therefore, nine stimulation experiments (n=9) were conducted to investigate the correlation between the two parameters as shown in Figure 4.16. From the figure, the correlation can be clearly observed where lower velocities of the stimulation tool initiate less backward movements of the cell, and vise versa. The Pearson correlation coefficient (R_{tp}), was confirmed using the following equation:

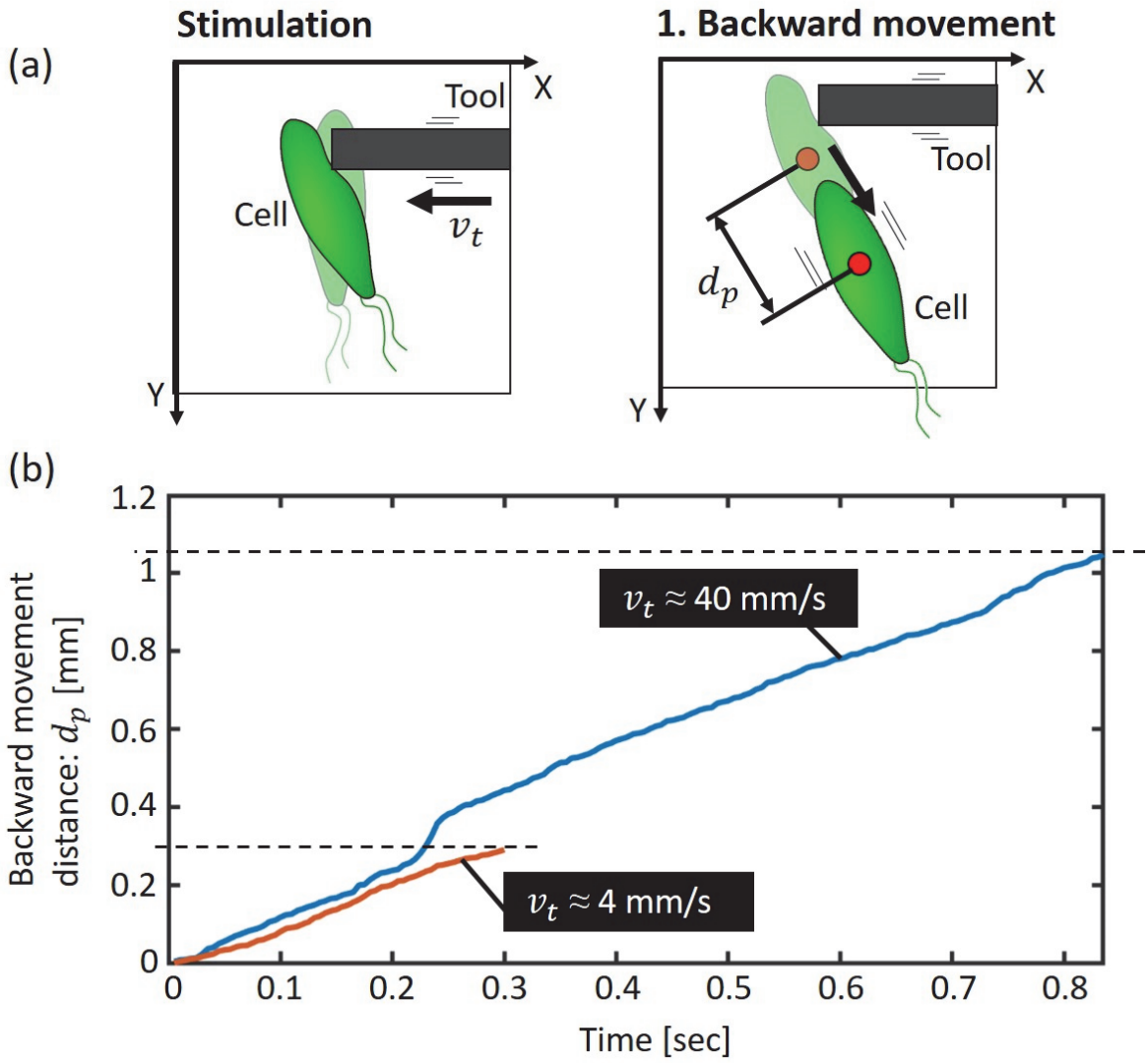

Figure 4.15: The backward movement of the *Paramecium* in response to different mechanical stimulation velocities.

$$R_{tp} = \frac{1}{n-1}\sum_{i=1}^{n}\left(\frac{t_i - \mu_t}{\sigma_t}\right)\left(\frac{p_i - \mu_p}{\sigma_p}\right) \tag{4.2}$$

where t_i and p_i are the values of the stimulation tool velocity and the backward movement distance for the i^{th} experiment respectively, μ_t and σ_t are the mean and standard deviation of the stimulation tool velocity respectively, and μ_p and σ_p are the mean and standard deviation of

the backward movement distance respectively. The coefficient showed a large correlation with the value of $R_{tp} = 0.9$, which clearly shows the effect of the increased velocity of the stimulation tool on the reaction of the *Paramecium*. It is important to note that the higher stimulation velocities are uncommon in the natural environment of the *Paramecium* compared to lower stimulation velocities. Moreover, using the developed platform this kind of high stimulation velocities was achieved for the first time on a freely swimming motile microorganism.

2) Change in direction: the second phase starts when phase 1 (backward movement) is completed. In this phase, the change in two parameters, the angle (θ_p) and the angular velocity ($\dot{\theta}_p$), have been confirmed. For comparison, the same parameters were taken in case of mechanically stimulating the posterior of the cell, where no avoiding reaction is initiated as the cell proceeds in approximately the same direction. The initial angle ($\theta_p = 0$) was considered to

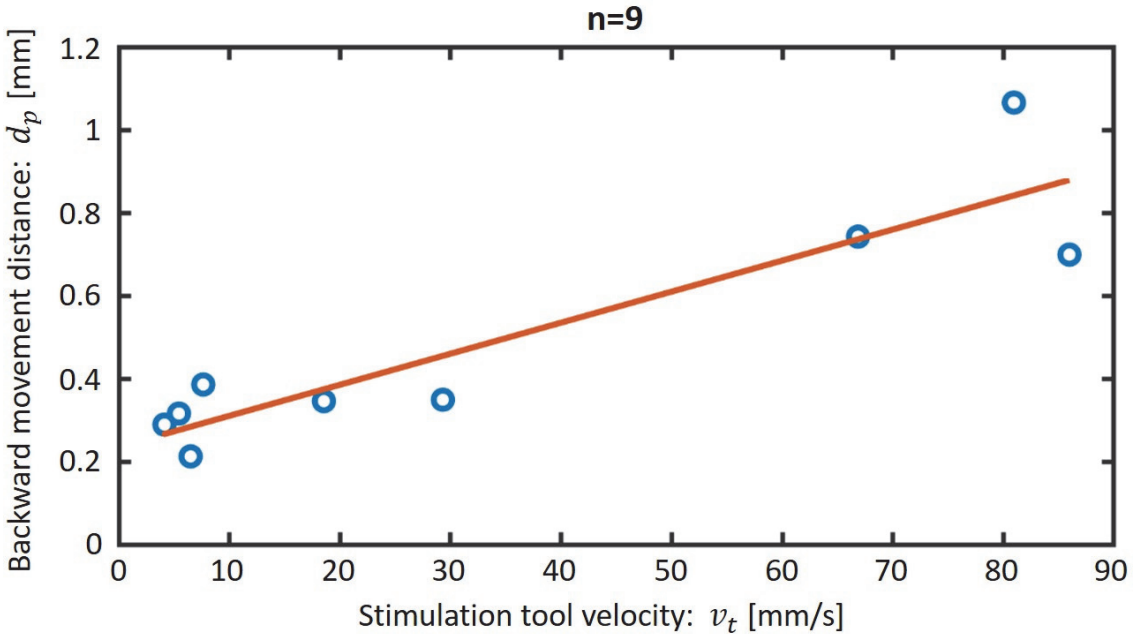

Figure 4.16: The correlation between the backward movement distance and the stimulation tool velocity.

be the angle of the microorganism at the moment when phase 1 was completed, as shown in Figure 4.17(a). Three experiments were conducted for each case. The number of the taken data points differed for each experiment depending on the time taken to finish the turning movement of the *Paramecium*. Figure 4.17(b) shows the actual data for the angle and the angular velocity

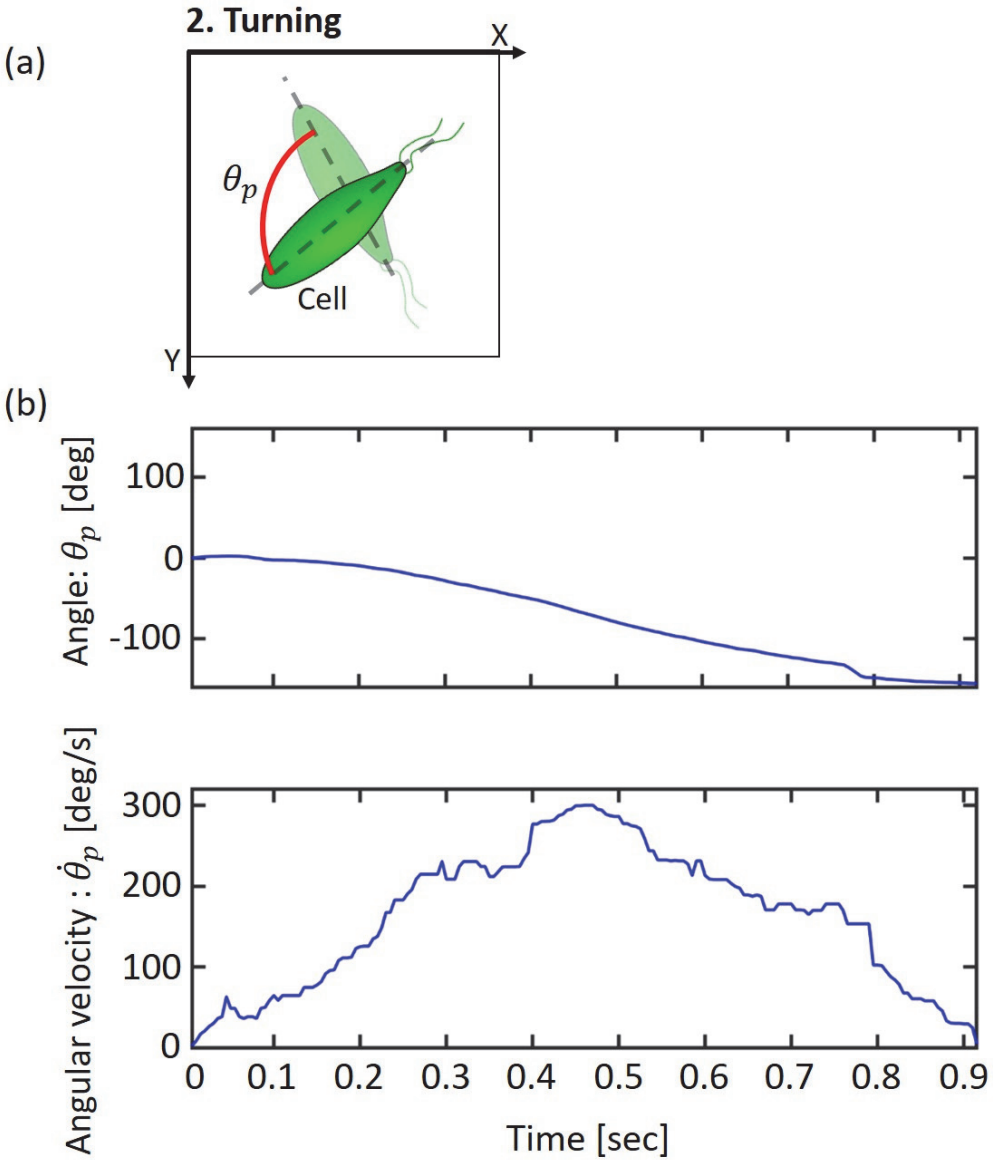

Figure 4.17: Measured angle and angular velocity of the *Paramecium* in response to mechanical stimulation.

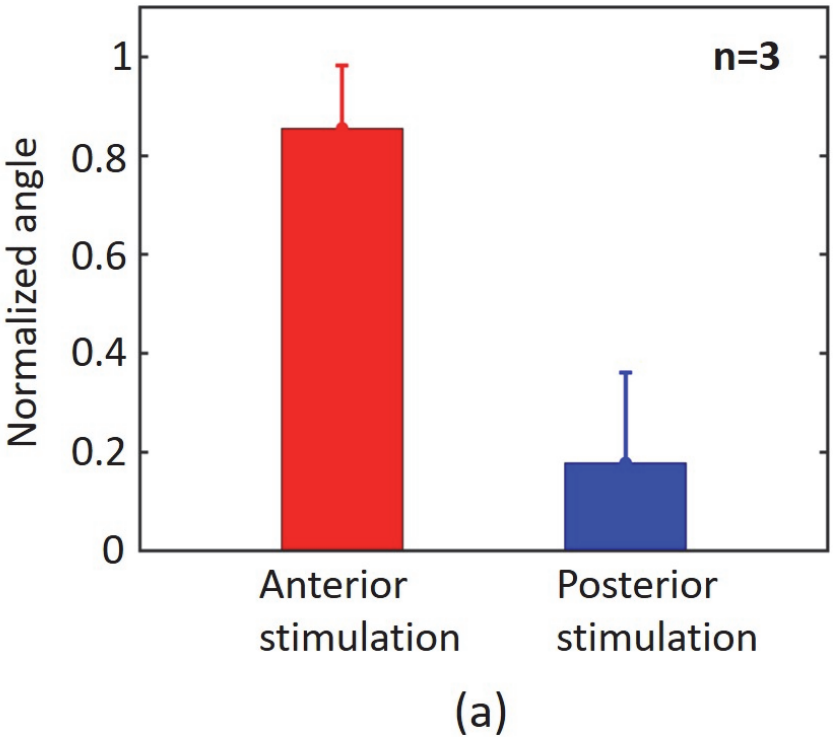

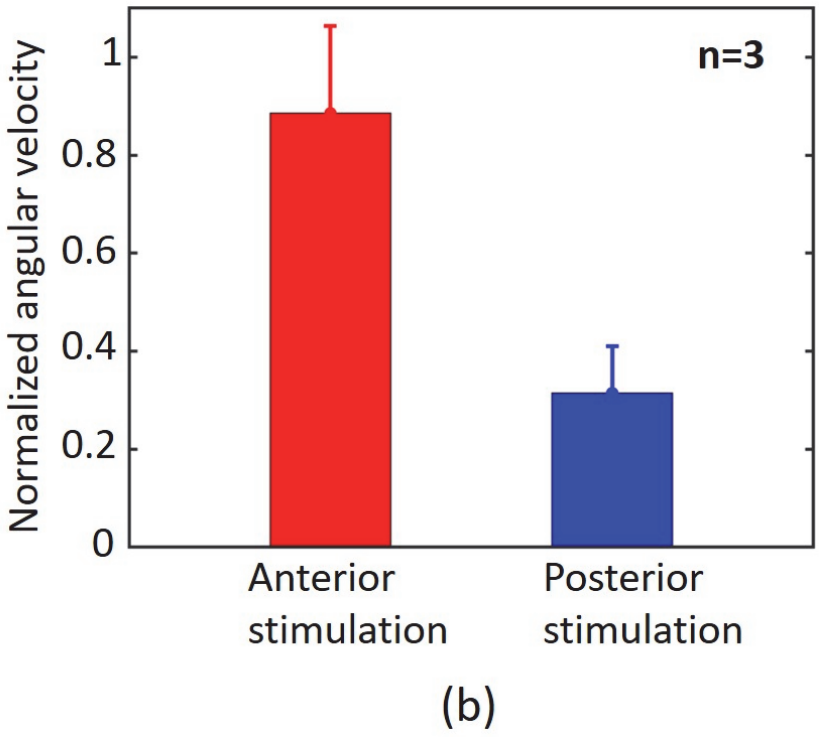

Figure 4.18: Comparison of anterior and posterior mechanical stimulation of *Paramecium*.

for one of the experiments. Figure 4.18 shows a comparison between the anterior and posterior mechanical stimulation with regards to the maximum change in angle and angular velocity. The maximum change in angle and the maximum angular velocity were confirmed from each experiment and then normalized by the maximum value of all the six experiments. Finally, the mean value and the standard deviation of the normalized values were obtained and plotted. From the figures, the second phase (turning) of avoiding behavior when stimulating the anterior of the cell can be clearly confirmed, where the stimulation of the anterior of the cell caused a large change in both the angle and the angular velocity compared to the stimulation of the posterior of the cell.

4.5.2 Electrical stimulation

Electrical stimulation has been widely applied by biologists to investigate the characteristics of bacteria and motile cells such as growth rate [84][85], which are promoted for medical applications, essentially for wound healing [86][87]. Our target motile cell, the *Paramecium*, reacts to the electric stimulation by a phenomenon called the negative galvanotaxis. In this phenomena, the *Paramecium* is forced to swim towards the cathode when an electrical stimulus is applied. This is due to the changes in the membrane potential, which controls the ciliary motion, under the electrical field influence [88]. In this experiment, electrical stimulation is applied to the freely swimming *Paramecium* inside the microfluidic chip. Two microtools are inserted from parallel side apertures of the microchips acting as electrodes. The electrodes are connected to a power supply, which supplies a maximum of 36V and 3A.

Figure 4.19 shows the results of the electrical stimulation on a freely swimming *Paramecium*. The system first starts by searching for and tracking a random target cell, as shown

in Figure 4.19(a-c). While tracking the cell, a 4V DC voltage was applied as electrical stimulation for multiple times as shown in Figure 4.19(d). Figure 4.19(e) shows the trajectory of the cell for the whole experiment. In the figure, the red-colored line indicates that electrical stimulation is applied in this area, whereas the blue colored line indicates no stimulation.

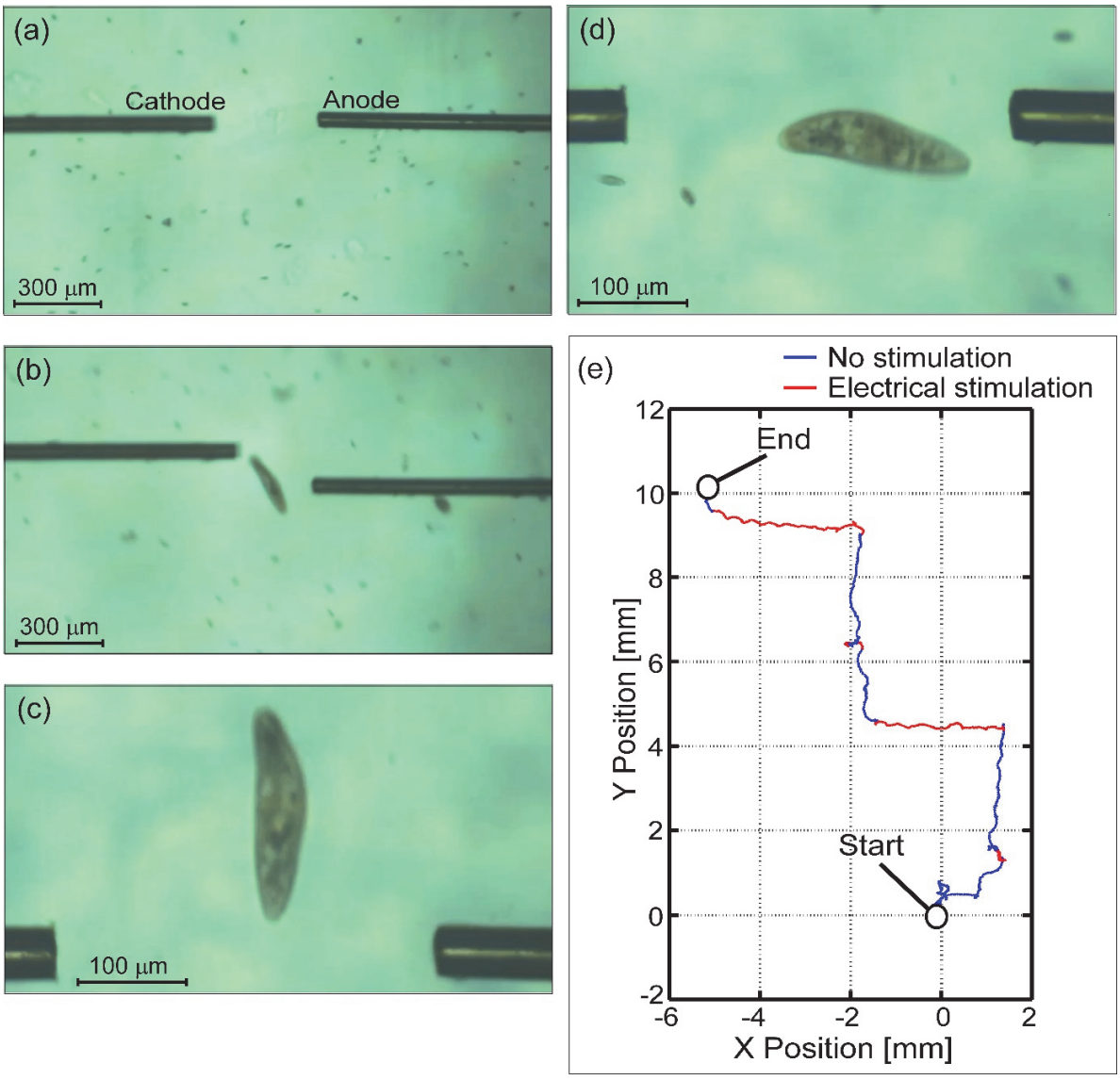

Figure 4.19: Electrical stimulation of a single freely swimming *Paramecium*.

From the figure, we can clearly confirm the galvanotaxis phenomena due to the sudden reversal in the *Paramecium* moving direction where the cell starts to swim towards the cathode. In the experiment, the target paramecium reached a maximum velocity of 2 mm/s and the maximum positioning error while tracking was around 130 μm. As for the microtools actuation accuracy, the maximum positioning error on the y-axis was around 150 μm. Moreover, the accuracy of the gap (the distance on the x-axis) between the two microtools had a maximum error around 300 μm, which is a bit large considering a 250 μm initial gap. Since the drag force is negligible on the horizontal direction, the large gap error is believed to be due to the xy stage actuation error since the x-axis handles more weight and hence more friction force.

4.6 Concluding Remarks

In this chapter, the final integrated platform for the investigation of a single motile cell has been shown. The performance and practicality of the platform were confirmed by conducting experiments on a freely swimming single *Paramecium*. The height of the microfluidic chip for actual cell experiment was first confirmed in order to restrict the vertical movement of the cell while maintaining a close-to-natural swimming mode.

Next, a number of long-time tracking experiments were conducted and the average tracking time was approximately 35 min. An elliptical ROI was used for noise elimination, as explained in Section 2.4.3. Thanks to the robustness of the developed tracking platform, the tracking could be continued regardless of the presence of noise or other cells inside the microchip.

Finally, mechanical and electrical stimulation experiments were conducted. To apply stimulations to a single cell, microtools with 50 μm thickness were driven using the magnetic

compensation approach, as proposed in Chapter 3. By virtue of the low fluidic disturbance generated by the microtools, the stimulation did not cause a tracking failure and the dynamic reaction of the *Paramecium* was confirmed without any immobilization manners. The avoiding reaction in response to mechanical stimulation was quantitatively confirmed by analyzing the captured image data with a spatial resolution of less than 5 μm and a time resolution of less than 5 ms.

Chapter 5

Conclusion

5.1 Summary

In summary, a novel microrobotic platform for the investigation of a single motile microorganism that realizes continuous observation and stimulation inside a microfluidic was demonstrated.

In Chapter 1, background and categorization for single-cell investigation through stimulation including motile cells were given. The difficulties and disadvantages of the conventional approach for observing the natural stimulus-response of motile cells were discussed. The need for a platform that realizes continuous observation and stimulation to achieve close-to-natural investigation of a single motile microorganism was proposed. The related works for the observation and stimulation of cells have been reviewed. Finally, based on this background, a new approach for the investigation of a single motile microorganism that utilizes high-speed online vision and actuators was introduced.

In Chapter 2, the design and implementation of the observation platform were explained. First, the required specifications were discussed, and the need for an observation platform that realizes robust high-speed tracking with variable magnification was established. To realize

robust real-time target tracking with variable magnification, the block diagram of the tracking and magnification controllers were shown, including the pixel pitch, focal length, and illumination control for the adaptive tracking. Consequently, a simple image processing method, which utilizes the small spatial difference between two consecutive frames, was implemented. Finally, the performance of the observation platform was confirmed. The platform could successfully track targets that move with a velocity of up to 10 mm/s even when using the largest magnification ratio available in the platform. Moreover, the robustness of the tracking control was shown through a basic experiment using software-generated image noise.

In Chapter 3, the development of a stimulation platform for single motile microorganism was shown. First, the stimulation tool size and its relation to the amount of generated fluid flow was discussed. Next, a magnetic drive method for driving thin microtools in the fluidic environment was introduced. The deflections when actuating a very thin microtool caused by the hydrodynamic drag force was compensated by utilizing permanent magnets aligned underneath the microtool. To achieve the magnetic drive with higher accuracy, permanent magnets arrangement that reduced the vertical component and enhanced the horizontal component of the magnetic force was first confirmed through numerical simulation and actual experiment on a thin microtool with a diameter of 50 μm. Finally, the positioning accuracy of the stimulation platform was confirmed through the basic experiments and the maximum positioning error of the microtool was approximately 200 μm, which was ten times lower than normal actuation without magnetic compensation.

In Chapter 4, the observation and stimulation platforms were combined into one platform that was used to conduct experiments on the actual motile microorganism. The *Paramecium* was chosen as a target of single motile microorganism. First, the tracking capability of the

platform was demonstrated. The platform achieved long-time tracking of the *Paramecium* continuously inside a microfluidic chip for more than 30 minutes, which showed the robustness of the tracking platform. After that, mechanical and electrical stimulation experiments using thin microtools driven by a magnetic compensation were conducted on a freely swimming *Paramecium* inside the microfluidic chip. The small fluidic flow generated by the microtools allowed for successful stimulation without disrupting the tracking control, and the *Paramecium* escaping behavior could be confirmed. Overall, the platform was successfully able to track and stimulate a freely swimming motile microorganism with both high-speed and high-magnification without immobilization.

5.2 Future Work

Tracking: one of the future goals for this work is to be able to observe the lifespan of the microorganism in real-time, particularly the cell division process. In order to do that, the developed platform should be able to track the microorganism for approximately one continuous day, where two main problems should be tackled:

1. The size of the elliptical ROI is fixed before the experiment. Because the platform chooses the first located cell in the environment (the microfluidic chip) randomly, the ROI parameters are not optimized for the particular microorganism being tracked, which causes some tracking failure instances especially when the target microorganism is slightly pushed by other cells. To solve this problem, the first few frames of the tracking sequence could be used to determine the parameters of the ROI based on the size of the target microorganism.

2. When conducting a tracking experiment for a long time, the XY stage was observed to overheat, which forced the termination of the experiment to guarantee the platform's safety. In fact, this problem is common in platforms and systems that operate for a relatively long time. In order to solve the heating problem, external heatsinks or an air cooling mechanism could be applied to the stage to maintain its temperature within the operational levels. This would aid in increasing the overall tracking time.

Stimulation: the currently achieved positioning accuracy of the microtool is sufficient to successfully apply stimulation to a motile microorganism, although a higher accuracy is desired. The forces opposing the movement of the microtool, mainly the hydrodynamic drag force and the friction force caused the positioning error of the microtool. Our target is local area stimulation of a single motile microorganism, and in this case, we need a positioning accuracy in the order of micrometers or at least tens of micrometers. To increase the positioning accuracy of the microtool, a number of ways can be applied individually or in a combined manner. For example, the magnets arrangement could be further optimally designed to reduce the friction force induced by the vertical component of the magnetic force as much as possible. Additionally, high-speed image feedback could be used together with the magnetic driving method proposed in Chapter 3, to accurately position the tool, which requires the detection of the tool even when a collision with the target cell occurs. On the other hand, modeling the dynamics of the microtool inside the microfluidic environment can also be effective. Using a dynamic model we can estimate the deflection of the microtool and compensate for it using feedforward control.

Analysis of dynamic behavior: after achieving local point stimulation, the final goal of this research would be to analyze the dynamic behavior of the motile microorganism. For

instance, the input-output relationship of the response to the mechanical stimulation could be analyzed to obtain the structural and dynamical mathematical model of the microorganism, such as the transfer function model. This knowledge can be very useful and inspiring in designing and fabricating the next-generation robotic sensors and actuators that mimic the dynamic behavior of motile microorganisms.

Application to various motile microorganisms: In this work, the *Paramecium* was chosen as an example motile microorganism to confirm the performance of the platform. However, the targeted motile microorganism can be extended to many other motile microorganisms within the limitation of the platform. To do that, a number of parameters need to be changed according to the size of the microorganism as listed below:

- Parameters of the ROI: a wide variety of motile microorganism's shapes and sizes exist from thin to wide and long to short. Therefore, the size and shape of the ROI need to be adjusted accordingly to achieve stable long-time tracking.
- The thickness of the microfluidic chip: in order to limit the vertical movement of the target microorganism, the thickness of the microfluidic chip needs to be considered. Thicker or thinner microchips are needed according to the target size while allowing close-to-natural movement.
- Size of the microtool: As mentioned before, the currently used microtool in the platform is 50 μm thick. This size might not be suitable to stimulate targets with a body length of less than 50 μm. On the other hand, smaller motile microorganisms require the use of thinner microfluidic chips, which can make the insertion of a 50 μm thick microtool not applicable.

Therefore, smaller or bigger microtools are needed to stimulate microorganisms with different sizes.

Bibliography

[1] K. Son, D. R. Brumley, and R. Stocker, "Live from under the lens: exploring microbial motility with dynamic imaging and microfluidics," *Nature Reviews Microbiology*, vol. 13, no. 12, pp. 761–775, 2015.

[2] V. A. Vladimirov, "Measurement of cell velocity distributions in populations of motile algae," *Journal of Experimental Biology*, vol. 207, no. 7, pp. 1203–1216, 2004.

[3] J. N. Eisenberg, J. O. Washburn, and S. J. Schreiber, "Generalist feeding behaviors of aedes sierrensis larvae and their effects on protozoan populations," *Ecology*, vol. 81, no. 4, pp. 921–935, 2000.

[4] C. A. Papadimitriou, A. Papatheodoulou, V. Takavakoglou, A. Zdragas, P. Samaras, G. P. Sakellaropoulos, M. Lazaridou, and G. Zalidis, "Investigation of protozoa as indicators of wastewater treatment efficiency in constructed wetlands," *Desalination*, vol. 250, no. 1, pp. 378–382, 2010.

[5] R. B. Frankel and R. P. Blakemore, "Magnetite and magnetotaxis in microorganisms," *Bioelectromagnetics*, vol. 10, no. 3, pp. 223–237, 1989.

[6] N. Q. Balaban, U. S. Schwarz, T. Ishizaki, and S. Narumiya, "Focal contacts as mechanosensors: externally applied local mechanical force induces growth of focal contacts by an mDia1-dependent and ROCK-independent mechanism," *The Journal of Cell Biology*, vol. 153, no. 6, pp. 1175–1185, 2001.

[7] A. E. Smith, Z. Zhang, C. R. Thomas, K. E. Moxham, and A. P. J. Middelberg, "The mechanical properties of Saccharomyces cerevisiae," *Proceedings of the National Academy of Sciences*, vol. 97, no. 18, pp. 1–4, 2000.

[8] K. Svennersten, M. Berggren, A. Richter-Dahlfors, and E. W. H. Jager, "Mechanical stimulation of epithelial cells using polypyrrole microactuators," *Lab on a Chip*, vol. 11, no. 19, pp. 3287–3293, 2011.

[9] Y. Sun, K. T. Wan, K. P. Roberts, J. C. Bischof, and B. J. Nelson, “Mechanical property characterization of mouse zona pellucida,” *IEEE Transactions on Nanobioscience*, vol. 2, no. 4, pp. 279–286, 2003.

[10] X. Yao, J. Walter, S. Burke, S. Stewart, M. H. Jericho, D. Pink, R. Hunter, and T. J. Beveridge, “Atomic force microscopy and theoretical considerations of surface properties and turgor pressures of bacteria,” *Colloids and Surfaces B: Biointerfaces*, vol. 23, no. 2–3, pp. 213–230, 2002.

[11] I. Jung, T. R. Powers, and J. M. Valles, “Evidence for two extremes of ciliary motor response in a single swimming microorganism,” *Biophysical Journal*, vol. 106, no. 1, pp. 106–113, 2014.

[12] L. H. Cisneros, R. Cortez, C. Dombrowski, R. E. Goldstein, and J. O. Kessler, “Fluid dynamics of self-propelled microorganisms, from individuals to concentrated populations,” *Animal Locomotion*, Springer, Berlin, Heidelberg, pp. 99–115, 2010.

[13] F. Bourdichon, S. Casaregola, C. Farrokh, J. C. Frisvad, M. L. Gerds, W. P. Hammes, J. Harnett, G. Huys, S. Laulund, A. Ouwehand, and I. B. Powell, “Food fermentations: microorganisms with technological beneficial use,” *International Journal of Food Microbiology*, vol. 154, no. 3, pp. 87–97, 2012.

[14] S. Fon-Sing, and M. A. Borowitzka "Isolation and screening of euryhaline Tetraselmis spp. suitable for large-scale outdoor culture in hypersaline media for biofuels," *Journal of applied phycology*, vol. 28, no. 1, pp. 1-14, 2016

[15] R. W. Carlsen, M. R. Edwards, J. Zhuang, C. Pacoret, and M. Sitti, “Magnetic steering control of multi-cellular bio-hybrid microswimmers,” *Lab on a Chip*, vol. 14, no. 19, pp. 3850–3859, 2014.

[16] N. Maki, J. E. Gestwicki, E. M. Lake, L. L. Kiessling, and J. Adler "Motility and chemotaxis of filamentous cells ofEscherichia coli," *Journal of Bacteriology*, vol. 182, no. 15, pp. 4337–4342, 2000.

[17] M. Valiadi, and D. Iglesias-Rodriguez, "Understanding bioluminescence in dinoflagellates—how far have we come?," *Microorganisms*, vol. 1, no. 1, pp. 3–25, 2013.

[18] F. Lenci, F. Ghetti, P. S. Song, "Photomovement in ciliates," *Comprehensive Series in Photosciences*, vol. 1, pp. 475–503, 2001.

[19] P. Kaur and A. Li, "Adhesive properties of human basal epidermal cells: an analysis of keratinocyte stem cells, transit amplifying cells, and postmitotic differentiating cells," *Journal of Investigative Dermatology*, vol. 114, no. 3, pp. 413–420, 2000.

[20] A. Pierres, A. M. Benoliel, D. Touchard, and P. Bongrand, "How cells tiptoe on adhesive surfaces before sticking," *Biophysical Journal*, vol. 94, no. 10, pp. 4114–4122, 2008.

[21] D.-B. Shieh, P.-C. Wu, G.-B. Lee, C.-C. Hsieh, and S.-B. Huang, "A microfluidic cell culture platform for real-time cellular imaging," *Biomedical Microdevices*, vol. 11, no. 4, pp. 903–913, 2009.

[22] T. Schroeder, "Long-term single-cell imaging of mammalian stem cells," *Nature Methods*, vol. 8, no. 4, pp. S30–S35, 2011.

[23] C. P. Ursekar, S. K. Teo, H. Hirata, I. Harada, K. H. Chiam, and Y. Sawada, "Design and construction of an equibiaxial cell stretching system that is improved for biochemical analysis," *PLoS ONE*, vol. 9, no. 3, p. e90665, 2014.

[24] Y. Xie, F. Zeng, W. Xi, Y. Zhou, H. Liu, and M. Chen, "A robot-assisted cell manipulation system with an adaptive visual servoing method," *Micromachines*, vol. 7, no. 6, p. 104, 2016.

[25] M. Hagiwara, T. Kawahara, Y. Yamanishi, T. Masuda, L. Feng, and F. Arai, "On-chip magnetically actuated robot with ultrasonic vibration for single cell manipulations," *Lab on a Chip*, vol. 11, no. 12, pp. 2049–2054, 2011.

[26] J. P. Bearinger, L. C. Dugan, L. Wu, H. Hill, A. T. Christian, and J. A. Hubbell, "Chemical tethering of motile bacteria to silicon surfaces," *BioTechniques*, vol. 46, no. 3, pp. 209–216, 2009.

[27] M. Micic, D. Hu, Y. D. Suh, G. Newton, M. Romine, and H. P. Lu, "Correlated atomic force microscopy and fluorescence lifetime imaging of live bacterial cells," *Colloids and Surfaces B: Biointerfaces*, vol. 34, no. 4, pp. 205–212, 2004.

[28] A. V Bolshakova, O. I. Kiselyova, A. S. Filonov, and O. Y. Frolova, "Comparative studies of bacteria with an atomic force microscopy," *Ultramicroscopy*, vol. 86, no. 1-2, pp. 121–128, 2001.

[29] S. Jana, A. Eddins, C. Spoon, and S. Jung, "Somersault of *Paramecium* in extremely confined environments," *Scientific Reports*, vol. 5, pp. 1–9, 2015.

[30] Y. Yan, L. Jiang, K. J. Aufderheide, G. A. Wright, A. Terekhov, L. Costa, K. Qin, W. T.

McCleery, J. J. Fellenstein, A. Ustione, and J. B. Robertson, “A microfluidic-enabled mechanical microcompressor for the immobilization of live single- and multi-cellular specimens,” *Microscopy and Microanalysis*, vol. 20, no. 1, pp. 141–151, 2014.

[31] S. Brás, R. Cunha, C. J. Silvestre, and P. J. Oliveira, “Nonlinear attitude observer based on range and inertial measurements,” *IEEE Transactions on Control Systems Technology*, vol. 21, no. 5, pp. 1889–1897, 2013.

[32] M. Jiang, Q. Gu, T. Aoyama, T. Takaki, and I. Ishii, “Real-time vibration source tracking using high-speed vision,” *IEEE Sensors Journal*, vol. 17, no. 5, pp. 1513–1527, 2017.

[33] I. Ishii, T. Ichida, Q. Gu, and T. Takaki, “500-fps face tracking system,” *Journal of Real-Time Image Processing*, vol. 8, no. 4, pp. 379–388, 2013.

[34] S. Chen, Y. Li, and N. M. Kwok, "Active vision in robotic systems: A survey of recent developments," *International Journal of Robotics Research,* vol. 30, no. 11, pp. 1343–1377, 2011.

[35] Y. Morimoto, W. H. Tan, Y. Tsuda, and S. Takeuchi, “Monodisperse semi-permeable microcapsules for continuous observation of cells,” *Lab on a Chip*, vol. 9, no. 15, pp. 2217–2223, 2009.

[36] G. Thalhammer, R. Steiger, S. Bernet, and M. Ritsch-Marte, “Optical macro-tweezers: trapping of highly motile micro-organisms,” *Journal of Optics*, vol. 13, no. 4, p. 044024, 2011.

[37] B. R. Lutz, J. Chen, and D. T. Schwartz, “Hydrodynamic tweezers: 1. noncontact trapping of single cells using steady streaming microeddies,” *Analytical Chemistry*, vol. 78, no. 15, pp. 5429–5435, 2006.

[38] C. Francois, and S. Hutchinson, “Visual servo control, part I: basic approaches,” *IEEE Robotics & Automation Magazine*, vol. 13, no. 4, pp. 82–90, 2006.

[39] F. Chaumette, “Visual servo control. part II: advanced approaches,” *IEEE Robotics and Automation Magazine*, vol. 1, no. 1, pp. 109–118, 2006.

[40] I. Sa, S. Hrabar, and P. Corke, “Outdoor flight testing of a pole inspection UAV incorporating high-speed vision,” *Springer Tracts in Advanced Robotics*, vol. 105, pp. 107–121, 2015.

[41] T. Senoo, Y. Yamakawa, Y. Watanabe, H. Oku, and M. Ishikawa, “High-speed vision and its application systems,” *Journal of Robotics and Mechatronics*, vol. 26, no. 3, pp. 287–301, 2014.

[42] H. Wu, K. Zou, T. Zhang, A. Borst, and K. Kühnlenz, “Insect-inspired high-speed motion vision system for robot control,” *Biological Cybernetics*, vol. 106, no. 8–9, pp. 453–463, 2012.

[43] I. Ishii, T. Taniguchi, K. Yamamoto, and T. Takaki, “High-frame-rate optical flow system,” *IEEE Transactions on Circuits and Systems for Video Technology*, vol. 22, no. 1, pp. 105–112, 2012.

[44] J. Sakakibara, J. Kita, and N. Osato, “Note: high-speed optical tracking of a flying insect,” *Review of Scientific Instruments*, vol. 83, no. 3, p. 036103, 2012.

[45] N. Ogawa, S. Member, H. Oku, K. Hashimoto, and M. Ishikawa, “Microrobotic visual control of motile cells using high-speed tracking system,” *IEEE Transactions on Robotics*, vol. 21, no. 3, pp. 704–712, 2005.

[46] F. Janabi-Sharifi and M. Marey, “A Kalman-filter-based method for pose estimation in visual servoing,” *IEEE Transactions on Robotics*, vol. 26, no. 5, pp. 939–947, 2010.

[47] S. Y. Chen, “Kalman filter for robot vision: a survey,” *IEEE Transactions on Industrial Electronics*, vol. 59, no. 11, pp. 4409–4420, 2012.

[48] S. Shen, Y. Mulgaonkar, N. Michael, and V. Kumar, “Vision-based state estimation and trajectory control towards high-speed flight with a quadrotor,” *Robotics: Science and Systems*, vol. 1, 2013.

[49] A. W. M. Smeulders, D. M. Chu, R. Cucchiara, S. Calderara, A. Dehghan and M. Shah, “Visual tracking : an experimental survey,” *IEEE Transactions on Pattern Analysis and Machine Intelligence*, vol. 36, no. 7, pp. 1442–1468, 2014.

[50] S. Sarkar, V. Venugopalan, K. Reddy, J. Ryde, N. Jaitly, and M. Giering, “Deep learning for automated occlusion edge detection in RGB-D frames,” *Journal of Signal Processing Systems*, vol. 88, no. 2, pp. 205–217, 2017.

[51] W. Ouyang, H. Zhou, H. Li, Q. Li, J. Yan, and X. Wang, “Jointly learning deep features, deformable parts, occlusion and classification for pedestrian detection,” *IEEE Transactions on Pattern Analysis and Machine Intelligence*, vol. 40, no. 8, pp. 1874–1887, 2018.

[52] H. T. Nguyen and A. W. M. Smeulders, “Fast occluded object tracking by a robust appearance filter,” *IEEE Transactions on Pattern Analysis and Machine Intelligence*, vol. 26, no. 8, pp. 1099–1104, 2004.

[53] S. Hare, S. Golodetz, A. Saffari, V. Vineet, M. Cheng, S. L. Hicks, and P. H. S. Torr, "Struck: structured output tracking with kernels," *IEEE Transactions on Pattern Analysis and Machine Intelligence*, vol. 38, no. 10, pp. 2096–2109, 2016.

[54] F. Arai, A. Kawaji, P. Luangjarmekorn, T. Fukuda, and K. Itoigawa, "Three-dimensional bio-micromanipulation under the microscope," *IEEE International Conference on Robotics & Automation*, pp. 604–609, 2001.

[55] T. Tanikawa and T. Arai, "Development of a micro-manipulation system having a two-fingered micro-hand," *IEEE Transactions on Robotics and Automation*, vol. 15, no. 1, pp. 152–162, 1999.

[56] R. Afrin, U. S. Zohora, H. Uehara, T. Watanabe-Nakayama, and A. Ikai, "Atomic force microscopy for cellular level manipulation: Imaging intracellular structures and DNA delivery through a membrane hole," *Journal of Molecular Recognition*, vol. 22, no. 5, pp. 363–372, 2009.

[57] O. Guillaume-Gentil, E. Potthoff, D. Ossola, C. M. Franz, T. Zambelli, and J. A. Vorholt, "Force-controlled manipulation of single cells: from AFM to FluidFM," *Trends in Biotechnology*, vol. 32, no. 7, pp. 381–388, 2014.

[58] O. Guillaume-Gentil, E. Potthoff, D. Ossola, P. Dörig, T. Zambelli, and J. A. Vorholt, "Force-controlled fluidic injection into single cell nuclei," *Small*, vol. 9, no. 11, pp. 1904–1907, 2013.

[59] A. Meister, M. Gabi, P. Behr, P. Studer, J. Vörös, P. Niedermann, J. Bitterli, J. Polesel-Maris, M. Liley, H. Heinzelmann, and T. Zambelli , "FluidFM: Combining atomic force microscopy and nanofluidics in a universal liquid delivery system for single cell applications and beyond," *Nano Letters*, vol. 9, no. 6, pp. 2501–2507, 2009.

[60] P. Dörig, P. Stiefel, P. Behr, E. Sarajlic, D. Bijl, M. Gabi, J. Vörös, JA. Vorholt, and T. Zambelli, "Force-controlled spatial manipulation of viable mammalian cells and micro-organisms by means of FluidFM technology," *Applied Physics Letters*, vol. 97, no. 2, pp. 1–4, 2010.

[61] Z. Ye and M. Sitti, "Dynamic trapping and two-dimensional transport of swimming microorganisms using a rotating magnetic microrobot," *Lab on a Chip*, vol. 14, no. 13, pp. 2177–2182, 2014.

[62] M. Hagiwara, T. Kawahara, T. Iijima, and F. Arai, "High-speed magnetic microrobot actuation in a microfluidic chip by a fine V-groove surface," *IEEE Transactions on Robotics*, vol. 29, no. 2, pp. 1–10, 2012.

[63] H. Oku, N. Ogawa, M. Ishikawa, and K. Hashimoto, "Two-dimensional tracking of a motile micro-organism allowing high-resolution observation with various imaging techniques," *Review of Scientific Instruments*, vol. 76, no. 3, pp. 1–9, 2005.

[64] D. Bradley, and G. Roth, "Adaptive thresholding using the integral image," *Journal of graphics tools*, vol. 12, no. 2, pp. 13–21, 2007.

[65] I. Barkana, "Simple adaptive control--a stable direct model reference adaptive control methodology--brief survey," *International Journal of Adaptive Control and Signal Processing*, vol. 28, no. 7–8, pp. 567–603, 2014.

[66] A. Borji, D. N. Sihite, and L. Itti, "Salient object detection : a benchmark supplementary material," *IEEE transactions on image processing*, vol. 24, no. 12, pp. 5706–5722, 2012.

[67] D. Holz, A. Topalidou-Kyniazopoulou, J. Stuckler, and S. Behnke, "Real-time object detection, localization and verification for fast robotic depalletizing," *IEEE International Conference on Intelligent Robots and Systems*, pp. 1459–1466, 2015.

[68] A. Noda, Y. Yamakawa, and M. Ishikawa, "Target tracking behind occlusions using a networked high-speed vision system," *IEEE SENSORS,* pp. 2018–2021, 2014.

[69] M. Fernando, R. Oliveira, V. Santos, and M. Silva, "Development of interfaces for impaired users," Available online: http://red.pe.org.pl/articles/2012/1a/26.pdf (accessed on 10 May 2019)

[70] M. Hagiwara, T. Kawahara, Y. Yamanishi, and F. Arai, "Driving method of microtool by horizontally arranged permanent magnets for single cell manipulation," *Applied Physics Letters*, vol. 97, no. 1, pp. 1–4, 2010.

[71] G. R. Wang, F. Yang, and W. Zhao, "There can be turbulence in microfluidics at low Reynolds number," *Lab on a Chip*, vol. 14, no. 8, pp. 1452–1458, 2014.

[72] "COMSOL Multiphysics® v. 5.2a. www.comsol.com. COMSOL AB, Stockholm, Sweden."

[73] H. Plattner, "My favorite cell-*Paramecium*," *Bioessays*, vol. 24, no. 2002, pp. 649–658, 2007.

[74] C. Kung, S.-Y. Chang, Y. Satow, J. Van Houten, and H. Hansma, "Genetic dissection of behavior in *Paramecium* behavioral," *Science*, vol. 188, no. 4191, pp. 898–904, 1975.

[75] A. Adoutte, R. Ramanathan, R. M. Lewis, R. R. Dute, K. Ling, C. Kung, and D. L. Nelson, "Biochemical studies of the excitable membrane of *Paramecium* tetra urelia : III. proteins of cilia

and ciliary membranes," *Journal of Cell Biology*, vol. 84, no. 3, pp. 717–738, 1980.

[76] J. Yano, M. Valentine, and J. Van Houten, "Novel insights into the development and function of cilia using the advantages of the *Paramecium* cell and its many cilia," *Cells*, vol. 4, no. 3, pp. 297–314, 2015.

[77] G. Knoll, B. Haacke-Bell, and H. Plattner, "Local trichocyst exocytosis provides an efficient escape mechanism for *Paramecium* cells," *European Journal of Protistology*, vol. 27, no. 4, pp. 381–385, 1991.

[78] A. Hamel, C. Fisch, L. Combettes, P. Dupuis-Williams, and C. N. Baroud, "Transitions between three swimming gaits in *Paramecium* escape," *Proceedings of the National Academy of Sciences*, vol. 108, no. 18, pp. 7290–7295, 2011.

[79] C. Erxleben, N. Klauke, M. Flötenmeyer, M. Blanchard, and C. Braun, "Microdomain Ca2+ activation during exocytosis in *Paramecium* cells. superposition of local subplasmalemmal calcium store activation by local Ca2+ influx," *Journal of Cell Biology*, vol. 136, no. 3, pp. 597–607, 1997.

[80] L. H. Bannister, "The structure of trichocysts in *Paramecium caudatum*," *Journal of Cell Science*, vol. 11, no. 3, pp. 899–929, 1972.

[81] K. Fujiu, Y. Nakayama, H. Iida, M. Sokabe, and K. Yoshimura, "Mechanoreception in motile flagella of Chlamydomonas," *Nature Cell Biology*, vol. 13, no. 5, pp. 630–632, 2011.

[82] K. Yoshimura, "Stimulus perception and membrane excitation in unicellular alga Chlamydomonas," *Coding and Decoding of Calcium Signals in Plants*. *Signaling and comunication in plants Springer*, Springer, Berlin, Heidelberg, pp. 79–91, 2011.

[83] H.S. Jennings, "Behavior of the lower organisms," *Columbia University Press*, no. 10, 1906.

[84] H. L. Merriman, C. A. Hegyi, C. R. Albright-Overton, J. Carlos, R. W. Putnam, and J. A. Mulcare, "A comparison of four electrical stimulation types on Staphylococcus aureus growth in vitro," *The Journal of Rehabilitation Research and Development*, vol. 41, no. 2, pp. 139–146, 2005.

[85] N. J. Szuminsky, A. C. Albers, P. Unger, and J. G. Eddy, "Effect of narrow, pulsed high voltages on bacterial viability," *Physical Therapy*, vol. 74, no. 7, pp. 660–667, 1994.

[86] G. Thakral, J. La Fontaine, P. Kim, B. Najafi, A. Nichols, and L. A. Lavery, "Treatment options

for venous leg ulcers: effectiveness of vascular surgery, bioengineered tissue, and electrical stimulation," *Advances in Skin and Wound Care*, vol. 28, no. 4, pp. 164–172, 2015.

[87] M. R. Asadi and G. Torkaman, "Bacterial inhibition by electrical stimulation," *Advances in Wound Care*, vol. 3, no. 2, pp. 91–97, 2013.

[88] N. Ogawa, H. Oku, K. Hashimoto, and M. Ishikawa, "A physical model for galvanotaxis of *Paramecium* cell," *Journal of Theoretical Biology*, vol. 242, no. 2, pp. 314–328, 2006.

List of Achievements

Journal Articles

[1] **B. Ahmad**, H. Maeda, T. Kawahara, and F. Arai, "Microrobotic platform for single motile microorganism investigation," *Micromachines*, vol. 8, no. 10, p. 295, 2017. [Selected as Cover Paper of the Issue]

[2] W. Huang, S. Zhang, **B. Ahmad**, and T. Kawahara, "Three-motorized-stage cyclic stretching system for cell monitoring based on chamber local displacement waveform," *Applied Sciences*, vol. 9, no. 8, p. 1560, 2019.

Conference Proceedings (Full-Paper-Review) (* Presenting author)

[1] **B. Ahmad***, H. Maeda, T. Kawahara, and F. Arai "Fine positioning of micro-tubular-tools for investigating the stimulus response of swimming *Paramecium,*" *IEEE RAS/EMBS International Conference on Biomedical Robotics and Biomechatronics (BioRob)*, pp. 634–639, 2018.

[2] **B. Ahmad***, D. Sato, R. Takemoto, H. Ohtsuka, I. Ishii, and T. Kawahara "Dynamic behavior of running insects activated by high-speed microdroplets manipulation," *International Conference on Manipulation, Automation and Robotics at Small Scale (MARSS)*, paper no. 78, 2018.

[3] W. Huang*, **B. Ahmad**, and T. Kawahara "On-line tracking of living cell subjected to cyclic stretch," *International Conference of the IEEE Engineering in Medicine and Biology Society (EMBC)*, pp. 3553–3556, 2015.

[4] **B. Ahmad**, T. Kawahara*, T. Yasuda, and F. Arai "Microrobotic platform for mechanical stimulation of swimming microorganism on a chip," *IEEE/RSJ International Conference on Intelligent Robots and Systems (IROS)*, pp. 4680 – 4685, 2014.

Conference Proceedings (Abstract-Review) (* Presenting author)

[1] T. Kawahara*, D. Sato, **B. Ahmad**, and H. Ohtsuka "On-line tracking and ejection system for investigating dynamic behavior of running insects," *IEEE/RSJ International Conference on Intelligent Robots and Systems (IROS)*, 2017. (Poster presentation)

[2] **B. Ahmad***, and T. Kawahara "Motile cell tracking and stimulation using high-speed microrobotic platform," *International Conference on Computational Methods in Engineering and Health Science (ICCMEH)*, p. 50, 2016.

[3] **B. Ahmad***, T. Kawahara, T. Yasuda, and F. Arai "Real-time observation and stimulation of a single motile cell using high-speed microrobotic platform," *IEEE International Symposium on Micro-NanoMechatronics and Human Science (MHS)*, pp. 164–164, 2016.

[4] T. Kawahara*, **B. Ahmad**, and F. Arai "High-speed microrobotic platform for mechanical manipulation of single microorganism," *17th International Symposium on Robotics Research (ISRR)*, pp. 1–13, 2015.

[5] **B. Ahmad***, T. Kawahara, T. Yasuda, and F. Arai "On-line tracking and stimulation of swimming microorganism by on-chip microrobot," *IEEE International Symposium on Micro-NanoMechatronics and Human Science (MHS)*, pp. 179–181, 2014.

[6] W. Huang*, **B. Ahmad**, and T. Kawahara "A system for real-time imaging of living cells exposed to cyclic stretch," *4th Japan-Switzerland Workshop on Biomechanics (JSB)*, p. 52, 2014.

Domestic Conference Proceedings (Abstract-Review) (* Presenting author)

[1] D. Sato*, **B. Ahmad**, T. Kawahara, and H. Ohtsuka "Development of a platform for investigating the dynamic behavior of walking insects," *The 18th SICE System Integration Division Annual Conference*, pp. 143–144, 2017.

[2] T. Kawahara*, **B. Ahmad**, T. Yasuda, and F. Arai "High-speed and high-magnification tracking of motile cells," *The Proceedings of Mechanical Engineering Congress*, J0230106, 2016.

[3] **B. Ahmad***, T. Kawahara, T. Yasuda, and F. Arai "Single Motile Cell Analysis using High Speed Microrobotic Platform," *The 32nd Conference on Chemistry and Micro. Nano Systems (Cheminas)*, p. 83, 2015. (Poster presentation)

[4] W. Huang*, **B. Ahmad**, and T. Kawahara "Real-time observation of cells exposed to cyclic stretch based on membrane deformation properties of stretch chamber," *Proceedings of the 26th Japan Society of Mechanical Engineering Conference on Frontiers in Bioengineering*, pp. 149–150, 2015.

[5] W. Huang*, **B. Ahmad**, and T. Kawahara "A platform for the observation of cells exposed to cyclic stretch under dynamic conditions," *Proceedings of the 27th Bioengineering Conference Annual meeting of BED/JSME*, pp. 385–386, 2015.

[6] **B. Ahmad***, T. Kawahara, T. Yasuda, and F. Arai "Mechanical stimulation of swimming microorganism by on-chip microrobot," *The 32nd annual conference of the Robotics Society of Japan (RSJ)*, 1D3–03, 2014.

Patents

[1] T. Kawahara, W. Huang, **B. Ahmad** "Cell Observation Apparatus," Japan Patent # 6393515, issued on November 26, 2015.

Acknowledgments

Foremost, I am grateful to **Associate Prof. Tomohiro Kawahara**, who was my supervisor in Ph.D. His strict but insightful supervision was one of the most important things that polished me as a Ph.D. student. His deep knowledge of sensing, control, and robotics allowed me to gain significant experience through frequent and fruitful discussions. His contribution was not limited to discussing, planning, and conducting research work, but he also supported me in personal aspects that were a great encouragement for me. He was a great example of a professional researcher whom I would like to follow in the future.

I would like to thank **Prof. Takashi Yasuda**, **Prof. Idaku Ishii, Prof. Yoko Yamanishi, Associate Prof. Kazuto Takashima** and **Prof. Fumihito Arai**, for their valuable and significant discussions and suggestions regarding my research work.

I would also like to thank all the current lab members: **Ms. Kiyoko Isei**, **Mr. Hironobu Maeda**, **Mr. Michiya Ueda**, **Mr. Yuuki Kawajiri**, **Mr. Hatsushi Taniguchi**, and **Mr. Motoki Furukawa**, as well as previous members: **Dr. Wenjing Huang**, **Ms. Ayako Shiraishi**, **Mr. Hiroki Nakane**, **Mr. Makoto Itayama**, **Mr. Sato Daiki**, **Mr. Masahiro Fukuda**, and **Mr. Leo Takemoto** for making the lab a bright and enjoyable place, and for their comments, discussions, and support in experimental work throughout my research.

I would like to thank the Ministry of Education, Culture, Sports, Science and Technology of Japan (MEXT) for their significant financial support.

I am grateful to all my friends in the Science and Research Park in Kitakyushu for all the support and encouragement and memorable times.

And last but not least, I express my deepest gratitude to my family, for without them I would not have gotten the opportunity to be in Japan and receive this degree. To my mom and dad, my sister, my two brothers, and my lovely nephews your love and support have been overwhelming, and for it, I humbly thank you.